Active and Fast Tunable Plasmonic Metamaterials

A thesis submitted in partial fulfilment of the requirements of the University of South Wales for the award of Doctor of Philosophy

PhD Thesis

Yusuf Abubakar

September 2023

Acknowledgements

Abstract

Active and Fast Tunable Plasmonic Metamaterials is a research development that has contributed to studying the interaction between light and matter, specifically focusing on the interaction between the electromagnetic field and free electrons in metals. This interaction can be stimulated by the electric component of light, leading to collective oscillations. In the field of nanotechnology, these phenomena have garnered significant interest due to their ability to enable the transmission of both optical signals and electric currents through the same thin metal structure. This presents an opportunity to connect the combined advantages of photonics and electronics within a single platform. This innovation gives rise to a new subfield of photonics known as plasmonic metamaterials.

Plasmonic metamaterials are artificial engineering materials whose optical properties can be engineered to generate the desired response to an incident electromagnetic wave. They consist of subwavelength-scale structures which can be understood as the atoms in conventional materials. The collective response of a randomly or periodically ordered ensemble of such meta-atoms defines the properties of the metamaterials, which can be described in terms of parameters such as permittivity, permeability, refractive index, and impedance. At the interface between noble metal particles and dielectric media, collective oscillations of the free electrons in the metal particles can be resonantly excited, known as plasmon resonances. This work considered two plasmon resonances: localised surface plasmon resonances (LSPRs) and propagating surface plasmon polaritons (SPPs).

The investigated plasmonic metamaterials, designed with specific structures, were considered for use in various applications, including telecommunications, information processing, sensing, industry, lighting, photovoltaic, metrology, and healthcare. The sample structures are manufactured using metal and dielectric materials as artificial composite materials. It can be used in the electromagnetic spectrum's visible and near-infrared wavelength range. Results obtained proved that artificial composite material can produce a thermal coherent emission at the mid-infrared wavelength range and enable active and fast-tunable optoelectronic devices. Therefore, this work focused on the integrated thermal infrared light source platforms for various applications such as thermal analysis, imaging, security, biosensing, and medical diagnosis. Enabled by Kirchhoff's law of thermal radiation, this work combined the concepts of material absorption with material emission. Hence, the results obtained proved that this approach enhances the overall performance of the active and fast-tunable plasmonic

metamaterial in terms of with effortless and fast tunability. This work further considers the narrow line width of the coherent thermal emission, tunable emission, and angular tunable emission at the mid-infrared, which are achieved through plasmonic stacked grating structure (PSGs) and plasmonic infrared absorber structure (PIRAs).

Three-dimensional (3D) plasmonic stacked gratings (PSGs) was used to create a tunable plasmonic metamaterial at optical wavelengths ranging from 3 m to 6 m, and from 6m to 9 m. These PSGs are made of a metallic grating with corrugations caused by narrow air openings, followed by a Bragg grating (BG). Additionally, this work demonstrated a thermal radiation source customised for the mid-infrared wavelength range of 3 μm to 5 μm. This source exhibits intriguing characteristics such as high emissivity, narrowband spectra, and sharp angular response capabilities. The proposed thermal emitter consists of a two-dimensional (2D) metallic grating on top of a one-dimensional dielectric BG.

Results obtained presented a plasmonic infrared absorber (PIRA) graphene nanostructure designed for a wavelength range of 3 to 14 μm. It was observed and concluded that this wavelength range offers excellent opportunities for detection, especially when targeting gas molecules in the infrared atmospheric windows. The design framework is based on active plasmon control for subwavelength-scale infrared absorbers within the mid-infrared range of the electromagnetic spectrum. Furthermore, this design is useful for applications such as infrared microbolometers, infrared photodetectors, and photovoltaic cells.

Finally, the observation and conclusion drawn for the sample of nanostructure used in this work, which consists of an artificial composite arrangement with plasmonic material, can contribute to a highly efficient mid-infrared light source with low power consumption, fast response emissions, and is a cost-effective structure.

Contents

Acronyms and Symbols

A	Absorption
B	Magnetic field
BG	Bragg grating
D	Electric displacement or dielectric
DNG	Double negative metamaterial
E	Electric field
EM	Electromagnetic wave
LAN	Local area networks
LHM	Left-hand metamaterials
M	Magnetisation of the optical medium
MG	Metallic grating
NDIR	Non-dispersive infrared
P	Polarisation density of the optical medium
PMM	Plasmonic metamaterials
PIRA	Plasmonic infrared absorber
PSG	Plasmonic stacked grating
PMM	Plasmonic metamaterial structure
PIRA	Plasmonic infrared absorber structure
PSGs	Plasmonic stacked grating structure,
Q	Source charge
SPs	Surface plasmons
SPPs	Surface plasmon polaritons
SDL	Spacing dielectric layer
SGs	Stacked grating
T	Temperature,
TM	Transverse magnetic
TE	Transverse electric
$\vec{B}$	Magnetic field vector
c	Speed of light in a vacuum,
$\vec{E}$	Electric field vector
$\vec{F}$	Electric force vector

h	Planck's constant
i_c	Conduction current
i_d	Displacement current
k	Boltzmann constant
n	Refractive index
v	Velocity of light in the medium
V_g	Group velocity
V_p	Phase velocity
ε_r	Relative permittivity
μ_r	Relative permeability
ϵ	Emissivity
λ	Wavelength
ω	Angular Frequency
ω_p	Plasma frequency
q_o	Charge particle
P_t	Poynting vector
r	Distance
σ	Area density
$\hat{A}$	Surface area
θ	Angle of incidence
ε	Permittivity of the medium
μ	Permeability of the medium
ε_o	Permittivity of the free space
μ_o	Permeability of the free space
k_o	Free space wave-vector
$\hbar k_o$	Free space photon
ε_{eff}	Effective permittivity
μ_{eff}	Effective permeability
ξ_o and z_o	Characteristic impedance for air (free space)
z_{PMM_s} and ξ_{n+1}	Characteristic impedance for the Plasmonic Metamaterial

List of Figures

List of tables

Chapter 1

Research Background

1.1 General Introduction

In recent decades, diverse technological applications have significantly expanded, profoundly impacting our daily lives. Many of these advancements were unforeseen in the past two decades. The exponential progression in shrinking integrated circuits to the nanometer scale has created significant opportunities for the widespread availability of inexpensive consumer electronics. Since the 1960s, the advancements in microelectronics have spurred the information revolution. The expanding market demands advanced hardware each year across various aspects, including sensing, imaging, processing, transmitting, displaying, and energy generation. These needs exceed the capabilities of traditional electronic systems due to the physical limitations predicted by Gordon Moore's law (Moore, 1998).

Photonics is the study of photons that emerged as a viable medium for transmitting information since the 1970s (Poldervaart and Sluijter, 1975) due to its broadband characteristics, swift response, high-volume data storage, and compatibility with modern electronic systems. This compatibility owes much to the photoelectric effect explained by Albert Einstein et al. (Einstein, 1905).

Moreover, Moore's law has delineated the roadmap for the semiconductor industry, advocating continued scaling down for decades and forming the foundation of the burgeoning field of nanotechnology, which has experienced exponential growth since the 1980s. Several research interests and domains have emerged within nanotechnology. One such relatively recent area of study is the "plasmonics" which is enabled the investigation into surface plasmons. In essence, Plasmonics is the branch of nanophotonics that studies the interaction between light and matter, and the behaviours of light at the nanometer level. A plasmon refers to the collective oscillation of free electrons occurring at the interface of metals and a dielectric medium. It can also be seen as a quasiparticle that is defined as a quantum of plasma oscillation. This is like photons as quanta of light and phonons as quanta of mechanical vibration. Although plasmons is known for a long time, recent technological advancements have empowered researchers to control them deliberately on the nanometer scale to generate, manipulate and detect light.

Another promising research area in nanotechnology is the study of 'metamaterials.' These are artificially engineered materials whose optical properties can be manipulated to produce the desired response to an incident electromagnetic wave. The origin of this field is attributed to the work of Russian physicist Viktor Veselago in 1968 (Veselago, 1968) that theoretically described the electromagnetic response of a material exhibiting simultaneously negative values for the real part of the electric permittivity and magnetic permeability. Veselago proposed that such a material would possess a negative refractive index. This unexpected result sparked widespread scepticism at the time, as no such material was known to exist. However, in the year 2000, John Pendry revisited this concept. While Veselago had demonstrated that such a material could create a flat lens, Pendry predicted that this lens would offer a non-diffraction-limited resolution, introducing the concept of 'a perfect lens' (Pendry, 2000). Pendry's work sparked a surge in the field of metamaterials, which now includes numerous electromagnetic materials catering to a wide array of applications, such as optical invisibility (cloaking), polarisation control, and even light slowing (transition optics).

In general, photonic technology has numerous applications. For instance, in telecommunication, particularly optical fibre communication, photonics has proved crucial for deploying resilient high-quality and high-speed telecommunication systems. Benefits include telecommunication links and high signalling rates internet service. Moreover, the development of lighting and energy-saving technologies in photonics has made significant contributions, leading to almost all lighting industries toward innovative photonics applications. As a part of photonics achievements, photovoltaic benefits modernly designed houses, streets, roads, and electric vehicles through energy conversion. Additionally, photonics is commonly recognised as a key enabling technology for the 21st century and holds the potential for even more significant societal impacts in the future (Council, 1998, Svedberg, 2012).

This thesis integrates the domains of plasmonics and metamaterials, emphasising the design, production, and characterisation of plasmonic metamaterial structures to achieve coherent emission through thermal motion. Results obtained from the sample of nanostructure consists of artificial composite arrangement with plasmonic material, prove that it can contribute to achieving cost-effective structure highly efficient mid-infrared light source with low power consumption and fast response emissions.

1.2   Thesis structure

Chapter 2 examines the background theories of plasmonics that contributed to the discovery of the optical properties of metal nanostructures. It introduces plasmonics and metamaterials, covering active and passive plasmonic components, as an optical domain capable of demonstrating excitability and propagation. Additionally, it introduces thermal photonics metamaterials and their role in mid-infrared thermal emission as key enabling applications.

Chapter 3 focuses on the fundamental principles of plasmonic metamaterials. Maxwell's equations are introduced to justify wave propagation through materials. The concept of metamaterials and the classification of materials based on permittivity and permeability are discussed. This chapter demonstrates the elements collectively forming the framework for active and fast tunable plasmonic metamaterials.

Chapter 4 covers the methodology and simulation algorithm for the nanophotonic design. It also presents the computational modelling approaches based on electromagnetic theory, which is a method for fabricating plasmonic metamaterial structures. The use of simulation methodologies finite-difference time-domain (FDTD) and DEVICE are used as design tools are also contained in this chapter. Fundamental phenomena that give rise to the features observed in the emission spectra of three-dimensional (3D), two-dimensional (2D), and one-dimensional (1D) periodic arrangements of plasmonic metamaterials (PMMs) are explained. These are used to develop physical intuition and understanding of the features behind the thermal emission spectrum.

Chapter 5 introduces the design work of plasmonic stacked gratings (PSG) structure based on two distinct PMM samples: a flat rectangular metallic patch and an air-corrugated metallic patch. This chapter emphasises on coherence thermal emission, multi-wavelength emission, and the angular and tunability properties of PSGs.

Chapter 6 deals with the design work of plasmonic infrared absorber (PIRA) structure based on two distinct PMM samples: with a graphene surface conductivity patch and without a graphene surface conductivity patch. This chapter highlights the absorption profile of the surface plasmon resonance enhancement through and without the graphene, including the tunability properties of the PIRA structure.

Chapter 7 presents the conclusion of the work completed in this project. It summarised key findings and highlights novelties and contribution to knowledge and provides a detailed upcoming optimisation viewpoint for all designs discussed in this thesis.

Chapter 2
Literature Review

This chapter introduces the background theories of plasmonics and metamaterials that have contributed to discovering the optical properties of metal nanostructures. It examines the fundamental mechanisms of plasmonics and metamaterials, including active and passive components of plasmonics and their development. For instance, thermal spectra control is used to manipulate thermal emission from broad to narrowband, fast modulation techniques and mid-infrared thermal emission are explored for various technological applications. These benefits were treated in this chapter.

2.1 Background Theory

Before scientists discovered the optical properties of metal nanostructures, artists used them to create colours in glass objects and artwork. The presence of gold nanoparticles of various sizes created a rainbow of colours. For instance, the Lycurgus cup from the Roman Empire in the 4th century appears green when observed in reflected light and shines red when light passes through it. Examples such as the Egyptian Gold-Plated Archaeological Ivory from the 8th century BC, part of the Louvre collection originating from Arslan Tash, Syria (Spadavecchia et al., 2014) and Teapot (1680) obtained by Johannes Kunckel using the 'Purple of Cassius' technique showcase the use of plasmonic materials. The Roman Cup, known as the Lycurgus Cup, is a typical example of plasmonic materials. This cup contains nanometer-sized silver and gold clusters, allowing localised plasmon resonances to be stimulated with visible light within the glass cup. Consequently, the applications related to plasmonic nanoparticles are impressively numerous. Due to the considerable interest in research across various disciplinary perspectives, these applications include biomedical uses in sensing (Saha et al., 2012, Di Fabrizio et al., 2016), cellular imaging (Murphy et al., 2008, Austin et al., 2015), electronics (Cho et al., 2012, Barsotti Jr et al., 2007), and nonlinear optical processes(Amendola and Meneghetti, 2012, Hentschel et al., 2016).

Figure 2.1: The Lycurgus cup for the Roman Empire, demonstrating the bright red colour of Transmitting light through gold nanoparticles.

Today, the electromagnetic (EM) properties of metal-dielectric structures are attracting considerable attention in the realms of science and nanotechnology, tracing back to the seminal works of Gustav Mie (1908) and Rufus Ritchie (1957) on small metal particles and flat surfaces. The development of these properties due to interactions has surpassed imagination, leading to crucial applications based on plasmonic structures in contemporary times. The potential applications span a wide range of areas, including optical sensors (Tittl et al., 2011, Lochbaum et al., 2017b, Li and Valentine, 2014), hot-electron photodetectors (Brar et al., 2015), optical modulators (Miyoshi et al., 2018, Yao et al., 2014, Sakat et al., 2018, Zhu et al., 2017, Inoue et al., 2016), high-speed switching (Li and Fan, 2018), energy recycling (Woolf et al., 2018, De Zoysa et al., 2012, Makhsiyan et al., 2015), image encryption (Bakan et al., 2018, Tittl et al., 2015), and thermal imaging (Li et al., 2014).

Furthermore, in 1898, the first metamaterial was proposed by Bose, the father of condensed matter physics. Who proposed changing the polarisation of light by twisting conductor elements (Bose, 1898). Other works (Kock, 1946) later implicitly supported such ideas. However, that concept was developed in 1996, when Sir John Pendry demonstrated tunable plasma frequency achieved by a metal wire array (Pendry et al., 1996). Later, the idea grew, leading to the establishment of the field of metamaterials. The main achievements of metamaterials can be better comprehended by looking at the possibilities in permittivity and permeability values. There are two main types of metamaterials depending on which light component will be coupled. If the interaction between light and material comes from the

magnetic component, we can consider that structure magnetic metamaterial. However, if the coupling is due to the electric component, it is electric metamaterials.

2.2   Plasmonics and metamaterials

Plasmonics and metamaterials are defined in this thesis as an optical domain in which surface plasmons exhibit excitability and propagate. This field originated in 1902, and the study of surface plasmons initially focused on the so-called Wood anomalies. These anomalies manifest as rapid variations in the intensity of diffracted spectral orders in narrow frequency bands when light is diffracted by diffraction gratings. Wood's anomalies are widely recognized as among the most fascinating optical phenomena of the twentieth century. Following Wood's discovery, plasmonics gained significant attention, making it an essential component of nanophotonics today. This field encompasses various aspects, including extraordinary light transmission through subwavelength-scale holes, the utilisation of surface plasmon polaritons (SPPs) for super lenses, and the development of very compact, high-speed, low-power, and interference-free optical devices for the telecommunications industry. Many studies based on plasmonics have concentrated on periodic structures. However, it is essential to note that numerous investigations have also explored the effects of SPP excitation on non-periodic rough surfaces, especially uneven surfaces. Before going deeper into plasmonic and metamaterials, let us examine the elements-components of active and fast-tunable plasmonic metamaterials.

2.3   Plasmonics Nanophotonics

Plasmonics is a branch of nanophotonics, and it has attracted considerable attention due to its interest in technologies linked to the strong development of nanophotonics. It typically involves generating, detecting, and controlling light at optical frequencies or wavelengths along metal and dielectric interfaces on the nanoscale. Considering the fields of optics that have defined the behaviour and properties of light, including the interaction of light with matter and the construction of instruments that detect light, such as lenses, mirrors, prisms, beam splitters, etc., all these elements have dimensions more significant than the wavelength of light. However, the photonics field, a subcategory of optics, can bring the size comparable but experience a diffraction limit below 1μm. One of the primary goals of plasmonic nanophotonics is to create optical instruments that can focus light from a point source much more tightly than the diffraction limit. These enabled researchers to investigate how the electromagnetic (EM) field can be confined over a length comparable to or less than the

wavelength of light to achieve strong plasmon localization, which may improve the optical area based on nanostructures.

Plasmonics involve the study of light behaviour on the nanometer scale and the interaction of light with matter on the subwavelength scale. It offers exceptional insights into the THz window within the nano-scale range. Additionally, it reduces device footprint by confining light in ultra-small volumes, thereby enhancing light interaction with materials of interest and reducing energy consumption. Regarding relationships with metamaterials, the optical properties of metamaterials are determined by plasmonic resonances, which are related to the collective oscillations of electrons in metallic nanostructure within the material. These resonances are responsible for manipulating and controlling light at the nanoscale. By engineering the structure and composition of metamaterials, researchers can carefully control and engineer metamaterial optical properties, enabling functionalities that are not achievable with naturally occurring materials.

2.3.1 Passive Plasmonic Components

Passive plasmonic components refer to elements that use plasmonic effects but do not require an external power source for their operation. These components manipulate and control light using structures designed to interact with electromagnetic fields at the nanoscale. They can perform functions such as guiding, manipulating, and detecting light. Such components can be found in various fields such as photonics, telecommunications, sensing, and imaging due to their ability to manipulate light at extremely small scales, enabling functionalities not feasible with conventional optics. The plasmonic facilities are used to localize electromagnetic waves, with efficient photon and plasmon transformations controlled at the sub-wavelength scale (Xu et al., 2010, Gramotnev and Bozhevolnyi, 2010).

2.3.2 Active Plasmonic Components

Active plasmonic lies under the fundamental principles of active plasmon control. It requires an external energy source or control mechanism to modify the behaviour of light at the nanoscale. These components often employ active materials, such as semiconductors or other tunable materials, to actively control and manipulate light properties like intensity, wavelength, phase, or direction. The modulation mechanisms of most active plasmonic structures rely on controlling the plasmonic components or their surrounding media, offering great flexibility and

opening numerous application opportunities. Active plasmon control utilises surface plasmon resonance (SPR) to manage the interaction of light between metal and dielectric material interfaces. The electromagnetic wave induces electron oscillation at the interface, where these electrons can propagate along a planar interface as surface plasmon polaritons (SPPs) or be confined within a subwavelength structure as localised surface plasmon resonance (LSPR). Both types of SPR can influence incident electromagnetic waves at a deep subwavelength scale, leading to a significant enhancement of the local field and enabling manipulation of light below the diffraction limit. This review presents an initial in-depth account of the theoretical relationship between surface plasmon resonance (SPR) and its influencing elements, serving as a foundation for active plasmon control. For instance, electron density excitations along a metal-dielectric interface (Maier, 2007, Sharma and Gupta, 2005) are known as surface plasmon polaritons (SPPs).

Plasmonic achievements in photonics technologies and optical interconnects, such as fibre optic cables, can transport digital data at a capacity that is over a thousand times that of electronic interconnects. The two-component device is necessary for technological advancement, but combining them on the same circuit is challenging. By exploiting plasmonic nanophotonics, transporting optical signals and electric currents through the same thin metal in nanoscale circuits is possible (Sorger et al., 2012, Krasavin and Zayats, 2015, Ozbay, 2006). One of these ideal solutions is surface plasmons (SPs) (Nicolas et al., 2015, Gong et al., 2013b, Krasavin and Zheludev, 2004, Vasa et al., 2014, Ambati et al., 2008, Raether, 1988b, Ritchie, 1957, Economou, 1969, MacDonald and Zheludev, 2010, Krasavin and Zayats, 2015), where the interaction of light with a material interface led to a new branch of photonics called plasmonics.

Consequently, plasmonics is one of the most exciting and rapidly developing areas of photonics, as it focuses on the optical properties of metallic nanostructures. Electromagnetic waves can be confined to a small volume in a plasmonic field, and efficient photon-to-plasmon conversion can be manipulated (Xu et al., 2010, Gramotnev and Bozhevolnyi, 2010). Noble metals, gold, and silver are commonly used plasmonic materials at visible (VIS) and near-infrared (NIR) ranges. The materials with plasma frequencies are needed to exploit plasmonic enhancement in mid/far-infrared waves.

2.4 Thermal Photonics Metamaterials

Thermal photonics are photonic structures that are intended to manipulate thermal emission. The emitters utilise photonic structures with significantly different properties than conventional thermal radiators. Conventional thermal radiators emit radiation across a broad frequency spectrum, which means they release electromagnetic radiation at various wavelengths due to the thermal energy of the emitting object. However, the emission is subject to fundamental physical laws, such as Planck's law of thermal radiation. Planck's law of thermal radiation describes the spectral density of thermal emission per unit area at a given temperature. It establishes the relationship between the temperature of an object and the distribution of emitted radiation across different wavelengths. According to Planck's law, the spectral density of thermal emission is limited and follows a specific distribution curve, with higher temperatures resulting in higher-intensity emissions at shorter wavelengths. In addition, thermal radiators are typically governed by Kirchhoff's law, which states that the angular spectral absorption and emissivity must be equal. These attributes and constraints severely limit the capacity of conventional structures to control thermal radiation.

Regarding technological investigation, plasmonic nanophotonics offers exceptional opportunities to tailor the absorption of a target material to modify its thermal emission spectrum based on Kirchhoff's law. Since then, different methods to control and manipulate thermal emission based on nanostructures have been developed. Most studies emphasise control of the spectral properties of thermal emission, which generates a variety of applications, such as radiative cooling (Hsu et al., 2016, Zhou et al., 2019, Bhatia et al., 2018), where the cooling strategy with zero consumption of electricity that can be used to radiate heat from buildings to reduce air-conditioning requirements. This technology can work well during optimal atmospheric conditions at night, and it is important to achieve efficient cooling during the daytime when peak cooling demand occurs. Also, can be in solar technology exploits the angular confinement of solar treatment in the sky to achieve sub-ambient cooling during the day regardless of the emitter properties in the solar spectrum (Bhatia et al., 2018). Thermophotovoltaic devices (Lenert et al., 2014) these methods are used to create power from sunlight, either photovoltaic (in which sunlight directly triggers electron-hole sets in a semiconductor) or solar thermal (in which sunlight drives a mechanical heat engine), as depicted in Figure 2.2.
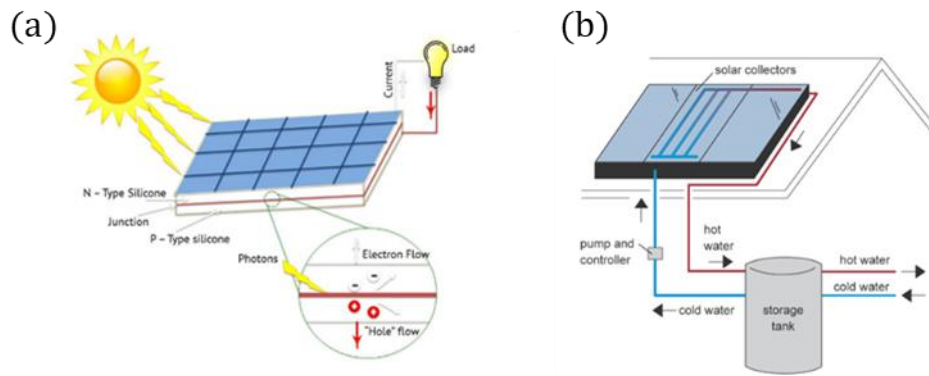
Figure 2.2: (a) photovoltaic system for electricity (b) solar thermal system for sunlight mechanical heat

Moreover, other essential technologies are thermal camouflage (Qu et al., 2018, Li et al., 2018) and thermal imaging (Ring and Ammer, 2012). These technologies are significant, especially for the development of multi-physical fields along with applications like electromagnetic communication (Fleury and Alu, 2014), military weapons (Lyu et al., 2019, Yu et al., 2014), anti-counterfeiting (Franklin et al., 2018), coating materials (Dang et al., 2019, Li and Zhu, 2018), temperature control (Hong et al., 2020, Lang et al., 2018), robot transformers (Bauer et al., 2014, Li et al., 2019, Morin et al., 2012). In thermal imaging, the infrared camera converts detected radiative energy into electrical waves to display a simulated temperature field, allowing to "see" the environment at night. Because all objects emit thermal waves in a radiative manner, thermal waves are considerably easier to expose in the infrared camera against the background temperature. As a result, many modern cars and military weapons have been used with these technologies. Thermal camouflage solutions are required to conceal targets in the infrared camera by tailoring the thermal radiation to be the same or similar to the backdrop environment.

The thermal camouflage technique is increasingly popular for various thermal applications that can hide or disguise an object in the background (Han et al., 2014), such as a person, an animal, or a piece of equipment. Regarding the basic mechanisms behind it, these technologies can be divided into two categories: colour camouflage and thermal camouflage. Colour camouflage is achieved by modifying light reflection or transmission to match the look of the object to the surroundings in the visible or near-infrared range (Phan et al., 2013, Yu et al., 2014, Wang et al., 2016). On the other hand, thermal camouflage uses thermal emission to match the radiation temperature of a specific object with that of the background. As a result, thermal disguises can trick thermal imagers, which differentiate objects from the environment based on their radiation temperature difference. Because of the radiation temperature differential between the object

and the backdrop, thermal imagers can quickly detect the object when the background temperature changes, as shown in Figure 2.3.
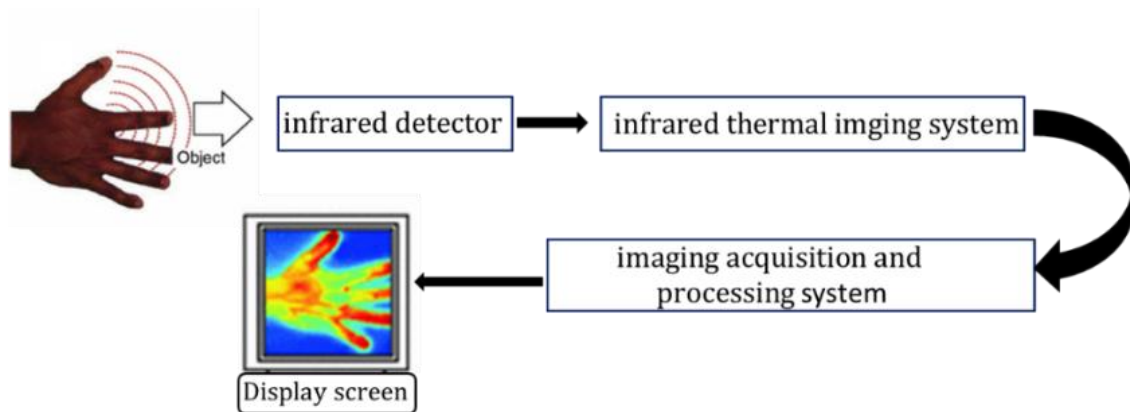
Figure 2.3: The thermal imaging processing, where the infrared radiation emitted from an object is focused on an infrared detector. The detector sends the information to sensor electronics for image processing. The electronics translate the data from the detector into an image that can be viewed on the viewfinder screen.

2.4.1   Thermal Radiation Source

According to the fundamental principles of statistical mechanics, every hot object emits electromagnetic radiation. Sunlight and the radiance of an electric oven and embers in a fire are examples of thermal emission sources. The fundamental physics of thermal emission from hot objects has been well understood for over a century, as described by Planck's law. Ideally, thermal radiation is an electromagnetic wave generated from the thermal motion of particles in matter. The radiation wave from the thermal body is essential in science and technological applications such as security, healthcare, telecommunications, etc. The thermal radiation spectrum possesses the emission of electromagnetic waves with a temperature greater than absolute zero, and an object with a temperature greater than absolute zero can emit thermal waves. Most of the emission waves at room temperature are infrared. The thermal emission light source, such as a blackbody or an incandescent light bulb, is essential locally and has been studied. Typically, it is omnidirectional and broadband in nature.

The desire to convert thermal broadband to narrowband has long been a research topic. Planck's law (1978) describes how a blackbody absorbs and emits a broad spectrum of electromagnetic radiation determined by its temperature. Increasing the blackbody's temperature increases the intensity of the emitted radiation. Therefore, objects at non-zero temperatures can radiate electromagnetic energy. The fundamental property of generating thermal emission waves compared to a blackbody is determined by its optical absorptivity (Planck, 1978). The connection between optical absorption and thermal emission, linked to the

time reversibility of microscopic processes, suggests that the temporal and spatial coherence of the thermal emission can be engineered via reasonable material selection and patterning.

2.4.2   Thermal Spectral Control

The spectra control of the thermal emission refers to the manipulation of the distribution of thermal energy emitted or absorbed by a structure across various wavelengths within the electromagnetic spectrum. Emitters that exhibit significant thermal emission in the required wavelength range while emitting little background light are extremely useful as efficient light sources for sensing and illumination. Controlling the thermal emission spectra of emitters, on the other hand, has captured the interest of researchers due to the need for increased energy utilisation efficiency in various fields such as lighting, energy harvesting, and sensing. Limiting the emission spectrum to a degree just below the bandgap wavelength of the target photovoltaic cell is critical for highly efficient solar thermophotovoltaic energy conversion. Controlling the emissivity or absorptivity spectra in radiative cooling applications is thus beneficial. Considerable effort has been devoted to engineering thermal emission (Fan, 2017, Li and Fan, 2018) using nanostructures. Several innovative examples have been reported and constructed with surprisingly varied thermal emissions properties, such as coherent, direct, polarised, narrowband thermal light sources and wavelength-selective emitters. These innovative thermal emitters have great promise for essential applications such as thermophotovoltaics (TPV), solar energy concentration, radiative cooling, thermal detection and sensing, novel light sources, thermal rectification, etc. We provide a preliminary study of the use of nanostructures to control thermal emission and encompass various techniques aimed at changing the characteristics of thermal radiation, such as emissivity, spectral distribution, and directionality of emission.

2.4.3   Fast Thermal Modulation

Fast thermal modulation is helpful for detection or communication applications, but it is still challenging due to thermal inflexibility. By introducing nanostructure, thermal inflexibility can be controlled and reduced (Mori et al., 2014). The fast modulation thermal emitter is explained by the extremely fast temperature response, which is dominated by a small heat capacity. High-speed light emitters integrated on-chip graphene blackbody emitters were also reported for optical communications. The graphene's contact with the substrate strongly affects its emission responses, depending on the number of graphene layers. The ultra-high-speed emission can be

explained by remote quantum thermal transport via surface polar phonons of the substrates (Miyoshi et al., 2018).

Furthermore, high-speed light modulation was reported using complex refractive index changes of electro-optics polymers. The high-glass-transition-temperature active-polyimide thin film was used in this study (Harada et al., 2000). Therefore, observing the compound semiconductors, such as light-emitting diodes (LEDs) and laser diodes (LDs), are also used for higher-speed optical communication with the optical modulators as external E/O converters. However, due to their large footprints, the low crystallinity of compound semiconductors grown directly on Si wafers, and the sophisticated device structures associated with p−n junctions and bandgap engineering (Liang and Bowers, 2010), these emitters face considerable challenges with respect to their integration with silicon-based electronics, photonics, and micromechanical platforms. The blackbody emitter, which is related to Joule heating, has a broad temperature-dependent spectrum that is given by Planck's law (Planck, 1901) in contrast to LDs and LEDs, which have sharp emission peaks that are related to the bandgap.

2.5 Mid-Infrared Thermal Emissions

Mid-infrared wavelengths have various technologically essential applications, including molecular sensing, security and defence, energy conservation, and free-space communication. The recent development and rapid commercialisation of new coherent mid-infrared sources have renewed many interests in developing mid-infrared optical systems for the abovementioned purposes. The mechanisms of these windows can be a blackbody or an incandescent source and have long been studied as an incoherent phenomenon due to the uncorrelated properties of spontaneous emission. Thermal sources such as hot membranes and globars are commonly used in the infrared spectrum. The emission properties of these sources can be tailored and used to control the spectrum, polarisation, and directivity. The mid-infrared wavelength is the portion of the electromagnetic spectrum that extends from the long wavelength of the telecommunication to the short wavelength of the THz. As a result, artificial control of thermal emission on mid-infrared spectral, which is difficult to achieve with natural materials, has been a research topic of interest for decades. The principle of controlling thermal emission is based on Kirchhoff's law, where emission and absorption are identical.

Fundamentally, the mid-infrared is a wavelength range that allows a wide range of light-matter interactions to be studied and engineered. Interaction with free carriers, the foundation of

plasmonics and many metamaterial structures, is controlled by defining the geometry of metallic optical structures and using 'designer' materials to engineer the optical properties of the metals themselves. Because of the low energies of most mid-infrared photons, traditional optoelectronic semiconductor materials with band gap energies well above the energy of most mid-infrared photons can be used as high-index and low-loss dielectrics. With careful band structure engineering, these materials can also provide designed optical transitions and enhanced optical nonlinearities. Various methods for controlling such mid-infrared thermal emissions based on nanostructures have been developed significantly, and thermal emitters are temporally and spatially coherent (Carminati and Greffet, 1999, Greffet et al., 2002a). However, spatially and temporally coherent thermal emitters are quasi-directional and narrowband because the thermal emission is directional at some specific wavelength and narrowband within some particular direction. Several structures have been proposed to control thermal emission spatially and temporally, such as gratings (Greffet et al., 2002a, Qu et al., 2016a) and vertical cavity-enhanced resonant thermal emitters (Celanovic et al., 2005) have been proposed to control the thermal emission spatially and temporally. In the presence of directional and narrowband emitters, the thermal emission is confined within the narrow bandwidth and narrow angular width. When matched with a conventional narrowband thermal emitter, this directional and narrowband emitter can achieve a higher equilibrium temperature and higher energy-conversion efficiency. Another figure of merit is directional and broadband thermal emitters, such emitters can emit in a specific direction within a broad wavelength range and be used for directional radiative cooling in the surrounding area (buildings).

2.6 Conclusion

This chapter provided a comprehensive theoretical background on plasmonics and metamaterials, which led to the discovery of the optical properties of metal nanostructures. Investigates the historical account of metamaterials, dating back to their initial mention in 1898, including active and passive components of plasmonic devices designed to manipulate and control light at subwavelength scales. Kirchhoff's law (which states the angular spectral absorption and emissivity must be equal) was used to demonstrate that the thermal photonic metamaterials' emission spectrum can be modified. The investigation of thermal photonics was focused on thermal emission properties, including technological investigation based on thermal radiation modification techniques. The mid-infrared thermal emission is discussed in technological applications such as molecular sensing, security and defence, energy

conservation, and free-space communication. The mid-infrared is a wavelength range that allows a wide range of light-matter interactions to be studied and engineered.

Chapter 3
Theoretical Framework

This chapter focuses on the fundamental principles of plasmonic metamaterials concerning their interaction with materials of interest. Maxwell's equations are employed to justify wave propagation through materials, particularly in the study of artificial materials, known as metamaterials. This exploration covers material classification, electromagnetic fields for polarisation states, surface confinement (SP), and localised surface plasmons for spectral tunability. Collectively, these elements form the framework for active and fast-tunable plasmonic metamaterials.

3.1 Maxwell's Equations

Electromagnetic waves are transverse plane waves, which can easily derive from the Maxwell equations in an infinite media without sources. We show the derivation formal of such waves, which are essential in knowing the propagation behaviour for any other polarisation state of an electromagnetic wave. Maxwell's equations justify how these waves can physically propagate through media. For example, a changing magnetic field creates a changing electric field through Faraday's law. Maxwell's correction to Ampère's law causes this electric field to generate a fluctuating magnetic field. This continual cycle enables these waves, now known as electromagnetic radiation, to move through media at velocity (c).

$$\nabla \cdot \boldsymbol{D} = \rho \qquad \qquad 3.1$$

$$\nabla \cdot \boldsymbol{B} = 0 \qquad \qquad 3.2$$

$$\nabla \times \boldsymbol{E} = -\frac{\partial \boldsymbol{B}}{\partial t} \qquad \qquad 3.3$$

$$\nabla \times \boldsymbol{H} = J + \frac{\partial \boldsymbol{D}}{\partial t} \qquad \qquad 3.4$$

The equations linking the four macroscopic fields are:
- ✓ Gauss's law of electric field (3.1).
- ✓ Gauss's law of magnetic field (3.2).
- ✓ Faraday's law of electromagnetic induction (3.3).
- ✓ Ampere's law of electric displacement (3.4)

The field parameters that appeared in the equations include, D is the electrical displacement in coulombs/meter² (C/m^2), B is the magnetic flux density or induction (Wb/m^2), E is the electric field strength in volts/meter (V/m), and H is the magnetic field strength in amperes/meter (A/m). The rho (ρ) and (J) letter is the surface density, J for current and ρ for charges. In a region with no charges $\rho = 0$ and no currents $J = 0$, such as in a vacuum/free space. The vector relation for the electric field quantities, E and D and the magnetic field quantities, H and B are independent quantities. The equation that constitutes the connections, Maxwell's equation, described as the time-varying electric field, will rise to the magnetic field and vice versa. The polarisation (P) and the magnetisation (M) connect the four macroscopic fields. The connection between the two disciplines is related to material properties. The relationships between these independent quantities must be specified to comprehend these properties. These independent quantities contribute to the bound charge and current response to the applied fields and are called constitutive relations. The relations between constitutive and optical medium were stated in equations 3.5 and 3.6, respectively.

$$D = \varepsilon E = \varepsilon_0 E + P \qquad 3.5$$

$$B = \mu H = \mu_0 H + M \qquad 3.6$$

Where ε is the electric permittivity of the medium, μ is the magnetic permeability of the medium, ε_o is free space permittivity ($8.85 \times 10^{-12} \ c^2 N^{-1} m^{-2}$), and μ_o is the permeability of free space ($4\pi \times 10^{-7} \ H/m$). In addition, the polarisation density vector P, is defined as the electric dipole moment per unit volume within the material. At the same time, the density of magnetic dipole moments in the material is described by the letter M, as a magnetisation of the optical medium. Subsequently, by examining Maxwell's equation, all other variables are independent of the optical medium. Still, only M and P, are defined as optical mediums because of light behaviour interaction in the medium determent by M and P response. Another important linear relationship is internal current density J and the electric field E, which is defined through the conductivity ($\sigma(\omega)$) by:

$$J = \sigma(\omega)E \qquad 3.7$$

The interaction between light and matter is generally electric, so the medium can be assumed to be non-magnetic without free charge. Therefore, the parameters M, J and ρ equal to zero and the condition of equation 3.1 - 3.4 is re-arranged as:

$$\nabla \cdot D = 0 \qquad 3.8$$

$$\nabla \cdot \boldsymbol{B} = 0 \tag{3.9}$$

$$\nabla \times \boldsymbol{E} = -\mu_0 \frac{\partial \boldsymbol{B}}{\partial t} \tag{3.10}$$

$$\nabla \times \boldsymbol{H} = \varepsilon_o \frac{\partial \boldsymbol{D}}{\partial t} \tag{3.11}$$

Considered the absence of magnetic or dielectric materials. In that case, the constitutive relations can be simplified as $\boldsymbol{D} = \varepsilon_o \boldsymbol{E}$ and $\boldsymbol{H} = \boldsymbol{B}/\mu_o$, and the currents and charges are substituted with free currents and charges. In an isotropic linear material, $\boldsymbol{P}$ is proportional to $\boldsymbol{E}$, and $\boldsymbol{M}$ is proportional to $\boldsymbol{B}$; the constitutive relations are also straightforward. By considering polarisation $\boldsymbol{P}$ and the magnetisation $\boldsymbol{M}$ defined using the dielectric susceptibility $(\chi_e(\omega))$, and expressed as:

$$\boldsymbol{P} = \varepsilon_o \chi_e(\omega) \boldsymbol{E} \tag{3.12}$$

$$\boldsymbol{M} = \chi_m(\omega) \boldsymbol{H} \tag{3.13}$$

Where $\chi_e(\omega)$ and $\chi_m(\omega)$ are the electric and magnetic susceptibilities of a given material and the relative susceptibilities based on permittivity and permeability defined as $\varepsilon = \varepsilon_o(1 + \chi_e(\omega))$ and $\mu = \mu_o(1 + \chi_m(\omega))$.

The derivation of the wave equation for E-field by considering equation 3.10 and substituting equation 3.11 with $(\boldsymbol{J} = 0)$

$$\nabla \times \nabla \times \boldsymbol{E} = -\mu \frac{\partial \boldsymbol{H}}{\partial t} \nabla \times \boldsymbol{H} = -\mu\varepsilon \frac{\partial^2 \boldsymbol{E}}{\partial t^2} \tag{3.14}$$

And $\nabla \times \nabla \times \boldsymbol{E}$ can be defined in terms of vector identity as $\nabla(\nabla \cdot \boldsymbol{E}) - \nabla^2 \boldsymbol{E}$. Therefore, equation 3.14 would become:

$$\nabla^2 \boldsymbol{E} - \mu\varepsilon \frac{\partial^2 \boldsymbol{E}}{\partial t^2} = 0 \tag{3.15}$$

$$\nabla^2 \vec{H} - \mu\varepsilon \frac{\partial^2 \boldsymbol{H}}{\partial t^2} = 0 \tag{3.16}$$

Substituting the above form of $\boldsymbol{E}$ and $\boldsymbol{H}$ into the appropriate wave equation leads to the identification of the wave velocity and is described as:

$$v = \frac{1}{\sqrt{\varepsilon\mu}} = \frac{\omega}{k} = \frac{c}{n} \tag{3.17}$$

The wave equation determines the velocity (v) of propagation for the EM wave. It is a function of the permittivity and permeability of the space or materials in which the wave exists. However, the relationship between the wave number (k) and the frequency (ω) can be an expression as:

$$\boldsymbol{k} = \omega\sqrt{\mu\varepsilon} \qquad 3.18$$

This relationship gives rise to the definition of phase velocity (v_p) and the refractive index (n), The frequency component in wave propagation is described by the phase velocity of a wave, which is controlled by the refractive index. In general, the phase velocity is a complex function of frequency, and equation 3.17, rewritten as:

$$v_p = \frac{\omega_0}{k} = \frac{c}{n^{\omega_0}} \qquad 3.19$$

Moreover, the group velocity (v_g) can also be described as a change in the frequency of the wave ($\partial\omega$) divided by the change in its wave number (∂k).

$$v_g = \frac{\partial\omega}{\partial k} = \frac{c(\omega_2-\omega_1)}{n^{\omega_2}-n^{\omega_1}} \qquad 3.20$$

Also, the energy that flows in space is given by Poynting's vector,

$$\boldsymbol{P}_t = \frac{1}{\mu}\,\boldsymbol{E}\times\boldsymbol{H} \qquad 3.21$$

Where μ is the permeability of the media through which the wave exists, E is the amplitude of the electric field, and H is the magnetic field. The two velocities v_p and v_g, describe different properties of wave movement, the distinction between them is single wave propagation on v_p , and envelope wave propagation on v_g. A plane-wave equation can be described as follows:

$$\boldsymbol{E}_z(\omega) = \boldsymbol{E}_{xz}(\omega)\boldsymbol{H}_{yz}(\omega) \qquad 3.22$$

Where $E_{xz}(\omega)$ is the electric field in the x-direction, and $H_{yz}(\omega)$ is the magnetic field in the y-direction.

The complex refractive index ($n\,(\omega)$), can therefore be described as:

$$n(\omega) = n + jk = \sqrt{\varepsilon\mu} \qquad 3.23$$

The impedance of the medium can be described as,

$$\eta = \sqrt{\frac{\mu}{\varepsilon}}$$

<div align="right">3.24</div>

Therefore, consider equation 3,23; the real part of the refractive index $n(\omega)$ is responsible for the dispersion in the medium, and the imaginary part $k(\omega)$ is responsible for the absorption (extinction coefficient). The complex $k(\omega)$ can be written as $k = k' - jk''$, when there's a loss, the real $k'(\omega)$ is responsible for the oscillation waves and the imaginary $k''(\omega)$ is for the decay. The wave propagation is based on the frequency-dependent dielectric constant $\varepsilon = \varepsilon(\omega)$, which is, in general, a complex function as:

$$\varepsilon(\omega) = \varepsilon'(\omega) + j\varepsilon''(\omega)$$

<div align="right">3.25</div>

Where the real part is identified as:

$$\varepsilon' = n^2 - k^2$$

<div align="right">3.26</div>

The imaginary part is also identified as:

$$\varepsilon'' = 2nk$$

<div align="right">3.27</div>

$$n^2 = \frac{\varepsilon'}{2} + \frac{1}{2}\sqrt{\varepsilon'^2 + \varepsilon''^2} \qquad\qquad k = \frac{\varepsilon''}{2n}$$

<div align="right">3.28</div>

3.2 Bulk Plasmons

Bulk plasmons are collective electron oscillations that occur in three-dimensional materials, usually within the bulk. These oscillations are characterised by their dispersion relation and are closely associated with the movement of free electrons in conductive materials. When studying wave propagation in a vacuum, we always investigate transverse waves. The optical properties can be described over a broad frequency range using the plasma model, which assumes a high-density electron gas that propagates freely behind a positively charged atom background. In the stable state, the positive atoms and electrons within the bulk metal will cancel each other, rendering the metal neutral. The free electrons oscillate longitudinally when an external field is applied to the metal. These oscillations appear at a frequency known as the plasma frequency, (ω_p) (Borys, 2011). As described in more depth, this ω_p, is transparent to radiation with higher frequencies and non-transparent with lower frequencies. Bulk plasmons cannot be excited by photons due to the mismatch between the longitudinal oscillation of free electrons in metals

and the transverse oscillation of light. In contrast, electron beams can excite bulk plasmons (Amendola et al., 2017).

Therefore, from a general perspective, the solution of the longitudinal waves satisfies $\nabla \times \mathrm{E} = 0$, which we studied in Equation 3.8. Furthermore, the Maxwell equations without using a specific medium model. Assuming the medium is linear, homogeneous, and isotropic. The most general linear form determines the frequency and wave vector under the constitutive relation with the spatial dependency.

$$\boldsymbol{D}(\omega, k) = \varepsilon(\omega, k)\boldsymbol{E}(\omega, \boldsymbol{k}) \qquad 3.29$$

The dependence on (ω) is called dispersion, and the dependence on (k) is called spatial dispersion. This dependence on the wave vector leads to a non-local relation between the electric field and the vector D in direct space so that spatial dispersion and non-local dielectric constant are two aspects of the same property:

$$\boldsymbol{D}(\omega, r) = \int \frac{\partial k}{8\pi^3} \varepsilon(\omega, \boldsymbol{k}) \boldsymbol{E}(\omega, \boldsymbol{k}) \exp(j\boldsymbol{k}.\boldsymbol{r}) = \int \varepsilon(\boldsymbol{r} - \boldsymbol{r}', \omega) E(\omega, \boldsymbol{r}') \partial \boldsymbol{r}' \qquad 3.30$$

Then Equation 3.29 can be cast in the form of:

$$\boldsymbol{\nabla} \cdot \boldsymbol{D} = \boldsymbol{\nabla} \cdot \int \frac{\partial k}{8\pi^3} \frac{\partial \omega}{2\pi} \varepsilon(\omega, \boldsymbol{k}) \boldsymbol{E}(\omega, \boldsymbol{k}) \exp(j\boldsymbol{k}.\boldsymbol{r} - j\omega t)$$

$$= \int \frac{\partial k}{8\pi^3} \frac{\partial \omega}{2\pi} \varepsilon(\omega, k) [j\boldsymbol{k} \cdot \boldsymbol{E}(\omega, \boldsymbol{k})] \exp(j\boldsymbol{k}.\boldsymbol{r} - j\omega t) = 0 \qquad 3.31$$

For additional information, see the reference (Aizpurua and Hillenbrand, 2012). If we take a non-zero longitudinal electric field, then $\boldsymbol{k} \cdot \boldsymbol{E}(\boldsymbol{k}, \omega) \neq 0$, then $\varepsilon(\omega, \boldsymbol{k}) = 0$. Additionally, If the medium has a dielectric constant that does not depend on k, then the dispersion relation of the longitudinal waves is given by $\varepsilon(\omega) = 0$. For the particular case of a non-lossy Drude model, $\varepsilon(\omega) = \varepsilon_0(1 - \omega_p^2/\omega^2)$ then we find $\omega = \omega_p$ (Aizpurua and Hillenbrand, 2012).

3.3   Surface Plasmons

Surface plasmon is a collective oscillation of electrons in solid-state physics that occurs at the interface between conductive materials, typically a metal (gold, silver) and a dielectric material, usually glass or air. The fundamental coupling concept of the surface waves is surface plasmons (SPs), it is coherent delocalised electron pulses that exist at the interface of two materials where the real part of the dielectric function's changes sign across the interface (Barnes et al., 2003,

Krasavin et al., 2005). It can have the ability to confine electromagnetic energy to subwavelength scales, allowing for manipulation and control of light at dimensions smaller than the diffraction limit of light. Also, it enables enhanced light-matter interactions, such as increased light absorption, scattering, and field localisation, which are important in applications like sensing, spectroscopy, and nanophotonics.

Surface plasmon describes polarisation oscillations of metallic nanoparticles and waves propagating along a plane interface and exponentially decaying away from the interface. SPs are a type of surface wave in electrodynamics, studied since the early days of radio wave propagation along the earth (Baños, 1966, Brekhovskikh, 1960, Felsen and Marcuvitz, 1994, King et al., 1992). Optics are modes of interface studied in the 1970s and 1980s. Numerous excellent articles are available from this perspective (Agranovich, 2012, Ghoshal and Kik, 2008, Zayats et al., 2005), and more recent achievements are summarised in references (Zayats et al., 2005, Barnes et al., 2003, Schuller et al., 2010).

3.3.1 Polariton

A polariton is a coupled state resulting from the interaction between an elementary excitation (such as plasmons, phonons, and excitons) and a photon. When electromagnetic waves propagate through a material interface, they cause a mechanical movement of charges and the coupled excitation, forming a polariton. In the case of a metal, the field may correspond to a longitudinal charge density wave, observable in the electron gas as an acoustic wave, resulting in what is known as a plasmon polariton. In an ionic crystal, an electromagnetic field can excite the mechanical motion of ions, referred to as a phonon, inducing a polarisation oscillation known as a phonon polariton. On the other hand, the coupling between the field and an electron-hole pair gives rise to what is termed an exciton-polariton.

Furthermore, the interaction of the electromagnetic wave with a considerable interface generates an exciting surface excitation. This interaction between the density surface charge and the electromagnetic field results in the momentum of the SP mode k_{SP} will become more excellent than that free space photon at the same frequency $k_o, (where\ k_o = {}^{\omega}/_c$). Charge movement in a surface plasmon always generates electromagnetic fields outside and inside the metal. The total excitation, which includes the charge movement and the related electromagnetic field, is called surface plasmon polaritons (SPPs) for a planar interface or localised surface plasmons (LSPs) for a tiny particle's closed surface. Hence, the spatial

variation of the charge density along the surface of a conductor can occur on a scale smaller than the wavelength of light. SPs can effectively squeeze light into small, sub-wavelength volumes. In these volumes, the optical fields can be strongly enhanced far beyond the incident wave that excites the matter and effectively magnifies the light-matter interaction.

3.3.2   Surface Plasmon Polaritons

Surface plasmon polaritons (SPPs) are the hybridised excitations that arise at the interface between a conducting material and a dielectric material when stimulated by incident light. The unique characteristics of surface plasmon polaritons, namely enhanced and spatially confined fields, combined with innovations in fabrication technologies, led to improved interest in studying plasmonics for various applications (Barnes et al., 2003). SPs can be excited by electromagnetic radiation, and the resulting excitations are known as SPPs. The oscillating electric field from the incident light can be coupled with the surface plasmon resonances (SPR) or, more precisely, SPP at a metal-dielectric interface when the incident light momentum equals that of the plasmon (Coupling between plasmon and photon). In contrast to LSP, SPP does not occur unless the momentum of the electric field associated with incident light matches the SP of metal (Sui, 2012). The properties of SPPs are obtained from the solution of Maxwell's equations in each medium and the associated boundary conditions. A smooth semi-infinite metal and dielectric boundary can support propagating surface plasmon polaritons, and the dispersion of these modes is the relationship between frequency and spatial wavenumber.

$$k_{SPP}(\omega) = k_o \sqrt{\frac{\varepsilon_m(\omega)\varepsilon_d(\omega)}{\varepsilon_m(\omega)+\varepsilon_d(\omega)}} \qquad\qquad 3.32$$

where k_{SPP}, is the SPP wave vector, ω is the electromagnetic frequency, and $\varepsilon_m(\omega)$ and $\varepsilon_d(\omega)$, are the complex dielectric materials, ε_m, metal and ε_d, dielectric. In three-dimensional (3D) metal structures, volume plasmons can exist in the Bulk of the metal. The plasma frequencies here are transparent to radiation with higher frequencies and nontransparent to radiation with lower frequencies. These plasmons are longitudinal modes that cannot be excited by an incident photon (Maier, 2007). Propagating surface plasmon polaritons (SPPs) can be excited at the metals and dielectrics interface. Also, metal structures such as nanoparticles support various localised surface plasmon resonances (LSPRs). SPPs and LSPRs have a wide range of excitation mechanisms determined by the geometry and size of the plasmonic structures and the polarisation state of the incident EM wave.

Therefore, we demonstrate a simple design in Figure 3.1 (a) that contains a metal and dielectric interface. The excitation of the SPPs at the metal and dielectric interface for collective oscillations of the free electrons in the metal generates dispersive longitudinal waves that propagate along the interface and decay exponentially into both media, as illustrated in the figure for ∂_d and ∂_m. The propagation solutions obey the plane wave vector, $k_{SPP}(\omega)$ of Equation 3.32 describes the dispersion relation. Surface plasmon mode always lies beyond the light line and has stronger momentum than a free space photon of the same frequency. The dispersion curve of such a design in Figure 3.1 (b) indicates SPPs in a solid red line; the light in a vacuum or free space is displayed in a solid green line, and the effect of the momentum, which allows coupling to light, is illustrated by black-solid lines. Consequently, the SP can couple to incident light and modify the planar metal surface with gratings or indentations possible to conserve the momentum energy (Cheng and Ellis, 1989). Experimental simulations of this scenario have frequently been utilised to scatter SPPs from contact to detect them and launch plasmons in surfaces (López-Tejeira et al., 2007).
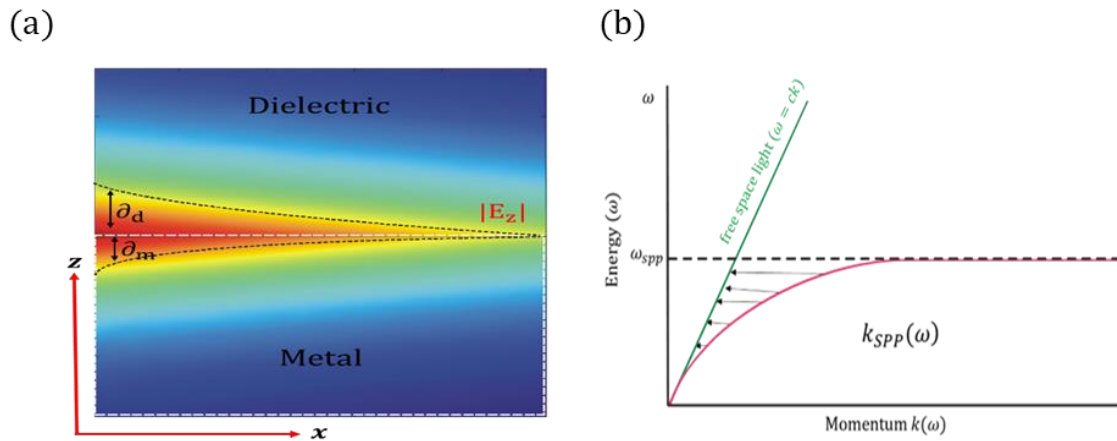
Figure 3.1: (a) The charge density oscillation model at the metal/dielectric interface, (b) the dispersion curve of the SPP

3.3.3 Surface Dispersion Theorems

The electric field obeyed the Helmholtz equation in both media under the dispersion relation for the non-magnetic cases and coupling. SPPs are surface charge density waves propagating along metal and dielectric interfaces. Surface dispersion theorems for SPPs define the relationship between the frequency, wavevector, and other material parameters, indicating how the SPPs behave at the interface. Light cannot be coupled directly to a flat metal surface if the

electron energy and momentum of the plasmon are not conserved simultaneously. The limitation of SPPs' excitation causes the surface plasmon to be predicted in the interaction of charges with thin metallic films (Ritchie, 1957). The plasmon excitation by fast electrons is possible due to the momentum transfer from those electrons that involves their velocity and energy. Light can also trigger SPPs, and there are several options for providing additional momentum, allowing for efficient generation and control of SPPs for various applications in photonics, sensing, and nanotechnology.

3.3.4   Waveguides Excitation

Waveguides can be in various shapes and materials, such as rectangular, circular, or dielectric. They serve as a pathway for guiding electromagnetic waves from one point to another while confining and controlling their propagation. The exciting waveguide involves introducing electromagnetic waves into the waveguide structure, allowing them to propagate along its length. This process can be achieved using different methods, including coupling devices such as lenses, gratings, or tapers, which efficiently couple external light sources, like lasers or optical fibres, into the waveguide structure. Plasmons at the conducting material and dielectric material interface can also be considered a mode propagating on a waveguide (Lal et al., 2007). The differences between these waveguides (long and short range) are propagation distances and waveguide design. The long-range SPP waveguides with propagation distances of a few tens of microns are described in the VIS up to hundreds of microns in the NIR range (Berini, 2009). The short-range SPP waveguides have propagation distances limited to tens of microns (Neutens et al., 2009). In this instance, the dispersion relations and thicknesses of the materials determine how propagating SPPs behave and how strongly they depend on the waveguide design. This propagation behaviour can be explained by the mode index of the waveguide, which explains the degree of confinement and the wave vector of the SPP.

$$k_{SPP}(\omega) = n_{\text{eff}} k_o(\omega)$$
$$\text{3.33}$$

Where the effective mode index n_{eff} can be used to describe the overall system propagation of SPPs. Because most dielectric materials exhibit little or no damping, the propagation behaviour is dominated primarily by the metal layer's properties. An example of long-range SPP waveguides is Insulator-Metal-Insulator waveguides, in which the metal layer is thinner than the skin depth, resulting in deficient confined modes with very long propagation distances (Berini, 2009). The Kretschmann configuration for SPP coupling also falls in the same class of

waveguide modes (Kretschmann and Raether, 1968). Short-range SPP waveguides are also Metal-Insulator-Metal waveguides in which the metal thickness is larger than the skin depth, resulting in highly confined modes with shorter propagation distances (Neutens et al., 2009).

Significant efforts have been made in the sensing field to measure the phase of propagating plasmons. It is possible to measure the phase difference by mixing P- and S-polarised waves for excitation (Kabashin et al., 2009). The P-polarised (TM-wave) can be competently coupled to a propagating SPP mode, whereas the S-polarised (TE-wave) is reflected without any significant phase change.

3.4 Localised Surface Plasmons

The oscillation of the surface charge density in metallic nanoparticles is usually known as localised surface plasmons (LSPs). The confinement of an SP in a nanoparticle is used to excite the plasmon when the oscillation frequency of electrons matches the frequency of incident electromagnetic waves. This resonance plasmon oscillation creates an absorption band in the visible region of the electromagnetic spectrum (Tabor, 2009, Rycenga et al., 2011), and this phenomenon is called Localised Surface Plasmon Resonance (LSPR) (Willets and Van Duyne, 2007).

However, the excitation of LSPR, including coupled and uncoupled, still relies highly on the wavelength and polarisation mode of the incident light. This interaction produces coherent localised plasmon oscillations with a resonant frequency that strongly depends on the composition, size, geometry, and dielectric environment. In contrast to the surface modes propagating along metal-dielectric interfaces, the LSPs are stationary oscillations of the surface charge density at optical frequencies along the boundaries of a metallic particle (Enoch and Bonod, 2012). Also, it is an essential element in generating subwavelength-enhanced electromagnetic fields, which can create, control and enhance physical processes such as vibrational spectroscopy (Xu et al., 1999), energy transfer, molecular sensing, photoemission, and imaging. Another vital element of the LSPs is that electric fields near the particle surface are significantly enhanced, and the particle optical absorption is limited at the plasmon resonant frequency. Surface plasmon resonance can also be tuned based on the shape of the nanoparticle. As shown in Figure 3.2, the electric field associated with incident light interacts with the metal nanoparticle, forming an electric dipole in which surface electrons move to one side of the nanoparticle. At the same time, the positive charge remains on the other. The resonance

frequency of the position of the LSPR absorption band is affected by several factors, including nanoparticle size, shape, and the dielectric of the surrounding media.
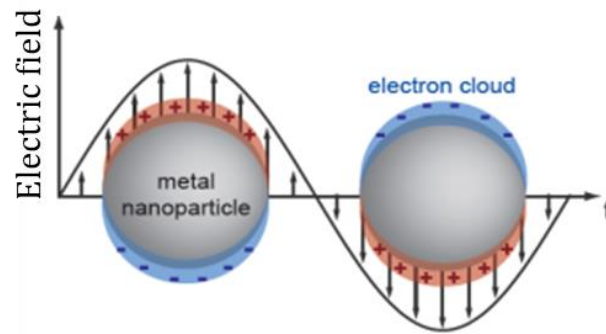
Figure 3.2: Schematic diagram illustrating localized surface plasmon resonance(Hutter and Fendler, 2004).

Numerous models, including the Lorentz model, the Drude model, and the Drude-Summerfeld model, have been applied to the interaction of electromagnetic radiation with the material (Fox, 2002, Trügler, 2011). The Lorentz model only applies to dielectric materials, whereas the other two use metals.

SPPs possess a near-field electromagnetic field that exists only at the metal and dielectric material interface and decays exponentially with separation into each medium. SPPs are extremely sensitive to their surrounding area and dramatically enhance the electric field. Light can propagate along the surface of the metal and coupled with the electron. Figure 3.4 shows the charge distribution associated with the electric field (Ebbesen et al., 2008). Since the dielectric function of metal strongly depends on the oscillation frequency. We stated Equation 3.32 of the dispersion relation as information data on the SPP properties of propagation and confinement. We demonstrated that changing the dielectric ε_a imaginary part can modify k_{SPP} and affect the coupling condition. These changes can affect the optical excitation efficiency of SPP, which can be observed by the intensity variation of the reflected light from the interface or of the transmitted light through the metal film. The results in Figure 3.3 generated the same contact as those in Figure 3.1 for the surface plasmon polariton guide. Figure 3.3 (a) illustrates the propagation mode along the *x*-axis, and Figure 3.3 (b) illustrates the mode charges associated with the electromagnetic wave at the metal and dielectric interface along the *y*-axis.
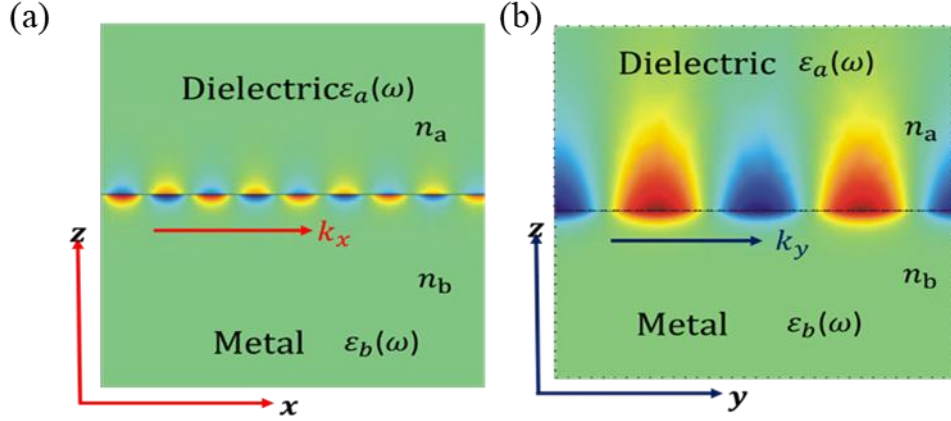
Figure 3.3: E-field lines and charge distribution for an SPP propagating at the interface between a metal and dielectric. (a) E-field propagation on x-direction and (b) E-field charge distribution modes at the interface between a metal and a dielectric.

At higher frequencies, the interaction between incident light and electrons in a metal changes, causing reduced absorption or diminished interaction in specific spectral ranges. This phenomenon may result in a degree of 'transparency', similar to decreased absorption in the metal at optical frequencies. In specific regimes, surface plasmon polaritons (SPPs) can also be referred to as Sommerfeld-Zenneck waves, representing a form of electromagnetic wave propagation along material interfaces. At large wave vector values (β), SPPs exhibit different properties, influencing their behaviour and interaction with incident light.

$$\omega_{sp} = \omega_p \sqrt{\frac{1}{1+\varepsilon_a}} \qquad\qquad 3.34$$

In the case of damped and undamped metal, the damped oscillations are responsible for attenuating along the propagation direction because the energy slowly dissipates via the metal heating. If the damping in the metal is introduced, the dielectric functions $\varepsilon(\omega)$ and $k(\omega)$ become complex. As a result, SPPs are characterised by a decay length (L_{SPP}) along their propagation direction. Let's consider the undamped metal for frequencies approaching ω_{sp}. The SPP wave vector $\beta \rightarrow \infty$ and the group velocity corresponding to the derivative of the dispersion relation $\partial\omega/\partial k$ is $v_g \rightarrow 0$. The model develops an electrostatic character and knows it is SP.

3.5 Metamaterial

Metamaterials attract attention not only for their exotic electromagnetic properties but also for their promising applications. These materials enable the independent control of electric and magnetic responses to incoming waves, creating unexpected phenomena. The fundamental

concept behind metamaterials revolves around manipulating material properties, specifically μ and ε. Research on metamaterials has expanded to encompass areas such as negative refraction and the complete customisation of ε and μ to achieve desired values for the refractive index, n, and medium impedance, η. The term 'meta' originates from the Greek word meaning 'above' or 'beyond.' When combined with 'material' to form 'metamaterial,' it implies that these materials are distinct from natural materials.

Metamaterials possess simultaneously negative real parts of electric permittivity and magnetic permeability. Unlike most materials, which typically have positive electric permittivity and magnetic permeability across a wide range of frequencies (referred to as 'double positive' materials), some materials exhibit either a single negative permittivity or a single negative permeability, as depicted in Figure 3.4. Metamaterials consist of periodic or non-periodic arrangements of sub-wavelength structures resembling metal atoms, known as composites. Numerous composite structures based on metamaterial through periodic repetition of metallic and dielectric elements have been established, and refer to these references (Xiao et al., 2009); (Soukoulis and Wegener, 2010); (Gansel et al., 2009); (Gao et al., 2013); etc.

3.5.1   Classification of Materials

Permittivity and permeability are two basic physical parameters of materials that characterise materials' response to electric and magnetic (Huang et al., 2007, Charles et al., 2021, Gou et al., 2018). According to the sign of these parameters, materials can be classified into four quadrants, as shown in Figure 3.4. According to the plot, materials that satisfy the first quadrant coordinate condition, such as air and water, crystals, and semiconductors, can be found in nature. Plasmonic material (Au and Ag) and other optical wavelengths can satisfy the second quadrant. In the third quadrant of the coordinate system, no natural materials meet these simultaneously negative requirements. This region is the metamaterial region that nature has not found for us. The last quadrant is for magnetic plasma, which does not naturally occur at optical wavelengths. The requirement for the inclusions to interact safely with light is much smaller than the incident wavelength. This is the main difference between simultaneously negative, which lies under the metamaterials and simultaneously positive, which lies on the photonic crystals. Also, the photonic crystals are periodic, and the period should be in the order of wavelength, while metamaterials do not necessarily need to be periodic.
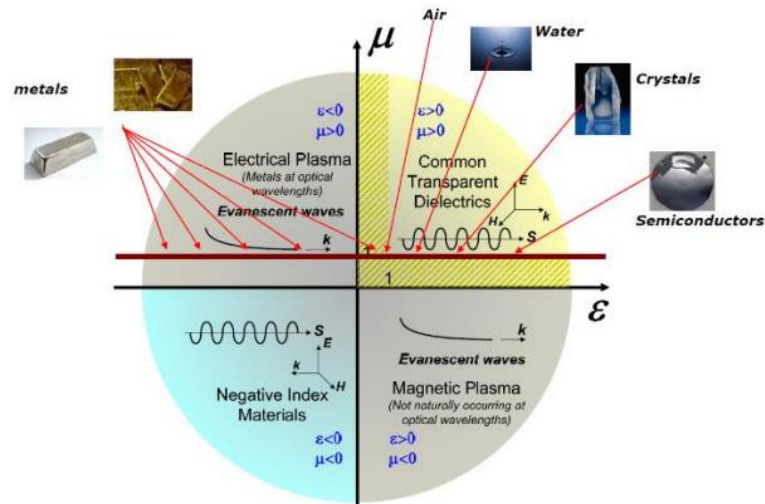
Figure 3.4: Indicate four materials based on the function of electrical permittivity (ε) and magnetic permeability (μ).

Furthermore, most natural materials have a double positive sign for the ε and μ. The plasmonic regime requires negative ε and positive μ, and this regime exhibits plasma behaviour. For example, silver and gold are epsilon-negative in the infrared and visible spectrums. The epsilon-negative or ENG has considerable attention in the optical dielectric function of metals and semiconductors (Johnson and Christy, 1972, Guo et al., 2017). ENG is needed in metamaterials for meta-performances such as negative refraction, negative phase velocity, or reverse Doppler effect (Shelby et al., 2001, Parazzoli et al., 2003, Veselago, 1968, Drachev et al., 2006, Grbic and Eleftheriades, 2002, Padilla et al., 2006, Iyer and Eleftheriades, 2002, Klar et al., 2006). For more details on epsilon negative ENG, refer to this reference (Fan et al., 2021) for an artificial magnetism regime where ε is positive and μ is negative. Materials with that kind of parameters provide a magneto-optic effect that modifies the electromagnetic waves by its quasi-static magnetic field. Also, single negative mu (μ) materials possessed some unique features not found in nature. In 1968, Victor Veselago, a Russian scientist, discovered materials with such properties (Veselago, 1968). However, electromagnetic waves decay evanescently in materials featuring either a single negative permeability or negative permittivity.

All materials can be classified and understood based on the electrical permittivity and magnetic permeability function. Most materials, such as water, glass, and other dielectric materials, lie on positive permittivity and permeability and are transparent to the incident electromagnetic waves. The electric and magnetic field and wave vector correspond to the right-handed rule; the propagation direction of the wave vector k and the Poynting vector P_t are in the same order

compared with a material possessing negative permittivity and permeability, which has an opposite k direction illustrated in Figure 3.5.

Right handed material
$$\varepsilon > 0 \; \mu > 0$$

Left handed material
$$\varepsilon < 0 \; \mu < 0$$
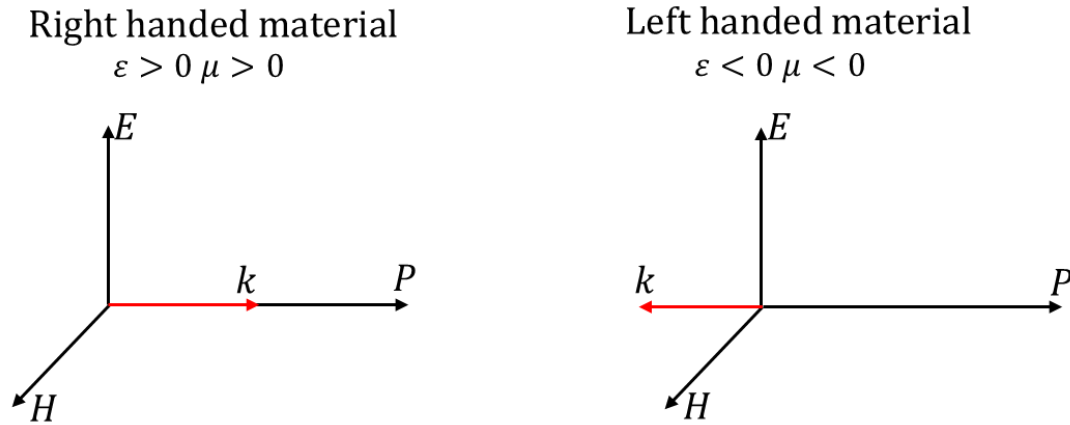
Figure 3.5: Field vectors, wave vectors and Poynting vectors in a right and left-handed material

The most superficial distinction between double positive materials (DPS) and double negative materials (DNG) is related to the refraction direction of the materials when the electromagnetic wave (light) passes through from the air. According to Snell's law, electromagnetic waves can be refracted toward or close to normal by cooperation:

$$n_a sin(\theta_a) = n_b \sin(\theta_b) \qquad 3.35$$

Equation 3.35 explains the relationship between the angles of incidence and refraction is equivalent to the ratio of phase velocities in the two media or the inverse proportion of n_a and n_b. Where n_a and n_b, are the indexes of the material, and $\theta_a \; and \; \theta_b$, are the angles of incidence and refraction. However, these processes are not only in the different direction of the refracted electromagnetic waves but also the frequency at which it is emitted (Bloembergen and Pershan, 1962), which requires phase matching to obtain efficient optical frequency conversion (Boyd, 2011, Lemieux et al., 2019, Sutherland, 2003, Bartal et al., 2006).

3.5.2   Negative Refractive index

The refractive index is the fundamental quantity used to characterise electromagnetic radiation's interaction with materials. As defined in equation 3.23, it is a complex number that has conventionally been regarded as positive. While the condition negative does not break any fundamental physical law, materials with a negative index have several unique and unexpected

features. For example, light, which is refracted at an interface between a positive-index material and a negative-index material, is bent in the way with respect to the normal. In this case, the group and phase velocities are antiparallel, the wave and Pointing vectors (**Pt** and **k**) are antiparallel, as illustrated in Figure 3.5. The concept of a negative refractive index (Antipov et al., 2005) refers to a unique phenomenon in which a material exhibits optical properties that deviate from those found in nature. Metamaterials are materials with a negative refractive index. They are man-made structures that use structures on the subwavelength scale to modify electromagnetic radiations (Farhat et al., 2010, Soukoulis et al., 2006). These materials are designed to interact with light in novel ways, allowing for a wide range of optical applications such as super-resolution imaging, cloaking devices, and enhanced sensing technologies (Smith et al., 2000). The phenomenon of negative refractive index challenges traditional optics by introducing new possibilities for controlling light and manipulating its behaviour, offering promising prospects for innovative applications in various scientific and technological fields (Kong, 2002).

Furthermore, the concept of a negative index of refraction, originally proposed by Veselago in the 1968, V. G. Veselago proposed the existence of substances with negative permittivity and permeability and elaborated the propagation rule for an electromagnetic wave in media (Veselago, 1968). In his pioneering work, Veselago presented the terminology of left-handed (LH) materials to refer to the left-handed pair formed by the electric field, magnetic field, and wave vector. Also, predicted LH materials possess several properties, including negative refraction for the interface scattering, inverse light pressure, reversed Doppler effect, and reversed ˇCerenkov radiation. In 1996, J. B. Pendry presented metallic structures made of thin metal wires to achieve negative permittivity in GHz bands (Pendry et al., 1996). The behaviours of that thin metal exhibit plasma characteristics under the action of electromagnetic waves and the frequency dependence of permittivity $\varepsilon\ (\omega)$.

However, the plasmonic concept involves creating artificial materials by combining metals and dielectrics to engineer a tailored response that differs from natural materials when subjected to an electromagnetic wave at their interface. The distinctions between artificial and natural materials in relation to their electromagnetic wave response can be explained in the table below.

Table 3.1**:** For artificial material and natural material.

	Metamaterials	**Natural materials**
Types of waves	Classical waves	Quantum/Classical waves
Constituents	Structured Metal/Dielectric	Atomic or Molecules
Geometric variants	Various shapes of constituents	Crystal lattice and amorphous state
Defect	Controllable	Random

3.5.2 Drude Model

One of the simplest models to describe the response of a metal particle revealed to an electromagnetic field was proposed by Paul Drude (Drude, 1902, Sommerfeld, 1928) at the beginning of the 20th century and additionally extended by Hendrik Lorentz five years later, for a detailed discussion. In 1933, Arnold Sommerfeld and Hans Bethe expanded the classical Lorentz-Drude model and eliminated some problems in the explanation of thermal electrons by accounting for the Pauli principle of quantum mechanics and replacing the Maxwell-Boltzmann with the Fermi Dirac distribution (Gordon, 2002, Fazarinc, 2015), Drude assumed a microscopic description of the electron sea in metal in classical relations, obtained the equation of motion of a damped oscillator where the electrons of the plasma sea, with charge $-e$ and effective mass m and the wave characterised by the complex electric field along the x direction of $\boldsymbol{E}(r,t) = \boldsymbol{E}(t)e_x$. The electron position $er(t)$ satisfies the laws of classical mechanics and defined as:

$$m\frac{d^2 er}{dt^2} + m\gamma\frac{der}{dt} = -e\boldsymbol{E} \qquad 3.36$$

For the harmonic time dependence of the driving field $E(t)$ can be described as $E_0 \exp j\omega t$, and the oscillation of the electron position can be described as $er(t) = er_0 \exp -j\omega t$. Therefore:

$$er_0 = \frac{-eE/m}{(\omega_0^2 - \omega^2) \pm j\gamma\omega}\boldsymbol{E} \qquad 3.37$$

Then, the polarisation vector, $\boldsymbol{P}$ described as $\boldsymbol{P} = -eNx$, where N is the number of electrons oscillating per unit volume. By using the expression for $\boldsymbol{P}$ in equation 3.37, we can generate the polarisation component become:

$$\boldsymbol{P} = \varepsilon_0 \left(\frac{Ne^2/\varepsilon_0 m}{(\omega_0^2 - \omega^2 \pm j\gamma\omega)} \right) \boldsymbol{E} = \varepsilon_o \chi_e(\omega) \boldsymbol{E} \qquad 3.38$$

Where $\chi_e(\omega)$:

$$\chi_e(\omega) = \frac{Ne^2/\varepsilon_0 m}{\omega_0^2 - \omega^2 \pm j\gamma\omega} \qquad 3.39$$

Since we started the behaviours of the thin metal introduced plasma characteristics, the dielectric function of a thin metal can be described as:

$$\varepsilon(\omega) = 1 - \frac{Ne^2/\varepsilon_0}{m(\omega_0^2 - \omega^2 \pm j\gamma\omega)} \qquad 3.40$$

Which can be re-written in the well-known format of Drude expression as:

$$\varepsilon(\omega) = 1 - \frac{\omega_p^2}{\omega_0^2 - \omega^2 \pm j\gamma\omega} \qquad 3.41$$

Where ω_p, is the plasma frequency, and γ is the damping factor. The plasma frequency is considered as follows:

$$\omega_p^2 = \frac{\text{effective electron } (Ne_{\text{eff}}^2)}{\text{effective mass } (\varepsilon_o m_{\text{eff}})} \qquad 3.42$$

Where the Ne_{eff}, described $n\pi r^2/a^2$ and m_{eff} described as $\mu_o e^2 n/2\pi \ \text{In}(a/r)$ if we consider this reference by (Pendry et al., 1996). Furthermore, the real and imaginary components of the complex dielectric function can be as follows:

$$\varepsilon_{\text{real}}(\omega) = 1 - \frac{\omega_p^2 \tau^2}{1 + \omega^2 \tau^2} \qquad 3.43$$

$$\varepsilon_{\text{imaginary}}(\omega) = \frac{\omega_p^2 \tau}{\omega(1 + \omega^2 \tau^2)} \qquad 3.44$$

Most metals lie in the ultraviolet region, which is why they are shiny and glittering in the visible spectrum. These conditions came under when the eigenfrequency was more significant than the plasma frequency $(\omega > \omega_p)$, then the dielectric function becomes positive, and the imaginary part (ε'') vanishes, leading to negligible damping. The metal becomes transparent because the electrons in the metal are too slow and cannot respond fast enough. While when the eigenfrequency was less significant than the plasma frequency $(\omega < \omega_p)$, the dielectric

function becomes negative, and the light is reflected corresponding to refractive index n imaginary.
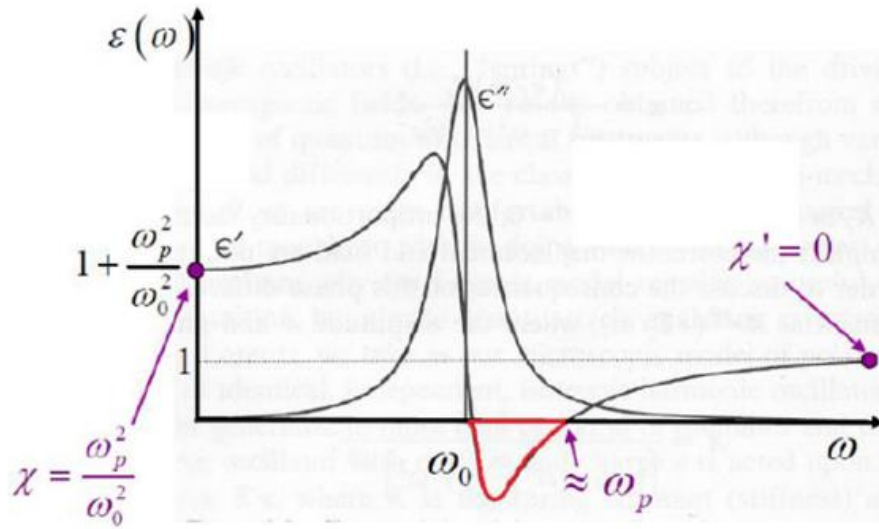
Figure 3.6: The complex dielectric function of frequency ω. The region with the negative real part of permittivity over resonance is bold by red mark (Shalaev, 2008).

3.6 Thermal emission Benefits

Thermal emission control has attracted increased attention in fundamental science and many applications, including infrared sensing, radiative cooling and thermophotovoltaics. Infrared absorbers with narrowband absorption properties have considerable application in thermal imaging. The infrared absorber, like an ideal blackbody, absorbs all the incidence radiation. Therefore, materials with high infrared absorption properties are much more significant in many fields and can be applied in photodetectors (Ahn et al., 2005, Gu et al., 2005, Hayden et al., 2006). Based on this premise, we introduce designing plasmonic metamaterial structures (PMMs) to serve as perfect absorbers in the mid-infrared range. The primary objective is to absorb heat and emit it as a coherent thermal light source. Another prospective application involves enhancing the energy conversion efficiency of electrical power, such as in thermoelectric generators or thermophotovoltaic systems, as indicated in reference Figure 3.8.

For more than a century, scientists have been fascinated and confounded by the physics of the blackbody (Planck, 1901). In practice, most objects have finite absorption and are called graybody. The emission spectra of graybodies can be altered by manipulating system geometry or utilising different materials. This capability to modify thermal emission profiles is key in various fields of applied physics and engineering. The desire to convert broadband thermal

emission to narrowband is necessary, especially in thermophotovoltaic, to reduce the cost-effectiveness of conversion filters. The conversion aims to optimize energy conversion efficiency by matching the emission spectrum to the spectral response of photovoltaic cells, potentially enhancing cost-effectiveness and overall performance. Figure 3.7 (a) demonstrates the thermoelectric conversion process involves the transformation of a heat flux, which typically flows from a hot source T_{hot} to T_{cold} into electricity via the Seebeck effect. The Seebeck effect is a fundamental principle of thermoelectricity where a voltage is generated across a material when there is a temperature gradient along its length. Figure 3.7 (b) illustrates the direct conversion of thermal radiation due to the thermophotovoltaic effect, generation, and subsequent separation of charge carriers with a p-n junction. The fundamental distinction in a thermophotovoltaic system lies in its optimised design to capture thermal radiation and convert it into electricity, using a photovoltaic device with tailored properties for efficient conversion at lower-energy photons.
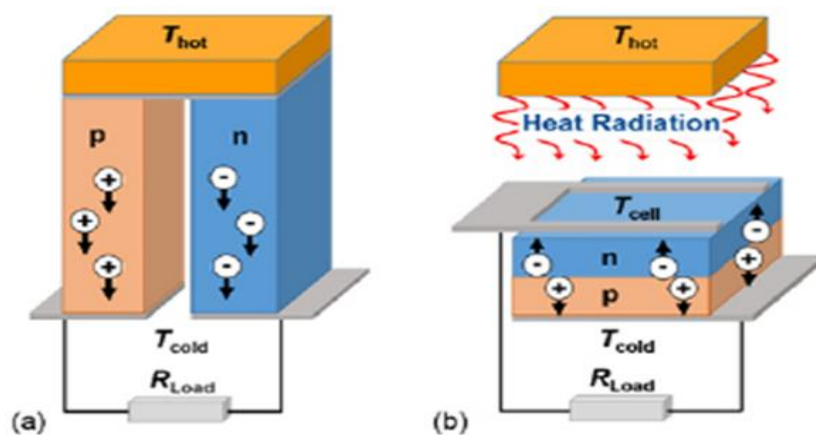
Figure 3.7: Depicts two alternatives for directly converting heat fluxes into electricity: (a) thermoelectric conversion. (b) Thermophotovoltaic effect, generation,(Tedah et al., 2019).

Our strategy here, is to follow Planck's thermal emission concept to improve heat recovery performance. The idea is based on a blackbody emitting a wide range of electromagnetic radiation depending on its temperature, and the intensity of light emitted by a blackbody increases as its temperature rises. The fundamental property of this concept is that the optical absorptivity of the object determines its thermal emissivity, thanks to Kirchhoff's law, which quantifies the tendency of that object to generate thermal emission when compared to a blackbody. The relationship between absorption and thermal emission, which is related to the time reversibility of microscopic processes, suggests that thermal emission temporal and spatial

coherence can be engineered through material selection and patterning. Therefore, we provided a modelling step in Figure 3.8 via the simple analysis to understand the transition between graybody and blackbody at the same temperature.
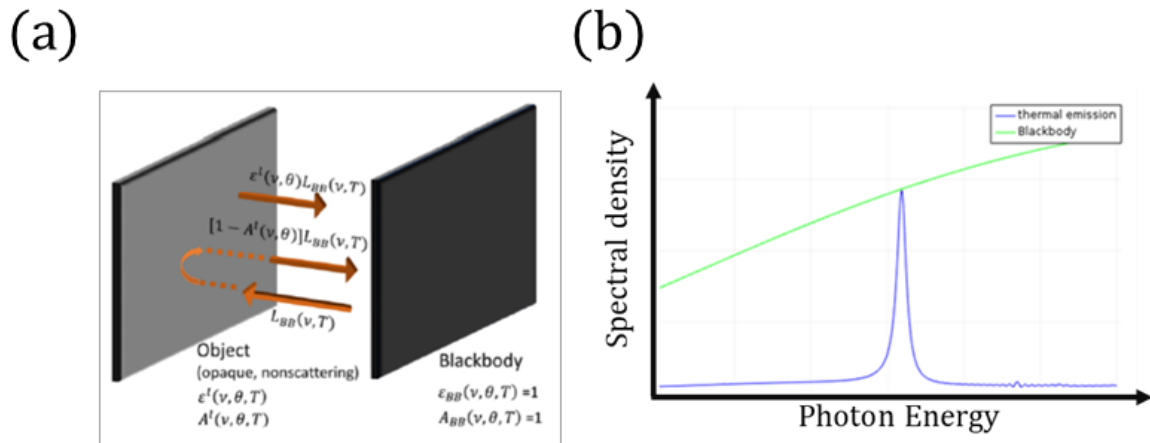
Figure 3.8: (a) Schematic of the energy balance described by Kirchhoff's law. (b) comparison spectrum between the graybody of the nanostructure and the blackbody at the same temperature.

3.6.1   Gratings Emitters

Grating is a different arrangement of different materials or structures on specific surfaces, usually periodically, resulting in refractive index variation. Etching or depositing causes changes in the refractive index, and diffraction occurs when the period of the index variant is more significant than the wavelength of light inside the grating material. Otherwise, light propagation in a grating will exhibit similar characteristics to that of a uniform medium and become more significant as the grating period decreases. The grating structure created artificial emitters such as spatial and temporally coherent light. The theoretical works were conducted in the 1980s and 1990s. Hesketh presented innovative experimental work examining the thermal emission from 1D deep gratings and demonstrated that these deep gratings exhibit significantly higher spectral emissivity than the pure, smooth surface. Many reporters have displayed 1D, 2D and 3D grating to manipulate thermal radiation (Greffet et al., 2002b, Gong et al., 2013b) (Heinzel et al., 2000) (Arnold et al., 2012, Kohiyama et al., 2015) to achieve narrowband (Kohiyama et al., 2015, Gong et al., 2013a) or wavelength-selective emitters(Sai et al., 2005). The theoretical calculations of the grating consider the following:

$$\boldsymbol{k} = \ \boldsymbol{k}_x \ + p\beta_g \qquad\qquad 3.45$$

Where p is an integer denoting the diffraction order, $k_x = 2\pi sin\theta/\lambda$, is the x- component of the wavevector of emitted waves, $\beta_g = 2\pi/\Lambda$ is the grating reciprocal vector, and k is the wavevector of the surface wave.

$$k = k_o \left(\frac{\varepsilon_a \varepsilon_b}{\varepsilon_a \varepsilon_b}\right)^{1/2} \qquad 3.46$$

where ε_a and ε_b, are permittivities of the surrounding medium. Similarly, quasi-coherent thermal radiation sources can be generated by combining the simple grating structure and the resonance wavelength of microcavity modes, which can be theoretically estimated as:

$$k = \sqrt{\left(\frac{\pi p}{a}\right)^2 + \left(\frac{\pi l}{h}\right)^2} \qquad 3.47$$

where p and l are integers indicating the orders of cavity resonance, and a is the metal film grating absorber, which is attributed to a combined anti-reflection effect at the top grating interface and efficient light coupling to densely populated localized modes in both angular and spectral domains, $k = 2\pi/\lambda$, is the wavevector, and h is the grating depth.

3.6.2   Photonic Crystals Emitters

Thermal emitters related to photonic crystals had the ability to achieve narrowband emission, directional, polarised, and even tunable emission. The photonic band gaps (PBG) generated by the destructive interference of scattered waves from different lattice points (Joannopoulos et al., 2008) can be engineered by the arrangements and periodicity, which can serve as an effective tool to tailor thermal emission. In general, photonic crystals are good candidates for designing ultracompact devices suitable for integrated photonic circuits. The behaviour's structure is regular arrays of dielectric layers with periodic refractive index, making them efficient in confining light waves in very small spaces. The essential characteristic of photonic crystals is a wavelength region in their band structure where no electromagnetic wave can propagate, and this region is known as the photonic band gap (PBG). Some feature-designed optical devices based on photonic crystals are Optical filters (Alipour-Banaei and Mehdizadeh, 2012, Alipour-Banaei and Mehdizadeh, 2013, Alipour-Banaei et al., 2013, Robinson and Nakkeeran, 2012), optical reflectors (Mehdizadeh et al., 2012), power splitters (Bayindir et al., 2000), optical switches (Cuesta-Soto et al., 2004), and optical demultiplexers(Bazargani, 2012, Rostami et al., 2011).

According to the dimensions based on nanostructures, the photonic crystal emitters can be divided into three: one-dimensional (1D), two-dimensional (2D) and three-dimensional (3D) photonic crystal thermal emitters. In a 1D photonic crystal, the emitters can still offer dependable control of thermal emission with an easy fabrication process, as many researchers reported (Narayanaswamy and Chen, 2004, Lee et al., 2005). Regarding 2D grating photonic crystals, consisting of periodic cavities or holes arranged on the wavelength scale, theoretical mechanisms of the designing rule can be applied, such as the excitation of surface waves using diffraction and cavity resonance modes. According to this source (Pralle et al., 2002), these emitters are photonic crystal-enhanced narrowband infrared emitters. Thermal emitters constructed by 2D-photonic crystals were reported in these references (Sai et al., 2001, Enoch et al., 2005), (Laroche et al., 2006). Thermal emitters based on three-dimensional photonic crystals (3D-PCs) can also be used to manipulate photonic band structures comprehensively. The emitters of 3D PCs have received extensive study due to the band gap, which effectively suppresses light propagation in all directions near the emission bands. Many successful 3D-PCs thermal emitters have been achieved (Lin et al., 2003a), (Han et al., 2007), (Arpin et al., 2013).

3.6.3   Metasurfaces Emitters

Usually, metasurface can be considered a new branch of metamaterials in two dimensions. Generally, periodic or nonperiodic arrangements of planar and subwavelength meta-atoms, which may or may not be resonant, are used to create metasurfaces. Engineering an individual resonant meta-atom, including its shape, size, composite material, and spatial and orientational arrangements, can artificially tailor the electromagnetic response of the entire configuration. In nanophotonics, metasurfaces have multiplied interest over the past few years. They offer extraordinary opportunities for manipulating electromagnetic wave amplitude, phase, and polarisation, and they support novel applications in imaging, sensing, information processing, energy harvesting, and conversion.

Structures like Metal-Insulator-Metal (MIM), in which absorption resonance can be controlled by combining various MIM resonators of different dimensions within the same subwavelength period (Bouchon et al., 2012, Koechlin et al., 2013), are also called metasurfaces. Metasurfaces are successfully used to design thermal emitters with extraordinary abilities, such as directionality, monochromaticity, and tunability. The achievement of metasurface can be presented by (Makhsiyan et al., 2015), (Miyazaki et al., 2014), (Cao et al., 2021), (Ji et al.,

2014), (Costantini et al., 2015a), etc. Metasurface designing can allow the achievement of thermal emitters at different wavelengths and emit radiations at different polarisations.

3.6.4 Metamaterials Emitters

The emitters based on micro/nanostructure typically use this kind of artificial materials to exhibit exotic properties like negative refraction (Yao et al., 2008), optical cloaking (Cai et al., 2007), and spontaneous emission enhancement (Lu et al., 2014), which provide unprecedented possibilities for photonics engineers to tailor thermal radiation. The metamaterials formation operation does not depend on photonic band gaps, although certain locally resonant metamaterials also display photonic band gaps due to strong coupling (Lemoult et al., 2013, Sugino et al., 2016).

Metamaterial thermal emitters achieve a broad and narrowband emission spectrum, which has been the subject of many articles focusing on selective or nonselective thermal emitters. Many researchers have reported a narrowband infrared thermal emitter based on a metamaterial. Plasmonic metamaterials have also been investigated for solar TPV applications (Deng et al., 2014). Developing a novel, highly efficient, and cost-effective mid-infrared light source has been identified as a scientific key and technological aim (Gong et al., 2017), (Matsuno and Sakurai, 2017). The metamaterial emitter based on a hyperbolic metamaterial (HMM) structure has been reported; the methodology is based on engineering the poles and zeros of the dielectric constant, which permits a variety of distinct optical responses. Many categories of metamaterial emitters have been reported to support the formation of the traditional application (Molesky et al., 2013), (Datas and Algora, 2010), (Dyachenko et al., 2016), (Kan et al., 2017), (Campione et al., 2016). It is possible to achieve highly directional strong emissivity and even super-Planckian emission in specific directions using asymmetric hyperbolic metamaterials (Nefedov and Melnikov, 2014), which exceeds the predicted Planck's limit by more than two orders of magnitude in the enhanced direction. To improve directionality, the optical axis of the uniaxial hyperbolic metamaterial is tilted to introduce asymmetry. Recently, metamaterial emitters have been demonstrated based on nonperiodic or even random micro and nanostructures, which are relatively easier to fabricate on a large scale. This type of metamaterial usually depends on the resonances in a single composition unit because the inter-unit coupling effect is difficult to control. For example, the proposed scalable disordered hybrid metamaterial based on a polymeric thin film embedded with arbitrarily distributed SiO_2 microspheres, which can act as radiative cooling emitters, exhibited an infrared emissivity greater than 93% across the

atmospheric window (Zhai et al., 2017). Therefore, the high performance of the emissivity is attributed to the localised phonon polaritons supported by the SiO_2 microspheres. The proposed Mie-resonance-based metamaterial thermal emitter for thermophotovoltaic applications consists of a thin film of SiO_2 embedded with nanoparticles on top of a tungsten layer (Ghanekar et al., 2016). The high emission broadband was achieved in the wavelength range of 0.4 μm to 2 μm, and it is suitable for GaSb and InGaAs-based photovoltaic cells.

Another remarkable report using Mie resonances to enhance thermal emission (Asano et al., 2016) combined the interband transitions and the Mie resonances in Si nanorods to realize a high thermal emission in the near-to-visible infrared range. Mie resonances are a class of electromagnetic resonants that appear when light interacts with spherical particles, which are frequently metallic or dielectric and have a diameter equal to the wavelength of the incident light. These resonances are named after the German physicist Gustav Mie, who extensively studied light scattering by spherical particles in the early 20th century. It is expected that the disordered array can also exhibit comparably high emissions because the performance mainly depends on the optical response of individual nanorods rather than their spatial arrangements. Micro- and nanoporous materials can also be treated as disordered metamaterial emitters. (Kong et al., 2018) introduced a random metamaterial thermal emitter based on three-layer structures, which consist of an insulator (SiO_2) layer sandwiched between a continuous metallic (W) film and an arbitrarily perforated metallic film. The electromagnetic radiation emitter is focused around 1μm due to the near-perfect impedance matching.

3.7   Tunable Plasmon Resonances

Surface plasmon resonance control can be achieved by inducing changes in the plasmonic materials' carrier density and dielectric function. Based on that, plasmonic structures can be designed and explained without the support of tunable surrounding media or supporting substrates. As a result, the modulation performance of such tunable plasmonic systems is determined by variations in the carrier density and dielectric function of the constituent materials. Tunable plasmon resonances depend on the intended application, and plasmon resonances can be turned in many ways. The excitation mechanisms for various plasmon resonances differ, which causes the resonance wavelength to depend on different parameters, namely the size and shape of nanoparticles and the dielectric constant of the environment.

Localised surface plasmon resonances (LSPRs) are highly tunable, allowing light to be confined to deep sub-wavelength dimensions. Most plasmon resonances exhibited a strong confirmation as the nanoparticle's size increased. The shape of nanoparticles is a significant design parameter that enables the excitation from plasmonic modes (plasmon resonances) to be highly sensitive to the metals and the surrounding dielectric mediums. LSPR can be tuned from ultraviolet to near-infrared by modifying the nanoparticle size and shape. The effect that appears due to the nanoparticle (Rivera et al., 2012) size is essential to understanding that there are two different size effects in this particular size regime, intrinsic and extrinsic. The intrinsic size effect, known as the quantum size effect, occurs in tiny sizes, less than 5 nm, where the energy level becomes discrete, and electrons have a high possibility of transferring between these levels. Due to this effect of electron transfer between energy levels, classical theory cannot be used, and quantum theory is necessary (Rivera et al., 2012, Kreibig and Vollmer, 2013). As particle size increases, the spacing between energy levels decreases, and a continuous band is formed, called the extrinsic size effect.

3.8 Wave Polarisation

Polarisation and its properties are typically used on transverse waves to determine the geometrical orientation of the oscillations. Polarisation is a significant feature of light that controls even optical systems that do not measure it explicitly, and it is essential for many optical applications. Optical design frequently focuses on light wavelength and intensity while ignoring polarisation. Light polarisation affects the focus of light beams and the cut-off wavelengths of filters and can help prevent unwanted back reflections. Different polarisations of light can also be absorbed to different degrees by materials. We classify wave polarisation into linear, Circular, and Elliptical polarisation. We considered $\boldsymbol{E}_x$ and $\boldsymbol{E}_y$, as a polarisation vector for transverse plane waves which are polarised perpendicular to each other. The wavevector $\boldsymbol{k}$ and angular frequency ω are real and, in the vacuum, are related by $\omega = c\boldsymbol{k}$. This relation indicates that electromagnetic waves are dispersion less with velocity (c), and in materials like a prism, light can have dispersion. Therefore, the equation suggests the electric field completely defines the magnetic field in a plane wave.

$$\boldsymbol{B_0} = {}^{1}\!/_{\omega}\,(\boldsymbol{k} \times \boldsymbol{E_0}) \qquad\qquad 3.48$$

Their magnitudes relation is:

$$|\boldsymbol{E}_0| = c|\boldsymbol{B}_0| \qquad\qquad 3.49$$

Then, the electric field that moves in the $z-$direction at the speed of light can be described as:

$$\boldsymbol{E} = \boldsymbol{E}_0 e^{j\omega\left(\frac{z}{c}-t\right)} \qquad\qquad 3.50$$

However, since the $\boldsymbol{E}_o$, is orthogonal to $\boldsymbol{k}$, and the linear polarised without phase difference can be written as $\boldsymbol{E}_0 = (\boldsymbol{E}_x, \boldsymbol{E}_y, 0)$ also, these two polarisation vectors $\boldsymbol{E}_x$, and $\boldsymbol{E}_y$ has magnitudes and phases as $\boldsymbol{E}_x = |E_x| \exp j\emptyset_x$ and $\boldsymbol{E}_y = |E_y| \exp j\emptyset_y$. Therefore, in the case of linear polarisation, the electric field is confined to a plane along the direction of propagation, $\boldsymbol{E}_x$ and $\boldsymbol{E}_y$ with the dielectric constant ε_x and ε_y, as shown in equation 3.51.

$$\begin{cases} \boldsymbol{E} = \varepsilon\boldsymbol{E}_{,0}x \exp j(\boldsymbol{k}z - \omega t) \\ \boldsymbol{E} = \varepsilon\boldsymbol{E}_0 y \exp j(\boldsymbol{k}z - \omega t) \end{cases} \qquad\qquad 3.51$$

Also, magnetic field:

$$\begin{cases} \boldsymbol{B} = -\frac{1}{\omega}\boldsymbol{E}_0 x \exp j(\boldsymbol{k}z - \omega t) \\ \boldsymbol{B} = \frac{1}{\omega}\boldsymbol{E}_0 y \exp j(\boldsymbol{k}z - \omega t) \end{cases} \qquad\qquad 3.52$$

Combination of these plane waves (3.51) with electric field direction (polarisation) ε_x and ε_y and complex electric field amplitude $E_0 x$ and $E_0 y$ the polarisation of the wave in the most general homogeneous plane wave can be described as

$$\boldsymbol{E} = (\varepsilon\boldsymbol{E}_{0,}x + \varepsilon\boldsymbol{E}_{0,}y)\exp j(\boldsymbol{k}z - \omega t) \qquad\qquad 3.53$$

The real and complex parts of the electric field amplitudes determine the polarisation state of the integrated EM wave, which is determined by the magnitude and phase of the field amplitudes of the constituent waves. For simplicity, both waves are in phase, and their combination is homogeneous, as illustrated in Figure 3.9.
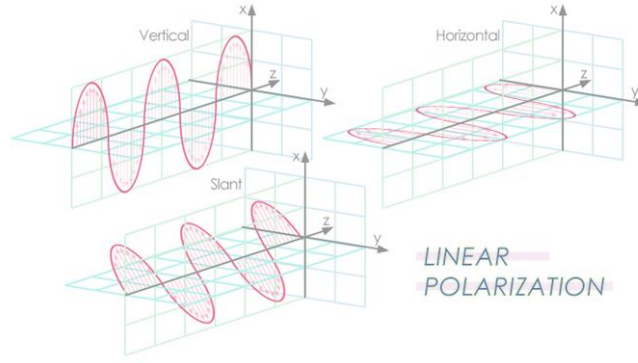
Figure 3.9: Schematic representation of a linearly polarised wave. The electric field of linearly polarised light is confined to the x-z plane (vertical wave) and the y-z plane (horizontal wave) along the direction of propagation. The slant linear polarised refers to oscillates of an electrical field at a 45-degree angle to a reference plane (https://jemengineering.com/blog-intro-to-antenna-polarisation/)

In circular polarisation, in this case, the electric field comprises two linear components perpendicular to each other, equal in amplitude but differ by a phase difference (out of phase) of $\pi/2$. The resultant electric field spins in the circle around the propagation direction, as demonstrated in Figure 3.10, and is referred to as left- or right-hand circularly polarised light, depending on the rotating direction. Therefore, $\pi/2$ can be described as $\emptyset_x - \emptyset_y$. Then,

$$\boldsymbol{E} = \boldsymbol{E}_0(\varepsilon_x \pm j\varepsilon_y) \exp j(\boldsymbol{k}z - \omega t) \qquad 3.54$$

Considering the direction of the unit vectors ε_x and ε_y. The propagation direction on the z-axis and the components of the electric fields can be obtained by taking the real part of the actual electric field.

$$Re[\boldsymbol{E}] = (\boldsymbol{E}_0 cos(\boldsymbol{k}z - \omega t), \quad \pm\boldsymbol{E}_0 sin(\boldsymbol{k}z - \omega t)) \qquad 3.55$$

When the upper signs in equations 3.54 and 3.55 are considered. These equations describe that at a fixed point in space, the electric field magnitude is constant at any instant and rotates around the propagation direction. The two circular polarisation states can also be used as primary fields to describe any other polarisation state.
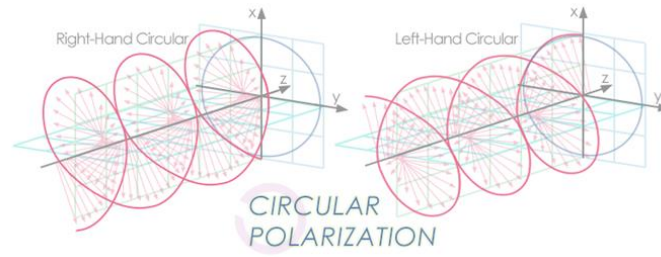
Figure 3.10: Schematic representation of a circularly polarised wave. The circularly polarised light electric field consists of two perpendiculars, equal-amplitude linear elements with a phase difference of π/2 or 90°. The resulting electric field wave flows in a circular motion. This polarisation consists of right and lifts hand rotation, as illustrated in the figure. (https://jemengineering.com/blog-intro-to-antenna-polarisation/)

Consequently, circular and linear polarisations are not linearly independent. Indeed, any potential polarisation can be written as a linear combination of left and right-handed. The distinction between linear and circular polarisation is angular momentum. Linearly polarised light carries no angular momentum. From this point of view, light cannot have arbitrarily small intensity. The smallest intensity light can obtain a single photon, and the photon itself must be polarised. A single circularly polarised photon has angular momentum:

$$\mathbf{J} = \pm \frac{h}{2\pi} \mathbf{k}$$

3.56

Elliptical polarisation: An ellipse is defined by the electric field of light induced by two linear components of varying amplitudes or a phase difference greater than $\pi/4$. Circular and linear polarised light may be considered special elliptically polarised light cases.
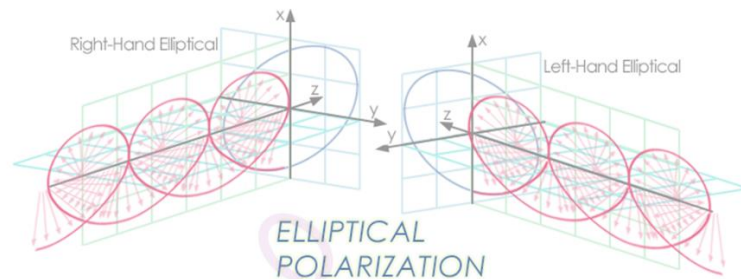
Figure 3.11: Schematic representation of an elliptically polarised wave composed of two transverse electromagnetic plane waves which are out of phase by π/4. Elliptical polarisation refers to an electrical field propagated in an elliptical helix. Like circular polarisation, this polarised can either be right-hand or left-hand, as illustrated in the figure. (https://jemengineering.com/blog-intro-to-antenna-polarisation/)

Numerous sources of electromagnetic radiation, such as the sun, fires, and incandescent lights, emit short waves that comprise an equal combination of polarisations, referred to as unpolarised light. Polarised light is created by passing unpolarised light through a polarizer, allowing only one polarisation of light to pass through. Most optical materials do not inherently

affect light polarisation, but certain materials exhibit properties like birefringence, dichroism, or optical activity, which influence light in different ways based on its polarisation. Some of these materials are utilised in the production of polarizing filters. When light reflects at an angle from a surface, it becomes partially polarised due to the orientation of the reflected waves.

3.9   Plasmonic Metamaterial Field Interest

The class of artificially structured materials (Plasmonic metamaterials) is a promising candidate for manipulating thermal emission properties that are difficult to achieve in natural materials. To date, different types of narrowband based on metamaterials emitters/absorbers have been reported, such as nano-gratings (Ikeda et al., 2008, Qu et al., 2016b, Bonod et al., 2008, Sai et al., 2003) photonic crystals (Lin et al., 2003b, Rinnerbauer et al., 2014, Fleming et al., 2002), thin films (Landy et al., 2008b), and three-layer-metamaterials (Liu et al., 2011b, Cui et al., 2014, Shrekenhamer et al., 2013, Liu et al., 2010a). Unfortunately, this strategy suffers from a common disadvantage of poor spatial coherence and relatively sizeable spectral bandwidth, which limits the device performance and real-world applications such as ultrahigh-resolution optical sensing (Lochbaum et al., 2020, Lochbaum et al., 2017a). This thesis reported the structures based on Plasmonic metamaterials (PMMs). The design allows thermal emitters with an ultranarrow spectrum and antenna-like spatial directivity. Additionally, the operating wavelength, radiation polarisation and angle are highly flexible and can be effectively tuned by varying the structure bandgap and geometry of the metallic surface pattern. These features open possibilities to obtain a novel compact mid-infrared source scheme that could have great potential for applications such as thermal analysis, imaging, security, biosensing, and medical diagnoses.

3.10   Conclusion

This chapter established the theoretical framework for the proposed title. Its key objective was to enhance comprehension of the waveguide (plasmon) behaviour at the interface between metal and dielectric materials. To facilitate understanding, the Maxwell's equations in microscopy were employed to elucidate behaviour leading to electric and magnetic phenomena. The discussion covered various aspects, including bulk plasmons representing collective electron oscillations within three-dimensional structures and surface plasmons occurring at the interface between conductive and dielectric materials. Furthermore, the surface dispersion theorem was examined to define the relationship among frequency, wavevector, and

other material parameters. Exploration into waveguide excitation covered scenarios engaging both long and short propagation distances. Metamaterial arrangements for manipulating the electric and magnetic response to incident waves were also discussed. The classification of material properties' function based on electric permittivity (ε) and magnetic permeability (μ), and tunable plasmonic resonance were examined in chapter, including the potential technological benefits of thermal emission.

Chapter 4
Research Methodology

This Chapter demonstrates a simulation algorithm for nanophotonics design. Computational modelling approaches based on electromagnetic theory are introduced as a critical method for fabricating plasmonic metamaterial structures. We also concentrate on some of the fundamental phenomena that give rise to many of the features observed in emission spectra of 3D, 2D, and 1D-periodic arrangement of plasmonic metamaterials (PMMs) to develop physical intuition and understanding of features behind thermal emission spectrum.

4.1 Lumerical Methods and Analysis

We conducted 3D simulations for the PSG and PIRA design nanostructures using finite-difference time-domain (FDTD), which allowed us to determine optical absorption across the complex metallic pattern. FDTD, a commercial time-domain finite element solver for Maxwell's equations, was used for time-domain simulations. Inside the field, the sample is defined in 2D or 3D, and the optical properties of the materials are determined using frequency-dependent parameters. Use of rectangular mesh, the structure is divided into discrete cells for which Maxwell's equations are solved in the time domain. The structure is exposed to a pulse with the desired frequencies, and its electromagnetic response is calculated as a function of time. Analysis of time-dependent solutions by Fourier produces electromagnetic fields at a specific frequency.

According to, the curl equation of Maxwell's equation related to equations 3.10 and 3.11 can be extended in differential form by

$$\frac{\partial \boldsymbol{E}}{\partial t} = -\frac{1}{\varepsilon} \nabla \times \boldsymbol{H} - \frac{\sigma}{\varepsilon} \boldsymbol{E} \qquad\qquad 4.1$$

$$\frac{\partial \boldsymbol{H}}{\partial t} = -\frac{1}{\mu} \nabla \times \boldsymbol{E} - \frac{\rho}{\mu} \boldsymbol{H} \qquad\qquad 4.2$$

The $\boldsymbol{E}$ and $\boldsymbol{H}$ in the Cartesian coordinate system have three corresponding components in three coordinate directions, respectively. Therefore, the equation is rearranged (Taflove et al., 2005).

E-field:

$$\frac{\partial E_z}{\partial t} = \frac{1}{\varepsilon}\left(\frac{\partial H_y}{\partial x} - \frac{\partial H_x}{\partial y} - \sigma E_z\right) \qquad 4.3$$

$$\frac{\partial E_x}{\partial t} = \frac{1}{\varepsilon}\left(\frac{\partial H_z}{\partial y} - \frac{\partial H_y}{\partial z} - \sigma E_x\right) \qquad 4.4$$

$$\frac{\partial E_y}{\partial t} = \frac{1}{\varepsilon}\left(\frac{\partial H_x}{\partial z} - \frac{\partial H_z}{\partial x} - \sigma E_y\right) \qquad 4.5$$

H-field:

$$\frac{\partial H_z}{\partial t} = \frac{1}{\mu}\left(\frac{\partial E_y}{\partial x} - \frac{\partial E_x}{\partial y} - \rho H_z\right) \qquad 4.6$$

$$\frac{\partial H_x}{\partial t} = \frac{1}{\mu}\left(\frac{\partial E_z}{\partial y} - \frac{\partial E_y}{\partial z} - \rho H_x\right) \qquad 4.7$$

$$\frac{\partial H_y}{\partial t} = \frac{1}{\mu}\left(\frac{\partial E_x}{\partial z} - \frac{\partial E_z}{\partial x} - \rho H_y\right) \qquad 4.8$$

E and H-field can be represented by a function relating to time and position $f(x, y, z, t)$, its discrete in time and the spatial domain is given by,

$$f(x, y, z, t) = f(i\Delta x, j\Delta y, k\Delta z, n\Delta t) = f^n(i, j, k) \qquad 4.9$$

The following equations are obtained by taking the partial derivative of $f(x, y, z, t)$ with respect to time and the spatial components, respectively.

$$\left|\frac{\partial f(x,y,z,t)}{\partial x,y,z,t}\right|_{\substack{x=i\Delta x \\ y=j\Delta y \\ y=k\Delta z \\ y=n\Delta t}} \approx \begin{cases} \dfrac{f^n\left(i+\frac{1}{2},j,k\right)-f^n\left(i-\frac{1}{2},j,k\right)}{\Delta x} \\[2ex] \dfrac{f^n\left(i,j+\frac{1}{2},k\right)-f^n\left(i,j-\frac{1}{2},k\right)}{\Delta y} \\[2ex] \dfrac{f^n\left(i,j,k+\frac{1}{2}\right)-f^n\left(i,j,k-\frac{1}{2}\right)}{\Delta z} \\[2ex] \dfrac{f^{n+\frac{1}{2}}(i,j,k)-f^{n-\frac{1}{2}}(i,j,k)}{\Delta t} \end{cases} \qquad 4.10$$

The Yee lattice, shown in Figure 4.1, depicts the spatial distribution of spatial nods of discrete electric and magnetic fields and is the robust core scheme of the FDTD method. Electric and magnetic field components surrounded each other inside the Yee cell. These fields' (E and H) direction arrangement obeys Faraday's law of electromagnetic induction and Ampère's circuital law, making it suitable for computing the difference of Maxwell's equation.
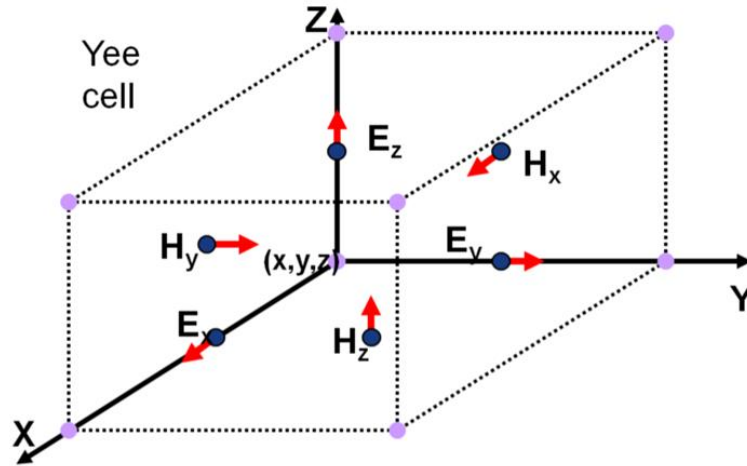
Figure 4.1: The Yee lattice of FDTD methods (Yee, 1966).

Maxwell's equation is solved by the FDTD method using the approximation in equation 4.10. Errors are, therefore, unavoidable at each step of the computing process. With increasing iterative steps and simulation duration, the error will accumulate to a value that must be considered. The simulation is considered stable or convergent if the accumulated error from each step does not increase the total error. In contrast, the simulation is unstable, which manifests itself as an infinite increase in simulation results with an infinite increase in simulation time and step. The numerical analysis of FDTD's stability is based on the Courant method. The stability condition of FDTD methods is characterised by time and spatial steps $(\Delta t \leq \Delta l / c\sqrt{N})$ and is the dimension of space for the simulation. The simulation must be finite due to computer memory constraints. The boundary region of the simulation requires special treatment. In general, the boundary should region's maintain outer radiation from the wave. Therefore, there should be no reflection at the simulation boundary and no distortion in the internal spatial space. The FDTD simulation's boundary is the perfect match layer (PML) based on Maxwell's equations (Berenger, 1994). The PML is a layer of a medium with a wave impedance that matches its neighbouring medium. The incident wave passes through the PML interface without reflection. A high-absorbing, finite layer thickness of PML can attenuate and absorb the incident wave. For FDTD simulation, the PML is the most commonly used for absorbing boundary conditions. Other boundary conditions, such as periodic boundary, metal boundary, and symmetrical boundary, are used depending on the requirements of the specific simulation problem (Harms et al., 1994, Mezzanotte et al., 1995).

The source is an essential point of FDTD simulation is the definition of a wave through the function of electric and magnetic components with respect to time ($f(n\Delta t)$). The wave source can be categorized as periodic and pulse source. Figure 4.2 demonstrates the field's source conditions.
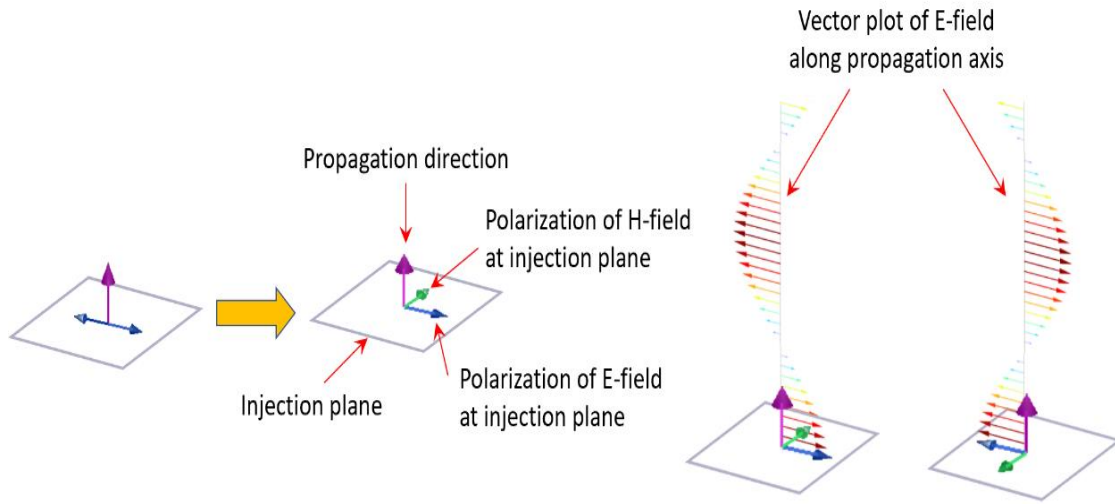
Figure 4.2: FDTD field source (<u>Plane wave and beam source - Simulation object – Ansys Optics</u>*)*

In FDTD, equation 4.11 demonstrates three wave sources: sine wave, Gaussian pulse, and bandpass filter Gaussian pulse. The sine wave is a periodic source, and the Gaussian pulse is a pulse-type source, with the Gaussian pulse being most commonly used for FDTD because it can replicate a wideband source. Furthermore, the wave source function requires different spatial rearrangements for various simulations and is classified as a surface, line, or point source.

$$f(n\Delta t) = (\sin(2\pi f_0 n\Delta t)) \text{ Sine wave}$$

$$f(n\Delta t) = e^{-\left[\frac{n-n_0}{n_{decay}}\right]^2} \text{ Gaussian pulse} \qquad 4.11$$

$$f(n\Delta t) = e^{-\left[\frac{n-n_0}{n_{decay}}\right]^2} \sin\left(2\pi f_0 (n-n_0)\Delta t\right) \text{ Bandpass filter Gaussian pulse}$$

The modern FDTD becomes more efficient and faster with these boundary conditions and source functions. There are already many commercial simulation programs on the market. Lumerical FDTD solvers were used for all FDTD simulations in this thesis.

4.1.1 FDTD Simulation Procedure

The FDTD solver is compatible with various boundary conditions, including periodic and Bloch. In addition, the FDTD solver provides several features, such as the conformal mesh algorithm, which enable accurate results to be obtained even when employing a relatively coarse mesh. The periodic boundary that we used is to understand the behaviour of each material attribute within the structure, and the response should be symmetric at all the boundary locations. In optics, the refractive index measures the bending light when passing from one medium into another or refracted when entering a medium, and the complex refractive index $(n(\omega))$ can be described as the function with respect to the incident wave. Figure 4.3 demonstrates the FDTD modelling arrangement.
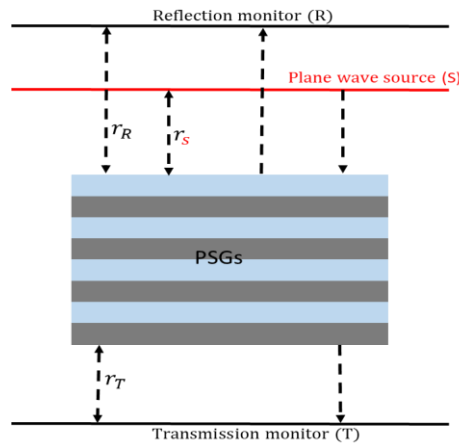
Figure 4.3: the PSG/PIRAs simulation arrangement for source and monitors

As the literature demonstrates, Maxwell's equations are the physics behind our simulation work. It is split into two independent sets of equations composed of three vector quantities, each of which can only be solved in the *x* and *y* plane. These independent TE and TM can be translated with the following condition (TE consider E_x, E_y, H_z, and TM consider H_x, H_y, E_z).

4.1.2 Materials Simulation Interest

Defining the correct material properties in optical simulations is essential to obtain accurate simulation results. Defining real and imaginary parts of the refractive index, including permittivity as a function of wavelength or frequency. The data of the materials must be closely related to experimental conditions. Figures 4.4 to 4.8 exhibit the simulation data used in the PSG and PIRA.

Metallic pattern: silver (Ag) and gold (Au) are the most common noble metals used in plasmonic materials.

Optical benefits: negative permittivity (Johnson and Christy, 1972, Debnath and Ghosh, 2022, Babar and Weaver, 2015), high reflectance (Babar and Weaver, 2015) and can be measured in the wavelength range of 0.5 to 32 μm (Bennett and Ashley, 1965).

Dielectric materials: silicon dioxide (SiO_2) and titanium dioxide (TiO_2) as dielectric spacers

Optical benefits: include low mid-infrared absorption properties, highly reflective light combined, and high melting points.

TiO_2 has a very high refractive index and is widely used in thin-film optics. When used for optical interference, TiO_2 is typically one component of alternating layers of high and low refractive index materials that tailor the spectral reflectance profile of the thin film. It also creates optical filters, reflectors, and antireflective coatings for eyeglasses and other lenses. Titanium dioxide is frequently used in conjunction with SiO_2.

The optical material silica, or SiO_2 glass, is essential in many technological aspects. For example, optical fibres transfer data across the Internet because they have extremely low absorption and scattering losses during signal transmission (Griscom, 1991, Mizoguchi et al., 2013) and excellent optical transmittance properties in the UV region. SiO2 is also used for lenses in semiconductor exposure apparatus, which govern the fabrication of advanced semiconductor chips with very thin wire electrodes (Kajihara, 2007). It is an important material for many applications in science and technology.

Metal stacked: chromium (Cr) is commonly used as blackbody material.

Optical benefits: higher reflectivity and good reflectors.

Plasmon enhancement: graphene 2D surface conductivity.

Optical benefits: It has unique properties such as optical transparency, flexibility, high electron mobility, and conductivity, which can be tuned by electrochemical potential via electrostatic gating, magnetic fields, or optical excitation (Bolotin et al., 2008, Geim, 2009, Novoselov et al., 2012). Graphene can support surface plasmon polaritons in the infrared range (Bao and Loh, 2012, Koppens et al., 2011, Hill et al., 2009, Grigorenko et al., 2012). It enables radiation control for such devices as modulators, tunable reflectors (Fallahi and Perruisseau-Carrier, 2012, Yan et al., 2012), filters, absorbers, and polarizers (Alaee et al., 2012). However, it has an enormous absorption of 2.3% per monolayer in the optical range.

❖ **Silver (Ag) and Gold (Au)**
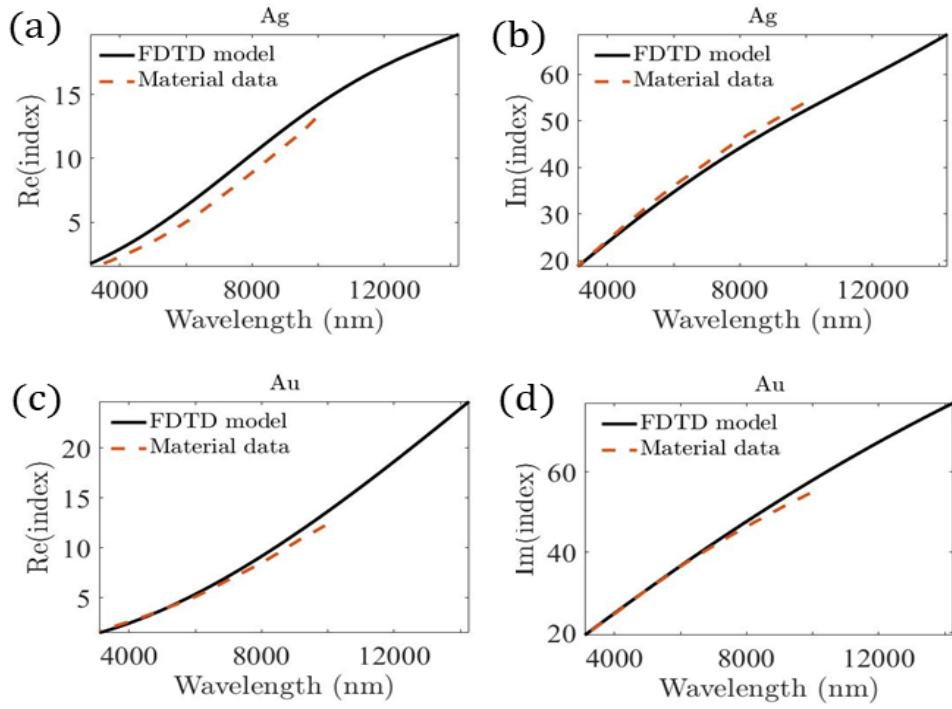
Figure 4.4: Noble metal analysis, on FDTD model and material data, (a) real index of Ag, (b) imaginary index of Ag, (c) real index of Au, (d) imaginary index of Au
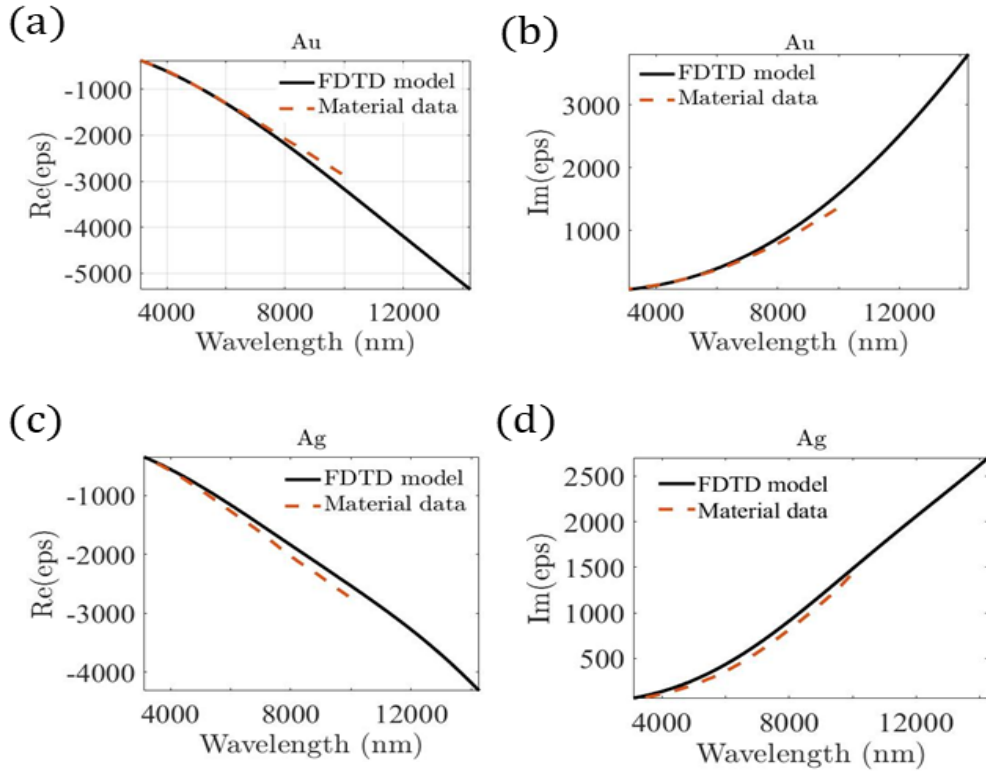
Figure 4.5*: A noble metal analysis based on the dielectric parameter (ε) for analysis between FDTD model and material data, (a) real epsilon of Au, (b) imaginary epsilon of Au, (c) real epsilon of Ag (d) imaginary epsilon of Ag.*

❖ Chromium (Cr)
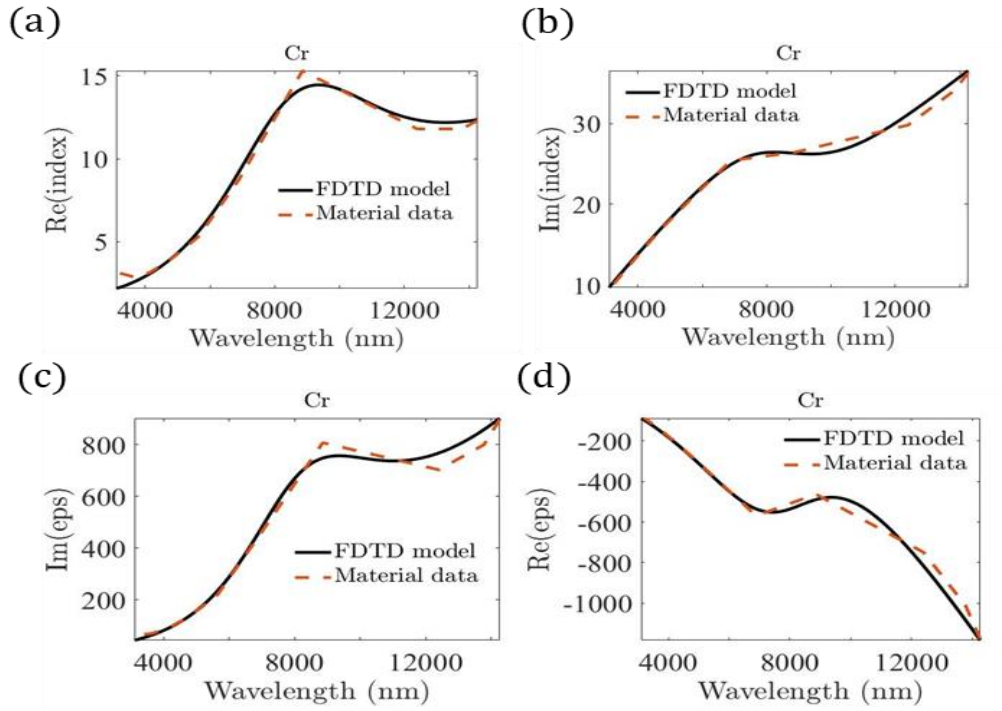
Figure 4.6: (a)Cr real part index, (b) Cr imaginary part index, (c) Cr real part (epsilon), (d) Cr imaginary part (epsilon)

❖ Silicon dioxide (SiO₂) and Titanium dioxide (TiO₂)
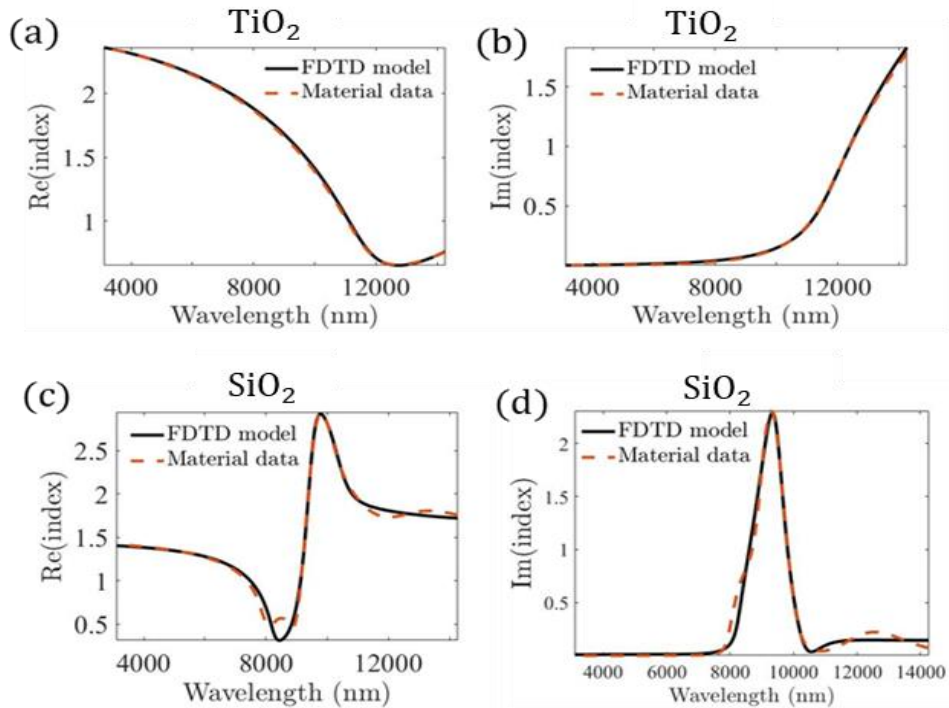
Figure 4.7: Refractive index of the dielectric material within the simulation range, including material data and FDTD model (a)TiO₂ real part, (b) TiO₂ imaginary part, (c) SiO₂ real part, (d) SiO₂ imaginary part.

❖ **Graphene (σ)**
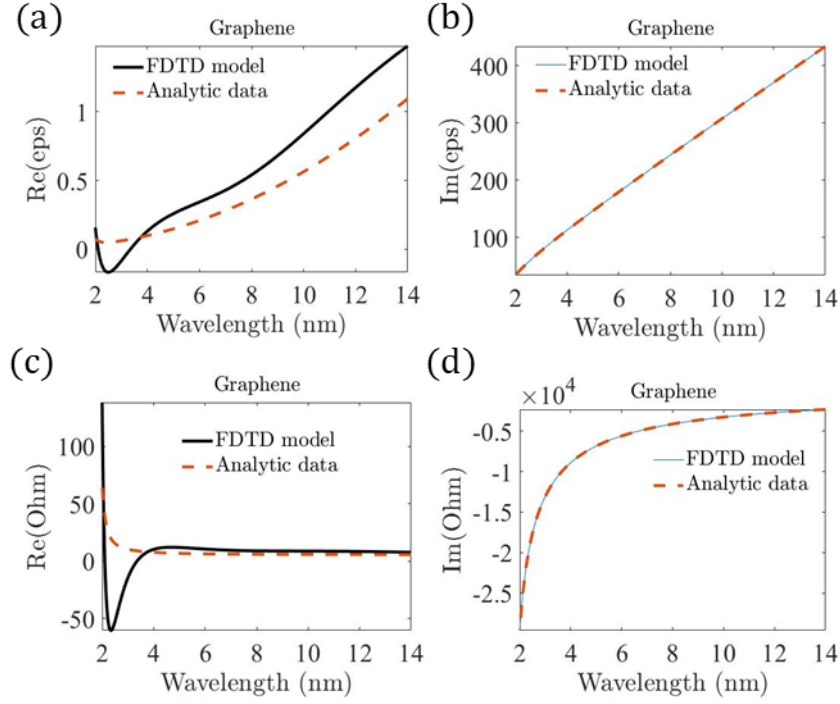
Figure 4.8: Graphene complex conductivity including resistance analysis data (a) Real part, (b) Imaginary part, (c) Real part (resistance), (d) Imaginary part (resistance)

The transmission line comparison is used in this study's surface conductivity method. An equivalent transmission line with perfect electric and magnetic boundary conditions is used for plane wave propagation. We showed an example guide that we used to achieve our desired interest by assuming that a thin conducting layer with surface conductivity at the flat boundary between two different refractive indexes is equivalent to a load attached to the junction between two transmission lines, as shown in Figure 4.9 for interface conditions(Andryieuski and Lavrinenko, 2013).
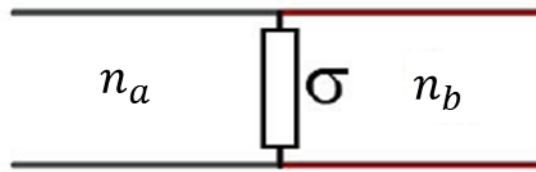
Figure 4.9: The conductive interface with two different indices.

We take the thickness of the conductive layer into account. If the thickness of the conductive layer is much smaller than the incidence wavelength, we can ignore the thickness and treat the

layer as a point load. The amplitude transmission and reflection coefficients for an incidence wave from the first material interface at normal incidence are as follows:

$$t = \frac{2n_a}{n_a + n_b + \sigma_s Z_o} \tag{4.12}$$

$$r = \frac{n_a - n_b - \sigma_s Z_o}{n_a + n_b + \sigma_s Z_o} \tag{4.13}$$

Where Z_o is the free-space impedance, and $\sigma_s = \infty$ the wave will be reflected entirely (r = −1). Surface conductivity equal to zero displays no effect, and the formulas become standard Fresnel for the interface between two materials. We also study TE and TM polarisations, and then the transmission and reflection coefficients become:

$$t_{TE} = \frac{2k_a}{k_a + k_b + \sigma_s Z_o} \tag{4.14}$$

$$r_{TE} = \frac{k_a - k_b - \sigma_s Z_o}{k_a + k_b + \sigma_s Z_o} \tag{4.15}$$

$$t_{TM} = \frac{2\rho_a}{\rho_a + \rho_b + \sigma_s Z_o} \tag{4.16}$$

$$r_{TM} = \frac{\rho_a - \rho_b - \sigma_s Z_o}{\rho_a + \rho_b + \sigma_s Z_o} \tag{4.17}$$

Where $\rho_{a,b} = \varepsilon_{a,b}/k_{a,b}$ and $k_{a,b} = \sqrt{\varepsilon_{a,b} - \sin^2 \theta}$ is the normalized normal component of the propagation constant and $\varepsilon_{a,b} = n_{a,b}^2$, are the relative dielectric constants.

$$t = \frac{2}{1 + \gamma + S + jS} \tag{4.18}$$

$$r = \frac{1 - \gamma - S - jS}{1 + \gamma + S + jS} \tag{4.19}$$

Where $\gamma = n_b/n_a$, is the ratio of the refractive indices and $S + jS = (\sigma_s' + \sigma_s'') z_0/n_a$, is the normalized surface conductivity. Structuring the graphene layer changes the surface conductivity by reducing the conductive material and introducing plasmonic resonances: the power transmittance, reflectance and absorbance of the considered conducting layer.

$$T = \gamma|t|^2 = \frac{4\gamma}{(1 + \gamma + S)^2 + S^2} \tag{4.20}$$

$$R = \frac{(1-\gamma-S)^2+S^2}{(1+\gamma+S)^2+S^2}$$

4.21

$$A = 1 - R - T = \frac{4S}{(1+\gamma+S)^2+S^2}$$

4.22

In this step, the maximum absorption occurs when the $S = 0$ and $S = 1 + \gamma$. We can obtain more significant absorbance for $\gamma < 1$ that corresponds to the circumstance of incidence from a high-refractive index to lower refractive index material ($n_a > n_b$). We can achieve greater absorbance using more conductive layers, including fast-response emission. It is straightforward to describe the properties of graphene in terms of surface conductivity because this quantity can be measured directly across a wide range of the electromagnetic spectrum. The conductivity of graphene is described using interband and intraband contributions.

4.2 Modelling Thermal Emission

Studying an object's thermal emission needs to simplify its absorptivity spectrum, knowing that the object's absorptivity and emissivity spectra are identical. Moreover, to develop an understanding of the physics behind the thermal emission spectrum, it is more helpful to think about absorption rather than emission. We used a plasmonic field based on metamaterial to possess a narrow thermal radiation light source spectrum at the mid-infrared region. We explained the equivalent transmission line model and demonstrated the characteristic impedance of the metallic grating and dielectric layers, including the corresponding wave vector in Figure 4.10. We calculated our bandgap to achieve zero light reflection by considering both side impedances (air and material).

(a)   (b)
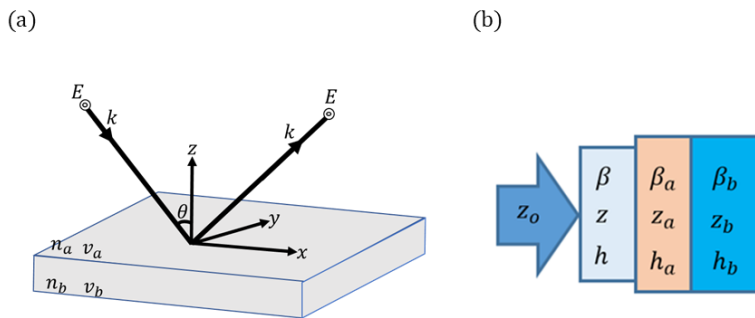
Figure 4.10: (a) Refraction of light caused by changing the velocity of light in the second medium, (b) the equivalent transmission line model of the structure, where β, β_a and β_b are their corresponding wave vector, h, h_a and h_b, are dielectric layers and z, z_a and z_b, are the characteristic impedance of the metallic grating.

According to Snell law, $n_a sin\theta_a = n_b sin\theta_b$ where, n_a and n_b are the material index and θ_a and θ_b are the incident angles here $\theta_r = \theta_b$. Therefore, our design structure is characterised by the stacked pattern and can be studied as a one-dimensional multilayer structure composed of a slab with permittivity (ε_{eff}) and permeability (μ_{eff}) followed by a 1D-BG.

The reflection, transmission, and absorption are logically investigated by the transfer matrix method (TMM) (Born and Wolf). The characteristic impedance of the air and our noble structure are demonstrated in equation 4.23 and displayed in Figure 4.10(b) for the transmission line (Gong et al., 2013b):

$$z_{PMM_s} = \xi_{n+1} = \xi_o = z_o \qquad 4.23$$

Where, ξ_o and z_o are characteristic impedance for air (free space), z_{PMM_s} and ξ_{n+1}, are characteristic impedance for the whole PMMs and ($n = 1,,,N$). The interaction of the plane wave with a metallic surface, the behaviours calculates the effective metamaterial like homogeneous slab with effective permittivity $\varepsilon_{eff} = {\varepsilon_r d}/{w}$ and permeability $\mu_{eff} = w(\beta_s^2/k_o^2 + sin^2\theta)/d$. The conservation momentum for the homogeneous slab is described in equation 4.24. We also consider the effective metamaterial slab whose constitutive parameters, including spatial dispersion effects, are in equation 4.25 respectively.

$$\varepsilon_{eff}\,\mu_{eff}k_o^2 = k_o^2 sin^2\theta + \beta_s^2 \qquad 4.24$$

$$z_{eff} = \sqrt{\frac{\mu_{eff}}{\varepsilon_{eff}}}\sqrt{1 - \frac{sin^2\theta}{\varepsilon_{eff}\mu_{eff}}} = \frac{1}{d}\int_{-d/2}^{d/2}\frac{E_x(x)}{H(x)}\,dx = \frac{w}{d}\frac{\beta_s}{k_o\varepsilon_r} \qquad 4.25$$

Where ε_r, is the dielectric constant, E and H are the transverse components of the electric and magnetic field, k_o, is the free space wave vector, and β_s, is the wave vector for free space and guided mode.

In the limit of ultranarrow, we demonstrated how we control the geometric structure by manipulating the metallic surface of the PMM structures, which can be understood by controlling the propagation direction of the metallic pattern. Also, the reflection coefficient at the metallic entrance of the PMMs can be considered as follows:

$$R = \frac{(z_{PMMs}^2 - z_o^2)\tan(\beta_s h)}{(z_{PMMs}^2 + z_o^2)\tan(\beta_s h) + 2iz_{PMMs}z_o} \qquad 4.26$$

Therefore, PMM structural example in Figure 4.10, the metallic pattern is corrugated by air slits. The electric field (E) within the slit is characterised by dependence on the width of the groove. For instance, the electric field's spatial component dependent on (x) within the air slit may be expressed from the lowest order mode. Therefore, when $x = |x| - w/2$, then:

$$E(x,z) = \cosh(\sqrt{k_o^2 - k_z^2}x) \exp(k_z z)$$
$$\text{4.27}$$

when $x = |x| + w/2$

$$E(x,z) = \frac{1}{\varepsilon_r}\cosh(\sqrt{k_0^2 - k_z^2}\,x)\exp\left[-\sqrt{k_z^2 - \varepsilon_r k_0^2}(|x| - x)\right]\exp(jk_z z)$$
$$\text{4.28}$$

The propagation constant of the mode (Gordon and Brolo, 2005)

$$\tanh(\sqrt{k_o^2 - k_z^2}x) = \frac{-\sqrt{k_z^2 - \varepsilon_r k_0^2}}{\varepsilon_r\sqrt{k_z^2 - k_o^2}}$$
$$\text{4.29}$$
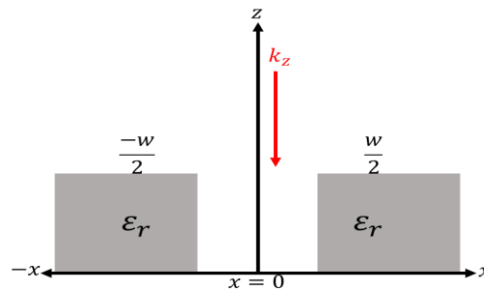
*Figure 4.11: Schematic representation of a slit in metal with the negative dielectric constant(ε_r). The width is **w** and equal to **x** in the corrugation boundary where **x = 0** in the middle of **z − direction** in the air slit.*

The free space region's electric field (E_o) is indicated as an infinite sum of a plane wave with TM polarisation. The effective index at the lowest TM mode inside the air slit, k_z/k_o (if we consider the PMM metallic pattern in Figure 4.11), as a function of the slit width with different values of the dielectric constant of the metal. Therefore, calculate the mode's reflection coefficient (r) in the slit at the free-space boundary. The tangential components of the electric and magnetic fields must match at the free-space edge at z = 0. The electric field in free space is written as an infinite sum of plane waves with polarisation direction:

$$E_x(x,z) = \int_{-\infty}^{\infty} E_x(\beta)\exp(j\beta x + jk_z z)\,d\beta$$
$$\text{4.30}$$

Where: $E_0(\beta)$ is the amplitude of the electric field for a plane wave with x component of the wave vector β, and $\beta = k_x$, k_z, is the propagation constant in the $z -$ direction. Since the incident EM wave along the $z -$ direction is $E_z = E e^{-jkz}$ where k due to loss is complex and components k_x and k_y are determined by the incident wave vector k or k_z, and the direction of incidence k are equal throughout the structure.

$$k_x = k_{x(incidence)} = k_o\sqrt{\varepsilon\,\mu\,cos\varphi\,sin\theta} \qquad 4.31$$

$$k_y = k_{y(incidence)} = k_o\sqrt{\varepsilon\,\mu\,sin\varphi\,sin\theta} \qquad 4.32$$

$$k_{z,i} = \sqrt{{k_o}^2\,\varepsilon_i\mu_i - k_x^2 - k_y^2} \qquad 4.33$$

Where i is the number of the material layer, which is composed of two alternately arranged interface layers for the index of refraction n_a and n_b. It is essential to note that with the symmetry modes, the system can be divided into transverse electric (TE) and transverse magnetic (TM) modes, the plane wave due to the system's mirror symmetry in a plane perpendicular to x and y. The x-polarised and y-polarised modes do not mix, and we examine these two polarisations independently.

4.2.1   Field Dispersion Relation

We emphasise the related quantity field that is time and position dependent. The complex or real wave vectors provide a detailed description of the field. We use a mathematical transform that decomposes functions into frequency components, with the transform's output being a frequency-dependent function. Most commonly, functions of time or space are transformed, giving a function based on the temporal or spatial frequency, respectively. The metal contribution to the integral can be extracted when the field is excited by sources at the interface. According to Sommerfeld's definition, the surface wave is the contribution of the pole of the Fresnel reflection or transmission factor to the integral.

Furthermore, a linear wave equation of modes with wave vector k and frequency ω can represent the field. The different representations of the field can be derived using modes exemplified by a frequency ω and a wave vector β. A material interface metal and dielectric can support SPPs with the boundary condition lay in x and y plane. The x component of the wave vector and E-field has harmonic time dependence.

$$E(x, y, z) = E(z) \exp j(k_x x - \omega t) \qquad\qquad 4.34$$

Where the $k_x = [k_{SPP}^2 - \beta^2]^{1/2}$, and The z-component of the wavevector is given in the usual form as $k_z = [\varepsilon_m k_o - k_{SPP}^2]^{1/2}$.

However, as k_x maybe complex, then the propagation term may describe as $\exp j(k_x x)$ and introduces dumping. For lossy medium, damping can be due to losses, even for non-lossy-medium (k_{SPP}, is real) and k_x, can be imaginary when β exceeds the value k_{SPP}. The 2D equivalent of evanescent waves with wavevector k greater than k_o, and cannot propagate in free space or a vacuum. k_{SPP} is a cut-off frequency, and the propagation term $\exp j(k_x x)$ works as a low-pass filter that prevents the propagation of fields associated with spatial frequencies larger than k_{SPP}. For the lossy media, it is the real part of k_{SPP}, which specifies the cut-off frequency. Changing the mode's phase and amplitude allows us to discuss any surface wave diffraction problem. For the sake of simplicity, the time dependence $\exp(-j\omega t)$ will be omitted, and then:

$$E(x, y) = \int \frac{\partial \beta}{2\pi} E \exp j\sqrt{k_{SPP}^2 - \beta^2}\, x + j\beta y \qquad\qquad 4.35$$

This expansion is similar to the angular plane wave representation of fields in a vacuum. It is valid for $z > 0$ in a source-free region. Since we consider the propagation of the surface plasmon field along a planar surface $z = 0$ in the direction of positive (x), we assume that the domain is identified at $z = 0$. For the upper medium, the field exponential describes as $\exp(j\sqrt{\varepsilon_d \omega^2 / c^2 - k_{SPP}^2}\ z)$, and in the down medium (in the metal), the exponential can be described as $\exp(-j\sqrt{\varepsilon_m \omega^2 / c^2 - k_{SPP}^2}\ z)$. The x and y-components of the electric field can be derived from the form of the z-component.

$$E_x = \sqrt{k_{SPP}^2 - \beta^2}\ \frac{k_z}{k_{SPP}^2} E_z \qquad\qquad 4.36$$

$$E_y = k_y\ \frac{k_z}{k_{SPP}^2} E_z \qquad\qquad 4.37$$

Where, $k_z = \sqrt{k_{SPP}^2 - \varepsilon_d \frac{\omega^2}{c^2}}$, is the z-component of the wavevector in the surrounding dielectric area.
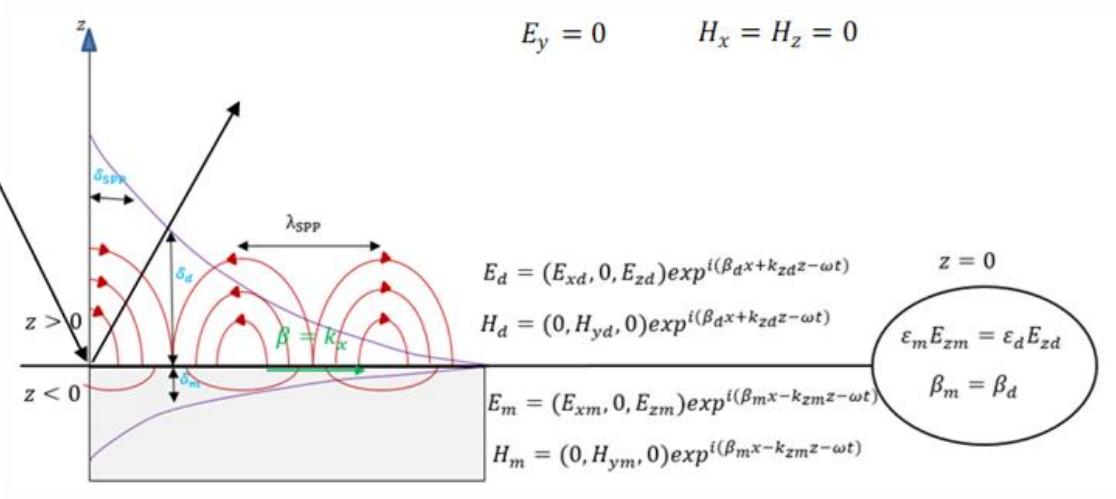
Figure 4.12: (a) Electric field lines and charge distribution for an SPP propagating at the interface between a metal/dielectric.

The dispersion relation of the SPP or the propagation that bound along with the interface concerning the real axis along the *x*-direction (β) and the imaginary axis along the *z*-direction(k_z) are:

$$\beta_z(\omega) = k_o \left(\frac{\varepsilon_a \varepsilon_b}{\varepsilon_a + \varepsilon_b}\right)^{1/2} = k_{spp} \qquad 4.38$$

Hence, $\beta_z = k_{x,z}$

The propagation of surface plasmon polaritons along a flat interface is investigated. Several experiments demonstrating surface plasmon propagation, interferences, and diffraction have been reported in the literature (Feng et al., 2007, Liu et al., 2005, Yin et al., 2005, Huber et al., 2008, Zia and Brongersma, 2007). The details of the field dispersion relation we represented in this thesis correspond comparably to our situation design structure, which was founded in the framework of optical physics based on the Huygens–Fresnel principle(Teperik et al., 2009).

4.2.2   Reflection and Transmission

After introducing electromagnetic waves and the fundamental relationship that governs the propagation of waves, most materials lie on a range of properties, and the characterisation is based on the dominant property of the material. Conductor and dielectric are examples of properties. Electromagnetic waves propagate on those properties; two essential parameters must be noticed: ε and μ. These parameters always allow the perfect calculation of electromagnetic waves travelling within and at the materials' surface. Permittivity ε and

permeability μ are two fundamental properties of materials that explain how they respond to electric, magnetic, or electromagnetic fields (Huang et al., 2007, Charles et al., 2021, Gou et al., 2018, Landy et al., 2008a). These parameters behave, allowing new varieties of components, structures and devices to create (Kshetrimayum, 2005). In terms of complexity function, it can be related to the refractive index $n(\omega)$ and the impedance (η). The $\boldsymbol{E}$ and $\boldsymbol{H}$ related through the impedance can be described in terms its phasor form:

$$\boldsymbol{E} = \boldsymbol{E}\hat{a}_x = \boldsymbol{E}_0 \exp(-j\boldsymbol{k}z)\hat{\boldsymbol{a}}_x \qquad 4.39$$

And

$$\boldsymbol{H} = \boldsymbol{H}_0 \exp(-j\boldsymbol{k}z)\hat{\boldsymbol{a}}_y \qquad 4.40$$

Where $\hat{\boldsymbol{a}}$, is the unit vector along the polarisation direction. The impedance can be expressed in the units of ohms as:

$$\eta = \frac{E}{H} = \frac{\omega\mu}{k} \equiv \sqrt{\frac{\mu}{\varepsilon}} \qquad 4.41$$

Therefore, since $\eta = E/H$, and the E-field propagates in the forward or backward z-direction with respected polarisation direction x, then the H-field can be found as:

$$\text{Forward} \qquad \boldsymbol{H} = \left(\frac{E}{\eta}\right)\exp(-j\boldsymbol{k}z)\hat{\boldsymbol{a}}_y \qquad 4.42$$

$$\text{Backward} \qquad \boldsymbol{H} = -\left(\frac{E}{\eta}\right)\exp(j\boldsymbol{k}z)\hat{\boldsymbol{a}}_y \qquad 4.43$$

Moreover, in a simple uniform plane wave, the E and H lie in the transverse plane mode and are orthogonal; their amplitudes are related through $\boldsymbol{E} = \eta\boldsymbol{H}$ and phase constant $\boldsymbol{\beta} = \boldsymbol{k}$. The reflection and transmission of plane waves at the interface of two different materials are useful for developing and comprehending light interaction behaviour. The optical power reflected and transmitted, including phase shifts on reflection, is a function of incident angle and field polarisation. Electromagnetic waves at the interface between two media, according to Snell's theorem, the angle between the normal and the transmitting wave varies from the angle between the incident wave and the normal, as illustrated in Figure 2.13.
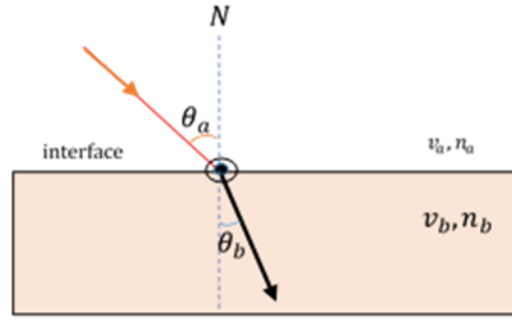
Figure 4.13: Refraction of light caused by changing the velocity of light in the second medium.

This change in the transmitted angles originates from the wavelength dependence of the refractive index. To formally derive these behaviours, we consider the polarisation-dependent properties of EM-waves that are incident on the interface of two different materials, as we presented in Figure 2.14 for more expanded. We consider two other polarisation states of a homogeneous plane wave: one in which the electric field is perpendicular to the incidence plane as a transverse magnetic (TM) wave (P-polarised) and another one with the electric field parallel to the plane of incidence as transverse electric (TE) wave (S-polarised) as illustrated below.
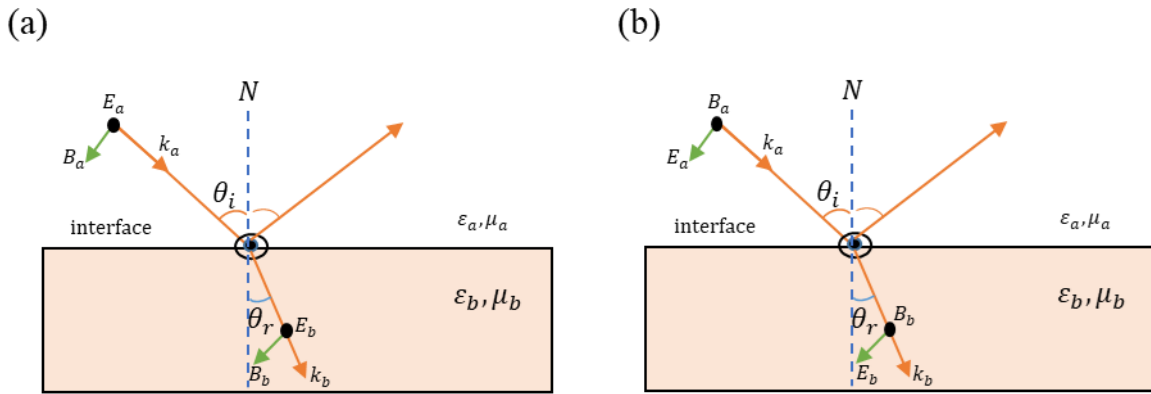
Figure 4.14: Representation of P-polarised and S-polarised electromagnetic radiation incident upon a planar Interface between two media at an angle of incidence. (a) TM mode, and (b) TE mode

For both polarisations, the boundary conditions need to be applied to derive the propagation performance of the incident wave at the interface. Three waves are involved in this procedure, which depends on the material properties of both media: the incident wave, the transmitted wave, and the reflected wave.

For incident wave $\quad \boldsymbol{E}_a = \boldsymbol{E}_{a,0} \exp j(\boldsymbol{k}_a \cdot \boldsymbol{r} - \omega t)$ $\qquad$ 4.44

$$B_a = \sqrt{\varepsilon_a \mu_a} \; \frac{E_a k_a}{k_a} \tag{4.45}$$

Transmission wave
$$E_b = E_{b,0} \exp j(k_b \cdot r - \omega t) \tag{4.46}$$

$$B_b = \sqrt{\varepsilon_b \mu_b} \; \frac{E_b k_b}{k_b} \tag{4.47}$$

Reflected wave
$$E_{a\prime} = E_{a\prime,0} \exp j(k_{a\prime} \cdot r - \omega t) \tag{4.48}$$

$$B_{a\prime} = \sqrt{\varepsilon_{a\prime} \mu_{a\prime}} \; \frac{E_{a\prime} k_{a\prime}}{k_{a\prime}} \tag{4.49}$$

At the interface, the two refractive indices as $n_a(z > 0)$ and $n_b(z < 0)$, the propagation direction and wavelength of the incident wave are characterised by the wave vector k. To determine the boundary conditions of the transmitted and reflected, we need to use the boundary that requires continuity of tangential components of the electric and magnetic field across the interface, which can be defined as:

$$\begin{bmatrix} \varepsilon \big(E_{a,(z=0)} + E_{a\prime,(z=0)}\big) = E_{b,(z=0)} \\ \mu \big(H_{a,(z=0)} + H_{a\prime,(z=0)}\big) = H_{b,(z=0)} \end{bmatrix} \tag{4.50}$$

At the interface, all fields' spatial and time variation must be the same, which implies that all phase vectors should be equal, independent of the boundary conditions. Since the $(k_a \cdot r) = (k_b \cdot r) = (k_{a\prime} \cdot r)$ this indicate all the three-wave vector lie on the same plane, and r can be described as $x\hat{a}_x + y\hat{a}_y + z\hat{a}_z$. As a result, the wave vector for the TE and TM cases is defined as:

$$\begin{bmatrix} k_{inc} = k_a z\hat{a}_z + k_a x\hat{a}_x = n_a k_o cos\theta_i \hat{a}_z + n_a k_o sin\theta_i \hat{a}_x \\ k_{ref} = k_a z\hat{a}_z + k_a x\hat{a}_x = -n_a k_o cos\theta_{r\prime} \hat{a}_z + n_a k_o sin\theta_{r\prime} \hat{a}_x \\ k_{trans} = k_b z\hat{a}_z + k_b x\hat{a}_x = n_b k_o cos\theta_r \hat{a}_z + n_b k_o sin\theta_r \hat{a}_x \end{bmatrix} \tag{4.51}$$

For the S-polarised wave, the equation from 4.50 can be re-written as

$$E_{a,0} + E_{a\prime,0} = E_{b,0} \tag{4.52}$$

$$\sqrt{\varepsilon_a \mu_a}(E_{a,0} - E_{a\prime,0})cos\theta_i = \sqrt{\varepsilon_b \mu_b} E_{b,0} cos\theta_r \tag{4.53}$$

Therefore, the relative amplitudes of the refracted and reflected waves are obtained, which gives the following complex transmission and reflection coefficients at that boundary:

$$\begin{cases} r_{s(TE)} = \dfrac{E_{a,0}}{E_{a,0}} = \dfrac{n_a \cos\theta_i - n_b \cos\theta_r}{n_a \cos\theta_i + n_b \cos\theta_r} = \dfrac{k_a - k_b}{k_a + k_b} \\ t_{s(TE)} = \dfrac{E_{b,0}}{E_{a,0}} = \dfrac{2k_a}{k_a + k_b} = 1 + r_{s(TE)} \end{cases} \qquad 4.54$$

Similarly, the *E* and *H* tangential components must be continuous for P polarised. We can write the relative field amplitudes as a function of the properties of the incident wave, which gives the following complex transmission and reflection coefficients:

$$\begin{cases} r_{p(TM)} = \dfrac{E_{a,0}}{E_{a,0}} = \dfrac{n_a/\cos\theta_i - n_b/\cos\theta_r}{n_a/\cos\theta_i + n_b/\cos\theta_r} = \dfrac{n_b^2 k_a - n_a^2 k_b}{n_b^2 k_a + n_a^2 k_b} \\ t_{p(TM)} = \dfrac{E_{b,0}}{E_{a,0}} = \dfrac{2n_a n_b k_a}{n_b^2 k_a + n_a^2 k_b} = \dfrac{n_a}{n_b}\left(1 + r_{p(TM)}\right) \end{cases} \qquad 4.55$$

The propagation behaviour of EM waves is described from equations 4.54 and 4.55, known as the Fresnel equations, which represent the reflection and transmission of plane waves at the interface of nonmagnetic materials.

4.3 Classic Techniques on Plasmon Control

The oscillating electric field from the incident electromagnetic wave is coupled with the SPR, or, more precisely, the SPP, at a metal and dielectric material junction when its momentum matches the plasmon. The techniques used to couple the incident electromagnetic wave onto the material interface and used to demonstrate the idea behind active control over the excitation of SPP by the prism and grating coupling. Prism enables SPP to be coupled with the evanescent electromagnetic field created by dampened total internal reflection. This coupling technique can be used in Kretschmann and Otto configurations (Zayats et al., 2005), as shown in Figure 4.15. The two main coupling techniques, grating and prism, demonstrate the principle underlying active control surface plasmon.
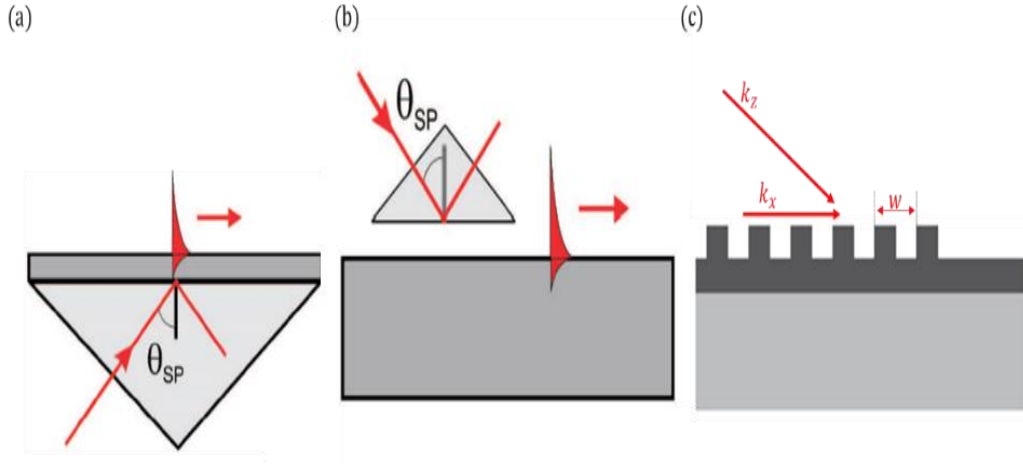
Figure 4.15: Coupling techniques (a) prism coupling of the Kretschmann configuration, (b) prism coupling of the Otto configuration, and (c) grating coupling of a light impinging on a metal grating surface of period w along the x-direction(Maier, 2007, Zayats et al., 2005).

4.3.1   Prism Coupling

The prism allows for the Coupling of SPP with the evanescent electromagnetic field produced by attenuated total internal reflection, applicable for both Kretschmann and Otto configurations.

4.3.1.1   Kretschmann configuration

The high-refractive-index prism (n_{prs}) is interfaced with metal and dielectric, the metal film with a sufficiently small thickness, which is usually less than 100 nm, and a dielectric with a refractive index n_a ($n_a < n_{prs}$) (Kretschmann and Raether, 1968). A light wave passing through the prism can be reflected and propagated in the metal as an evanescent wave when the incidence angle of the light wave is above the critical angle. The evanescent wave penetrated through the thin metal film. It coupled with the surface waves at the metal and dielectric meeting junction by controlling the angle of incidence on the base of the prism according to the expression:

$$k = \frac{2\pi}{\lambda} n_{prs} \, sin\theta = Re\{k_{SPP}\} \qquad 4.56$$

Where k, represent the propagation constants of the evanescent wave and k_{SPP}, represent surface waves as SPP propagation at the metal and dielectric interface. The surface waves excited by incident electromagnetic waves under specific coupling conditions are detected as a dip at a particular wavelength in the spectrum of the light reflected from the prism. The

challenge with this configuration does not arise in SPP excitation when direct contact between the prism and the metal surface, or when the metal film isn't sufficiently thin to allow penetration of the evanescent electromagnetic wave. Refer to Figure 4.15 (a) for the presented configuration.

4.3.1.2   Otto configuration

In the Otto configuration, where a dielectric layer with a refractive index n_a smaller than that of the prism n_{prs} and is deposited between the prism and the metal film n_b. The incident electromagnetic wave at a certain angle can be reflected at the interface between the prism and the dielectric layer, producing an evanescent wave decaying exponentially with distance in the dielectric layer (Otto, 1968). Suppose the thickness of the dielectric layer is changed correctly, usually a few hundred nanometer (100 nm) in the optical regime. In that case, the evanescent wave can reach the dielectric and metal interface with enough for the excitation of the SPP. The controllable factors on the excitation of the surface plasmon include the incidence of electromagnetic waves that can change the resonance strength of the SPP, which can be observed by the amplitude modification of the light reflected from the prisms (Sincerbox and Gordon, 1981, Dawson et al., 2000). The amplitude of the light reflected from the prism base is changed by varying the thickness of the gap.

4.3.2   Grating coupling

Grating Coupling is another technique for the optical excitation of surface waves based on the diffraction of light on a grating pattern on the metal surface. The diffracted light couples to the surface wave or, more clearly, SPP if the momentum k of the diffracted light parallel to the grating surface is equal to the propagation constant of the SPP (Grigorenko et al., 1999). This coupling processes can be mathematically expressed as:

$$kn_a \, sin\theta \;\pm \Lambda \frac{2\pi}{d_W} = Re\{k_{SPP}\} \qquad 4.57$$

Where w is the grating period, and $\Lambda =$ is the given grating pattern on the metal surface ($\Lambda = 1$, 2, 3…,), Λ and d_W are constant parameters in the structure. As a result, the wavelength of the incident electromagnetic wave in the grating coupling was controlled by the surface wave excitation. Metallic cavity arrays are an extreme type of grating. The evanescent field associated with surface waves can span the metal film and be scattered by the periodic surface

arrangement, allowing the surface wave to be scattered into the transmitted light, which can be realized by measuring light transmission through the metal film (Garcia-Vidal et al., 2010). In this coupling scheme of Figure 4.15 (c), the incident electromagnetic wave's polarisation state also governs the surface wave's excitation.

According to Maxwell's equations and the boundary conditions, SPP (surface wave) propagation along the interface between a metal and a dielectric is possible only for TM polarisation. Therefore, controlling the polarisation state of the incident electromagnetic wave is an effective way to vary the strength of the surface wave as SPP. For an interface structure composed of complex and anisotropic dielectric material and a metal, the surface wave can be excited by TM and TE polarised light (Li et al., 2008, Abdulhalim, 2008), and control over these polarisation states can enable the SPP with tunable directionality. The dispersion of LSPR supported by metal nanoparticles allows for its excitation by incident electromagnetic waves over the widespread angle. These excitations can be uncoupled and coupled due to the wavelength and polarisation state.

4.4 Media Interface

We considered two different media; the first is a lossy dielectric medium, which is defined as a medium in which the electric conductivity is not equal to zero and it is not a good conductor; the second is a lossless medium, which is a medium with zero conductivity and finite permeability and permittivity. The electromagnetic wave passes through this medium, and the amplitude of the electric or magnetic field remains constant throughout the propagation. As a result, the PMM structure's absorption resonance peak was determined by the metal's finite conductivity. The imaginary part of the metal's complex permittivity characterises finite conductivity, and surface plasmons can exist when the real part of the complex permittivity dominates and is negative (Raether, 1988a). When the material in the structure is lossy, light absorption at the wavelengths of interest can be effectively increased. Within the Drude formalism, for example, the dielectric response of metal is controlled by its free electron, and the frequency-dependent dielectric constant of metal can be written as:

$$\varepsilon(\omega) = 1 - \frac{\omega_p^2}{\omega_r^2 + j\gamma\omega} \qquad 4.58$$

Where ω_p, is the plasma frequency measuring the strength of the interaction between the oscillators and the electric field, and ω_r, is the resonance frequency, γ is the damping constant

(absorption). We characterised the medium by the constitutive relation of $\boldsymbol{D} = \varepsilon_o \boldsymbol{E} + \boldsymbol{P} = \varepsilon_o \varepsilon \boldsymbol{E}$, and $\boldsymbol{P}$ is an optical medium defined by Maxwell. Under the consideration of an electric field on a dispersive and absorbing medium, the wave equation of the electric polarised can be stated as

$$\frac{\partial^2 \boldsymbol{P}}{\partial t^2} + \gamma \frac{\partial \boldsymbol{P}}{\partial t} + \omega_r^2 \boldsymbol{P} = \varepsilon_o \omega_p^2 \boldsymbol{E} \qquad 4.59$$

According to the Lorentz model, when $\omega_r = 0,$ the above model is reduced to the Drude model. It is the most used model for describing the permittivity of realistic dispersive materials such as conventional dielectric media, metals, etc. Similarly, in the presence of an oscillating magnetic field, the equation of wave of the magnetic polarisation can be defined as:

$$\frac{\partial^2 \boldsymbol{M}}{\partial t^2} + \gamma \frac{\partial \boldsymbol{M}}{\partial t} + \omega_r^2 \boldsymbol{M} = \mu_o \omega_p^2 \boldsymbol{H} \qquad 4.60$$

As we explained in the literature, all other variables are independent of the optical medium under the accountability of Maxwell's equation. However, the M and P are defined as optical mediums. Because the behaviour of light interaction in the medium is determined by M and P response to the light field, then the relative magnetic permeability $\mu(\omega)$, can be stated in the form of:

$$\mu(\omega) = 1 - \frac{\omega_p^2}{\omega_r{}^2 + j\gamma\omega} \qquad 4.61$$

4.5   Thermal Emission Properties

Some materials have been successfully used to design thermal light sources with unprecedented abilities. For example, directionality or monochromaticity contrasts with the ordinary incandescent light bulbs following Planck's law (Greffet et al., 2002b, Liu et al., 2011a, Greffet, 2011, Costantini et al., 2015b). A thermal radiation source, such as a blackbody or an incandescent filament of a light bulb, is regularly omnidirectional and broadband in nature, in contrast to a laser, which is temporally and spatially coherent.

We investigated a different way to control and manipulate the thermal emission spectrum based on plasmonic metamaterial. In the first steps, we focussed on realizing temporally and spatially coherent thermal sources with emission over the angular range, including its intensity, spectral and polarisation, depending not only on the temperature of the emitter but also on its optical properties. The physical mechanism behind this approach is not only based on the excitation

of surface modes or absorption resonances, but we also considered both passive and active excitation surface modes. The theory of thermal emission control in this thesis is based on Kirchhoff's law of thermal radiation.

Studying plasmonic behaviour within the visible to infrared range of the electromagnetic spectrum, including metamaterials, can view an understandable relation between plasmonic and metamaterials. The connection of these fields was stated via the concept of James Clerk Maxwell's equation (refer to chapter 2 of this thesis). We combined plasmonic (such as plasmonic material) and metamaterial as plasmonic metamaterials (PMMs) to design and engineer the materials index of the nanostructure. Since plasmonic resonances determine the optical properties of metamaterial, we apply Snell's law to relate the index of different material boundaries due to the fast propagation of light through the material that can change velocity and direction within other media, as illustrated in Figures 4.13 and 4.14 in this thesis for P and S-polarised. When the light enters from n_a ε_a to n_b ε_b, interface, the results at the boundary interface, some of the light is reflected away, some absorbed, and some transmitted inside the material. Since we deal with surface plasmon mode, we considered absorption rather than reflection and transmission, which occur at the interface due to the magnitude of the interaction between light and material. We modified that process via Kirchhoff's law of thermal radiation (Inoue et al., 2015) by neglecting the transmission throughout the PMM structures. Therefore, the absorption can be described as:

$$A(\lambda, \theta) = \epsilon(\lambda, \theta) = 1 - R(\lambda, \theta) - T(\lambda, \theta) \qquad 4.62$$

Where A is the material's absorptivity, and R and T are the reflectivity and transmissivity of the surface, all the above depend not only on wavelength but also the angle of incidence. The 3D finite-difference time-domain (FDTD) method is utilised to design and optimize the proposed PMMs. The refractive index of all materials is taken from experimental data of this reference (Palik, 1998). Furthermore, Thermal emission is a process that occurs in addition to absorption and $\epsilon(\lambda, \theta, T)$ reported from equation 4.62 the same as $A(\omega)$, therefore, the emissivity defined as the ratio of spectral radiance of the thermal emission from an object to that of a black body:

$$\epsilon(\lambda, T) = \frac{L_e(\lambda, T)}{L_{bb}(\lambda, T)} \qquad 4.63$$

Where the $L_e(\lambda, T)$ is the spectral radiance defined as the emitted optical power per unit area, solid angle, and per unit frequency at frequency ω or wavelength λ. $L_{bb}(\lambda, T)$ is the theoretical emittance of a blackbody according to Planck's law (Makhsiyan et al., 2015), and described as:

$$L_{bb}(\lambda, T) = \frac{2\pi hc^2}{\lambda^5} \frac{1}{\exp hc/\lambda KT_{-1}}$$
4.64

Where h is Planck's constant, λ is the wavelength of the emitted light, T is the object's temperature, c is the speed of light in a vacuum, and K is the Boltzmann constant. The thermal emittance $E_s(\lambda, T)$ from the surface of a heated object is given in W-m^{-3}, by Planck's law of thermal radiation:

$$E_s(\lambda, T) = (\lambda, T) \, L_{bb}(\lambda, T),$$
4.65

4.6 Material Stacked Arrangement

We consider the metal material as silver, accompanied by two dielectric materials: TiO2 with a refractive index of 2.13 and SiO2 with a refractive index of 1.46 as illustrate in Figure 4.16. The periodic geometric parameters were used in conjunction with PML absorbing boundaries along the z-minimum and z-maximum. These PML absorbing boundary conditions are specifically engineered to minimize reflections by efficiently absorbing incident light. They are implemented as absorbing materials that are impedance-matched to the surrounding materials, further reducing reflections. When using periodic boundary conditions, it is important to understand the need for systematic reliability across the entire system, which includes both the physical structure and the EM fields. This methodical approach allows for the calculation of the entire system's response while only considering one unit cell.

PSGs design arrangement
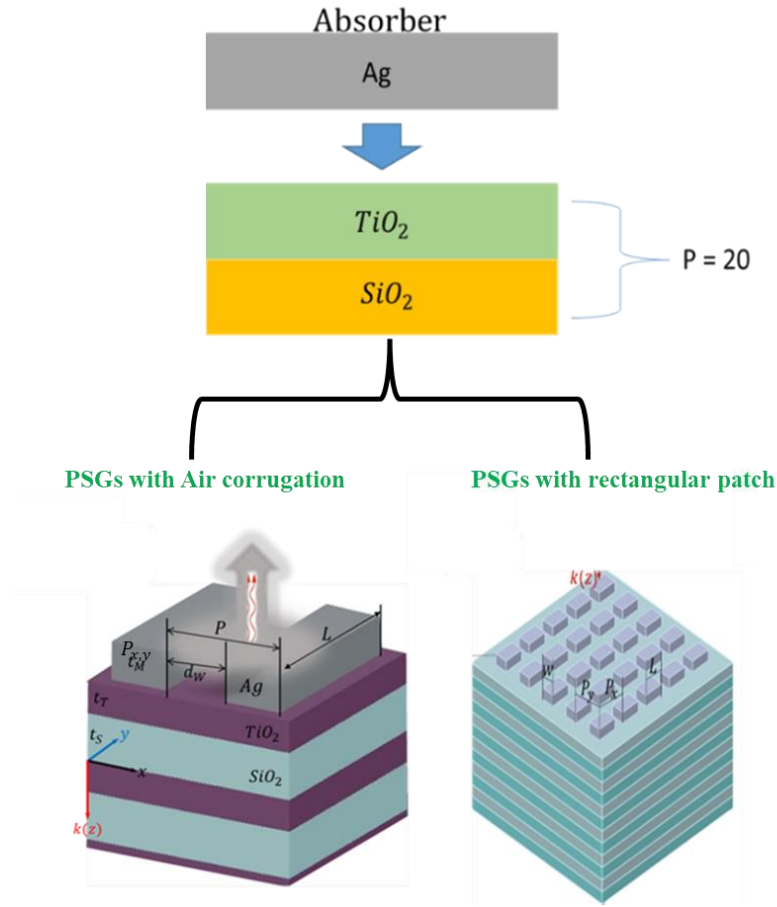
Figure 4.16: provides a schematic design arrangement of PSG structure including modelling simulation samples.

Regarding phase difference, we used the Bloch boundary along the *x* and *y* axes. The dispersion of the Bragg grating is calculated where k is the Bloch pseudo-wave vector and Λ_b, is BG, period. It is well known that the Bragg gating bandgap appears at the region of $k\Lambda_b/\pi = 1$, and the incident light at wavelengths in the region is reflected. A similar approach was used in the case of the Figure 4.17 structure, though it differed from the design arrangement we initially illustrated.

PIRAs design arrangement
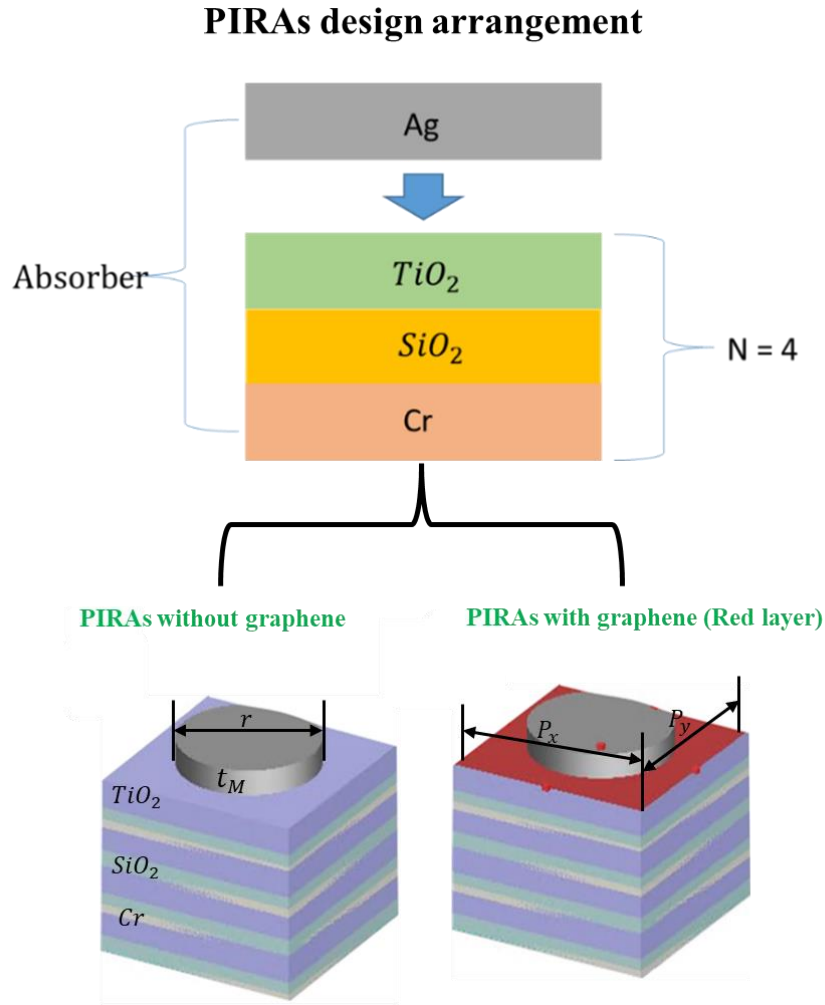
Figure 4.17: provides a schematic design arrangement of PIRA structure including modelling simulation samples.

4.6 Conclusion

We have demonstrated the simulation procedure based on the Lumerical Method analysis. The material information presented in this study, used in designing plasmonic metamaterials, enabled us to obtain accurate simulation results. We explained the structural analysis and theoretical calculations of reflection and transmission based on electric and magnetic fields, explaining some of the resultant findings. This chapter delineated a classical technique for plasmon resonance guidance in 3D Lumerical FDTD simulation, and the analysis script was included in the Appendix section. We considered various boundary conditions, encompassing periodic and Bloch. Furthermore, we investigated the thermal emission properties in different ways to control and manipulate the thermal emission spectrum based on plasmonic metamaterials.

Chapter 5
Plasmonic Stacked Grating Results and Discussion

This chapter will present simulation investigation results of the plasmonic stacked grating structure (PSGs). The spatial properties of emissivity are considered a key success following Kirchhoff's Law of Thermal Radiation. We introduce a helpful framework to understand some physical phenomena that drive thermal emission in 3D periodic structures and emphasise phenomenology and physical intuition through the details of Lumerical calculations as described in the previous chapter. We would look at periodicity, which plays a crucial role in determining the types of physical phenomena that can be excited in plasmonic metamaterials.

Disclaimer

The results and some of the material presented in this chapter were previously published in a journal article (Abubakar et al., 2021). The author of this thesis is also the first author of the publications. The publisher permits academic reuse as well as the creation of derivative works.

5.1   Plasmonic Stacked Grating Structure (PSGs)

We present a thermal radiation design based on plasmonic metamaterials. The structure comprises metallic elements and a Bragg grating, as depicted in Figure 5.1. This design demonstration consists of a two-dimensional (2D) metallic nanostructure and a one-dimensional (1D) dielectric Bragg Grating (BG). A 2D metallic nanostructure with a thickness rest on top of a 1D-BG arranged in z direction. The BG comprises two alternately arranged dielectric materials with thicknesses and refractive indices, respectively. The total number of grating periods in the BG is denoted as P. The metallic nanostructures have consisted of periodic silver patches with pitches of Px and Py along x and y directions. Each silver patch has a height of a width of W, and a length of L.
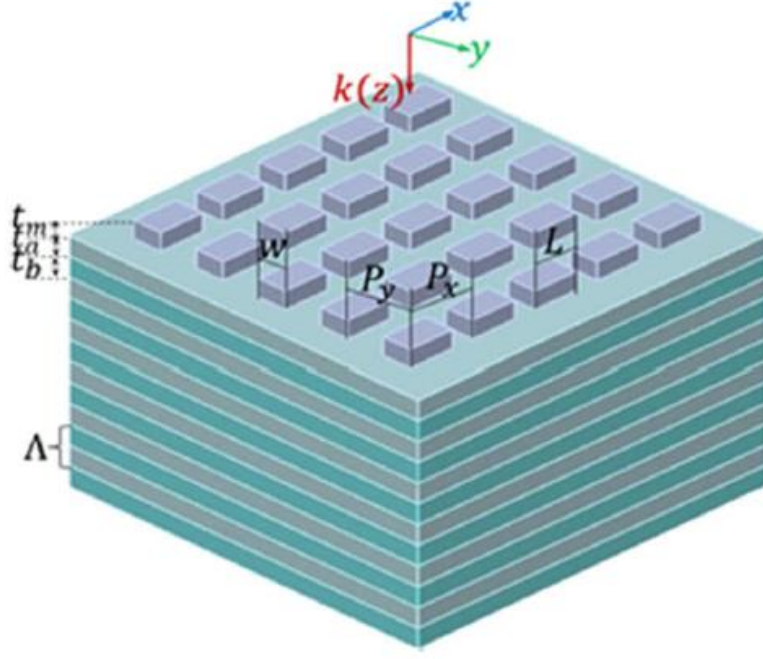
Figure 5.1: (a) A schematic diagram of the proposed PSGs composed of 2D metallic Nanostructured Surface and 1D BG that contains alternative TiO₂ and SiO₂ thin films with a period of Λ.

5.2   Coherent Thermal Emission on PSGs

Coherent thermal emission based on PSGs involves dielectric materials within the BG structure, which consists of TiO2 and SiO2. The proposed PSGs were designed and optimized using the finite-difference time-domain (FDTD) method in three dimensions. The refraction index of the dielectric materials was determined using experimental data (Palik, 1998). The interaction between the metallic grating and the BG in this configuration leads to impedance matching at wavelengths within the photonic band gap. This allows the structure to exhibit high emissivity with a narrow spectrum and to shape angular responses in the infrared regime. Additionally, the combination of the metallic grating and the BG results in high reflectivity for light. Figure 5.2 displays the calculated spectrum of the PSGs. It is evident that a significant resonant dip occurs at a wavelength of 3.86 μm in the reflection spectrum, resulting in a narrow-band peak with emissivity as high as 99% in the emissivity spectrum.
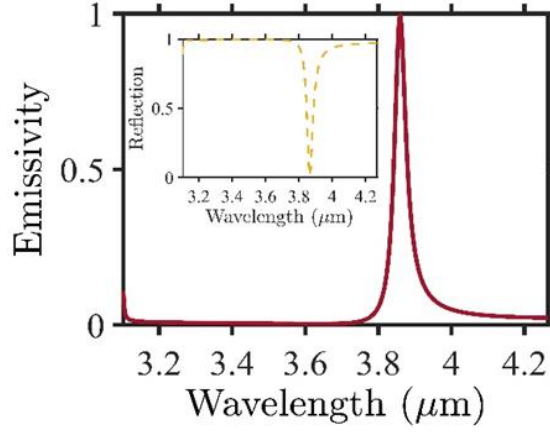
Figure 5.2: Emissivity and reflectivity spectrum of the PSBs under normal incidence at TM polarisation.

5.2.1 Polarisation Mode on PSGs

The physical mechanism of the emergence of the strong and sharp resonance originates from the fact that when a plane wave is impinging on the PSGs along the *z* direction, the 2D silver nanostructure of the PSG can be equivalently described as a homogeneous slab with frequency-dependent permittivity and permeability (Gong et al., 2013b). We neglected the transmission, as we stated in Chapter 4, at all the PSG wavelengths due to the existence of a photonic bandgap enabled by the dielectric materials of the BG. To get more insight into the behaviours of the sharp and strong emissivity, we considered and obtained the emissivity spectra for both TE- and TM-polarised light and the reflection and transmission spectra of the BG, as depicted in Figure 5.3(a) and (b). The proposed PSGs support polarisation-dependent thermal radiation, which is desirable for various potential applications such as polarisation-assisted thermal encryption (Makhsiyan et al., 2015). We note that the emissivity peaks for both polarisations always appear within the BG bandgap.
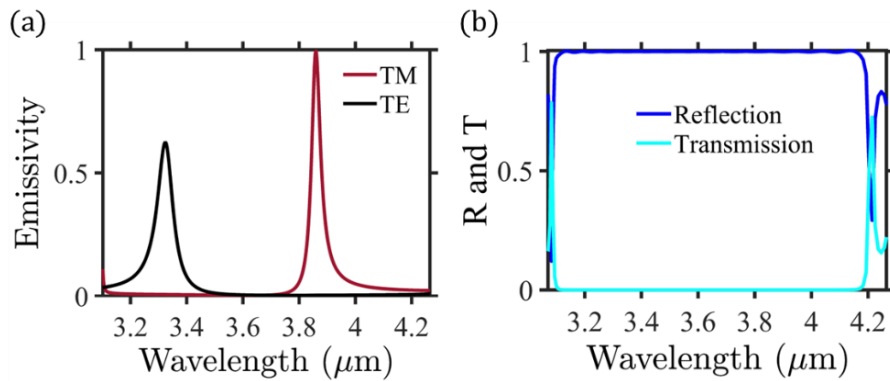
Figure 5.3: Polarisation-dependent optical characteristics of the PSGs. (a) Emissivity spectra of the PSGs under TE- and TM-polarised incidence of light, respectively. (b) The reflectivity and transmissivity spectra of the BG.

The absorption resonance peak in Figure 5.3(a) for the TE mode is restricted due to the system's mirror symmetry in a plane perpendicular to x and y and performed a lower emission peak at the photonic bandgap of the 1D-BG. However, the modes of the system can be separated into transverse electric (TE) and transverse magnetic (TM) modes for the mirror plane due to the system's mirror symmetry in a plane perpendicular to x and y.

Furthermore, the $|E|^2$ field distribution of the PSGs at resonant wavelengths is plotted in Figure 5.4 (a)-(d). It indicates that light is strongly localised and absorbed near the corners of the metallic nanoparticles (Figure. 5.4(a) and (b)), and there is no transmission of light through PSGs (Figure. 5.4(c) and (d) observation). Design parameters are $P_x = P_y = 1.63$ μm, $L = 1.1$ μm, $w = 0.7$ μm, $t_m = 0.05$ μm, $t_a = 0.38$ μm, $t_b = 0.65$ μm, and $P = 20$. For both TE- and TM-polarised incidence of light, the electric fields oscillate along the x and y directions, respectively.
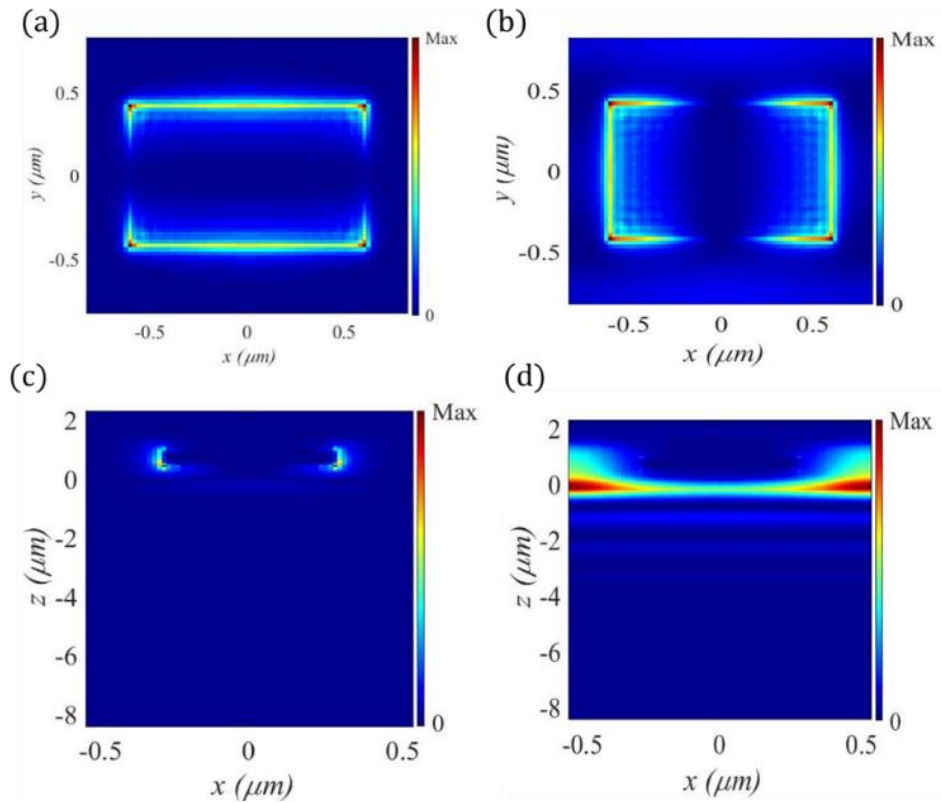
Figure 5.4: Field distribution $|E|^2$ of the PSGs in the central plane (i.e., x-y plane) of the metallic nanostructure at a resonant wavelength of 3.32 μm for the TE-polarised light (a) and a resonant wavelength of 3.86 μm for the TM-polarised light (b). Field distribution $|E|^2$ of the PSGs in the x-z plane of the metallic nanostructure at a resonant wavelength of 3.32 μm for TE-polarised light (c) also, resonant wavelength of 3.86 μm for TM-polarised light (d).

5.3 Concept and Optical Characteristics

The schematic PSG structure, illustrated in Figure 5.1, depicts the thickness of the 2D metallic nanostructure as denoted by t_m,. The refractive indices thicknesses of the composed dielectric materials are given as n_a and n_b,. The metallic nanostructures have consisted of periodic silver patches, along x and y directions, each silver patch has a height of t_m, a width of W, and a length of L.

The relationship between the resonant peaks and the structural parameters of t_m, t_a, t_b, and P_x, P_y, based on observation, the resonant wavelength of the PSGs shifts when P_x, P_y, rises from 1.63 to 2.03 μm, and the emission peak becomes smaller when the grating period becomes more significant than 1.8 μm. The emission wavelength is slightly tunable by varying the BG period, as shown in Figures 5.5 (a) and (b). We observed that the thickness of TiO$_2$ (t_a) and SiO$_2$ (t_b) Layers in the Bragg gratings play a crucial role in the emission peak and emission wavelength. Especially when t_a, thickness varying from 0.33 to 0.43 μm, the emission peak is slightly dropped to $\sim$ 80% when the thickness reaches 0.4 μm. The BG bandgap position reacts according to the Bragg condition, and the emission wavelength shifted linearly from $\sim$ 3.6 to 4.0 μm. However, when t_b, thickness varies from 0.55 to 0.75 μm, the BG bandgap position varies according to the Bragg condition as we stated before, and this Bragg condition can be stated as $\lambda_{Bragg} = 2(t_a n_a + t_a n_b)$. In this case, of t_b, the intensity of the emission peak is not affected by the thickness, but only the emission wavelength shifted linearly from $\sim$ 3.8 to 4.1 μm and slightly narrowed from 0.55 μm, as shown in Figure 5.5 (b). The dependence of light emissivity on the thickness of the silver film t_m , is shown in Figure 5.4 (d). As t_m, increases, the resonant wavelength of the PSGs shifts when the thickness increases from 0.05 to 1 μm. However, the TiO$_2$ thickness (t_a) in Figure 5.5 (a) illustrates the resonant peak decreases in intensity when the thickness is more significant than 0.4 μm, and the emission wavelength also varies with the increase or decrease in this thickness.
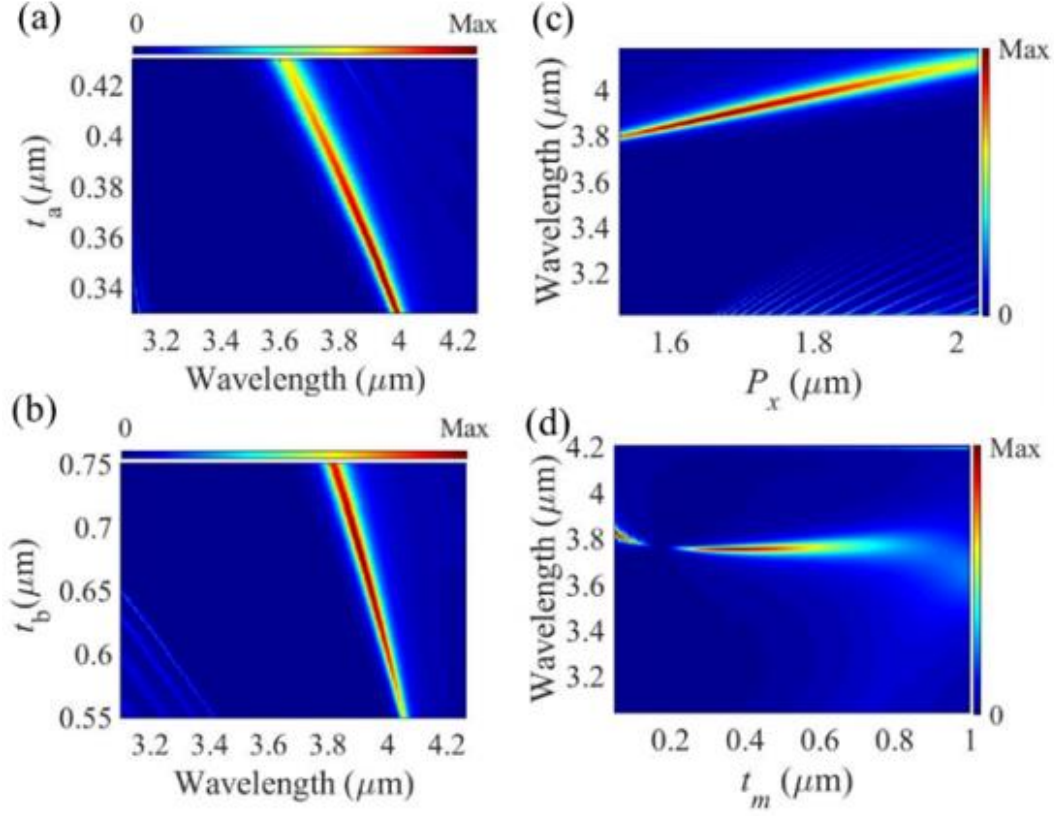
Figure 5.5: Evolution of the emissivity spectra to the structure parameters of the PSGs. (a) Dependence of the emissivity spectra on the thickness of TiO_2 (b) Dependence of the emissivity spectra on the thickness of SiO_2 (c) Dependence of the emissivity spectra on the pitch length (L) (d) Dependence of the emissivity spectra on the thickness of the silver film.

The dependence of transmission and emission of the PSGs at $P = 5$, 10, and 15 are investigated and demonstrated in Figure 5.6(a) and (b), respectively. Consequently, the total number of grating periods would affect the impedance matching condition, causing more transmission through the stacked gratings only when the number of grating periods of the stack is less than 15. In our case in Figure 5.6 (a), when we use a period stack of $P \leq 15$, there is minimal transmission, and it does not affect the emission wavelength, only the emission intensity. When P is less than 15, transmission components within the structure are observed, causing less emissivity of the proposed PSG structure. Therefore, increasing P leads to reduced light transmission and emission intensity increase.
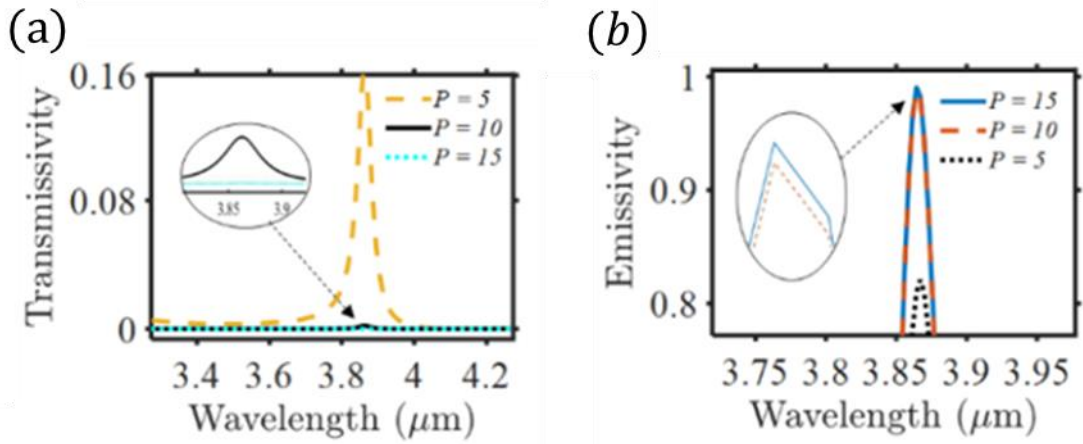
Figure 5.6: Transmissibity (a) and emissivity (b) at P = 5, 10, 15, when $P_x = P_y = 1.63\ \mu m$, $L = 1.1\ \mu m$, $w = 0.7\ \mu m$, $t_m = 0.05\ \mu m$, $t_a = 0.38\ \mu m$, and $t_b = 0.65\ \mu m$.

5.4   Angular and tunability properties of the PSGs

We used PSG structure to achieve tunable plasmon resonance. Plasmon resonances are electromagnetic modes associated with the excitation of collective oscillations of the electron's charge density in metals. They combine high-field intensities with frequency or wavelength selectivity that could be used for new photonic devices. Two plasmon resonances need to be understood: surface plasmon polariton (SPP) propagating along a metal-dielectric interface and localised surface plasmon (LSP) modes confined to subwavelength metallic objects. The strong optical fields produced can be used to improve applications at specific wavelengths.

Attributing to the PSGs' unique property of the emission peak always being located within the band gap of the BG, the FWHM of the PSGs can be flexibly tuned and significantly narrowed by decreasing the BG band gap, such as by minimizing the refractive index difference of the BG. According to our observations, the emission peak is always located in the BG bandgap. Therefore, when the BG bandgap is narrower, the FWHM of the resonant peak would be smaller. Narrowing the BG bandgap relies on minimizing the refractive index difference of the BG (Gong et al., 2013b).

Another intriguing property of the PSGs is spatial directivity. We investigate this property by calculating emissions from a different angle. Figures 5.7 (a) and (b) illustrate the dependence of the resonant peaks on the radiation angles from 5 deg to 20 deg. The resonant peaks' wavelength varies significantly with the angle, and the angle bandwidth is quite narrow. As a result, we can observe the emission of a single wavelength only in a certain direction. To put it simply, the resonant emission of the proposed PSGs is highly directional. The behaviour's

physical origin arises from the emission wavelengths appearing in the BG band gap, which is sensitive to the incidence angle, as shown in Figure 5.7.
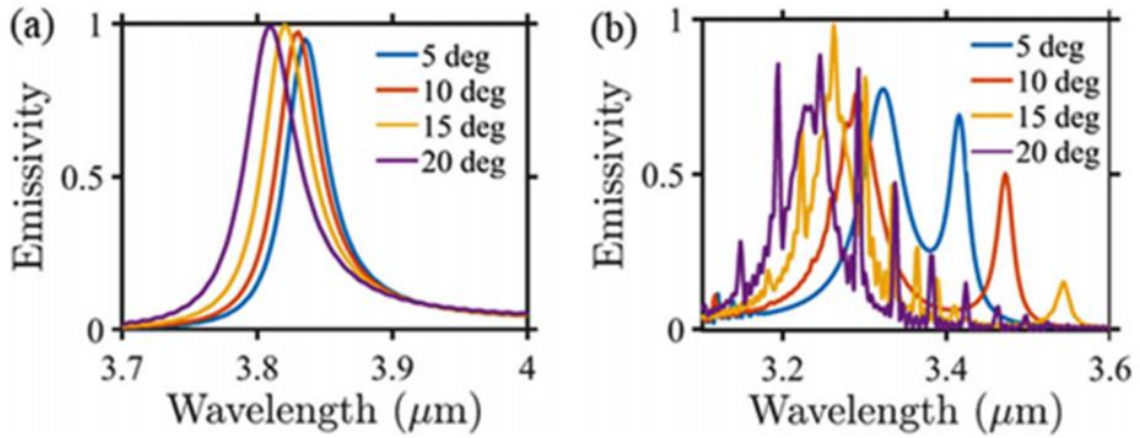
Figure 5.7: Angular response of the PSGs. Dependence of the emissivity spectra on the radiation angle for TM-polarised (a) and TE-polarised light (b), respectively.

We also demonstrate the flexible tuning of resonance peaks by adjusting the structural parameters. For instance, varying the width of the metallic patch along the y-axis, W, from 0.3 μm to 0.7 μm, results in a shift of the emissivity peak wavelength from 3.86 to 4.10 μm for TM-polarised light and from 3.32 μm to 3.15 μm for TE-polarised light, as depicted in Figures 5.8(a) and (b). In Figure 5.8(b), the dashed line indicates the photonic boundary limitation in the spectrum, distinguishing the area with zero transmission (on the right) from the region with non-zero transmission (on the left) due to polarisation changes.
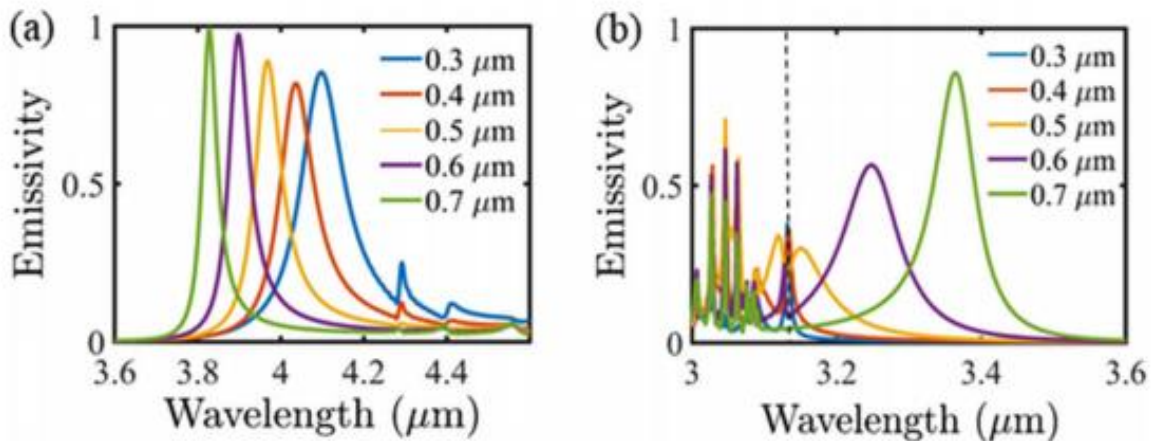
Figure 5.8: Tailoring thermal radiation of TM- (a) a TE-polarised light (b) by tuning geometric parameter w from 0.3 μm to 0.7 μm.

5.5   Periodic Tunable Plasmonic Metamaterials

A tunable plasmonic metamaterial for mid-infrared applications has been reported. The proposed PSGs require narrowband absorption spectra within the mid-infrared range, which was achieved using plasmonic field enhancement and near-field coupling. This allows the resonant wavelength of a potential application to be tuned. Plasmonic narrowband absorbers based on periodic resonators on metamaterials have resulted in outstanding applications. Surface plasmons, which denote resonant oscillations of free conducting electrons stimulated by electromagnetic radiation at the metal and dielectric interface, physically change in response to modifications in the refractive index of the surrounding medium. The high surface sensitivity of plasmonic absorbers, coupled with their free process electrons and fast real-time response, renders them well-suited for sensing, imaging, and energy harvesting devices. This technology has garnered significant attention for its design and development in the visible and near-infrared wavelengths. Therefore, we used plasmonic material to design and fabricate a coherent thermal light source based on plasmonic metamaterial absorber. The nanocomposite exhibits an average absorbance of 98% across the spectrum for both PSG designs. Our simulation results, illustrated in Figure 5.9, demonstrate that the absorption peak of the PSGs can be tuned by varying the thickness and Bragg grating period. Modulating that period provides a straightforward method to effectively adjust the operating wavelength of the PSGs.
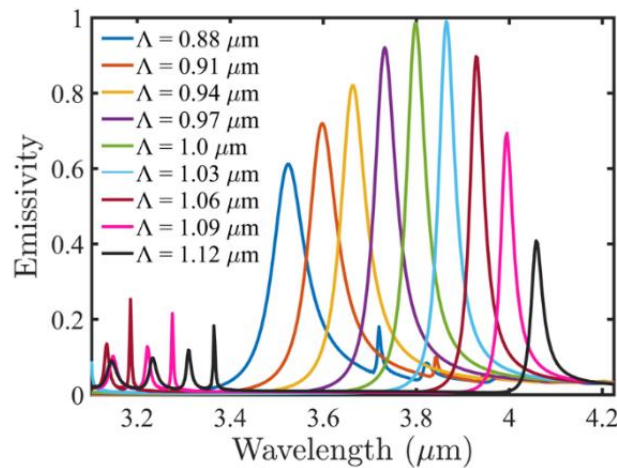
Figure 5.9: tunable absorption based on 1D-BG periods.

As a result of the sensitivity of surface plasmons to one-dimensional Bragg grating (1D-BG) changes, a shift in the resonant wavelengths of the absorption characteristics is obtained. The use of near-field enhancement on the surface of the PSGs improves sensitivity by intensifying the interaction between surface waves and analyte molecules. As illustrated in

Figure 5.9, increasing the 1D-BG period from 0.88 to 1.12 μm leads to significant shifts in the absorption wavelengths, causing a reduction in the intensity of the emitted light at specific wavelengths.

5.6 Plasmonic Stacked Grating structure with Air Slit

Disclaimer

Some of the results presented in this section were accepted as a poster publication in the CLEO/Europe-EQEC Conference 2019 in Munich, Germany, during the World of Photonics Congress. Title: *Novel Mid-infrared Multiple Coherent Emissions for Gas Sensing*.

We introduce another designed structure based on a 3D simulation illustrated in Figure 5.10. This proposal requires a 2D metasurface pattern on top of dielectric periodic layers. Plasmonic structure based on 2D metasurface attracts significant attention for tailoring an electromagnetic response across several spectral ranges. We demonstrate the metallic pattern with a narrow air slit on top of Bragg grating acts like a homogenous slap with large permittivity and small permeability. In this work, the design and simulation of the novel structure are to achieve multi-emission spectra by varying some of the parameters of the metallic pattern and Bragg grating period. The parameters include metallic thickness t_M, Bragg grating t_T, and t_S, and the length of the metallic patching L.
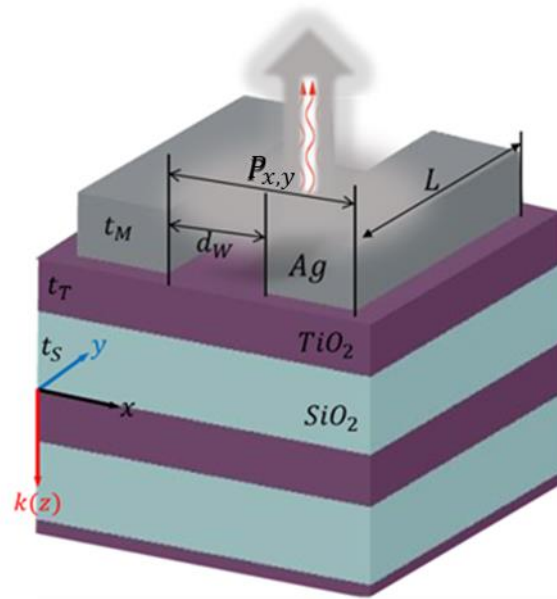
Figure 5.10: representation sample of pairing a metallic grating and a Bragg grating with an air slit at the middle for wavelength emission, patterned as 3D gratings of periodicity P_x and P_y,

5.6.1 Plasmonic Stacked Grating Structure with Air Slit

The proposed plasmonic stacked gratings (PSGs) feature a configuration with narrow air slits that enable thermal emission with an ultra-narrow spectrum. These PSGs comprise a metallic pattern and a Bragg grating. The schematic design of the PSGs is illustrated in Figure 5.10, which demonstrates a metallic film of thickness t_M corrugated by narrow air slits of width d_W and period along P_x and P_y. This metallic layer rests on top of Bragg grating dielectric layers with thicknesses t_T and t_S, and refractive indices n_a and n_b derived from experimental data (Palik, 1998). The PSG structure has the capability to emit light within a narrow angular range and effectively tune its operating wavelength. Controlling the Bragg grating band gap allows for significant narrowing and adjustment of the emission spectrum's half-width at half-maximum (FWHM). Figure 5.11 illustrates the coherent thermal emission from the proposed PSGs in both TE and TM polarisations using an air-corrugated design.
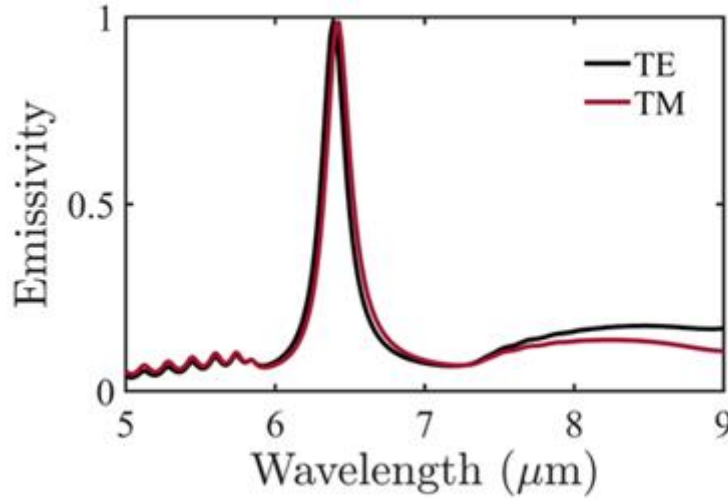
Figure 5.11: Emission spectrum for different geometric calculations on the metallic grating TE and TM.

Table 5.1: Design parameters

Materials	Thickness
Silicon dioxide (SiO$_2$) layer	Vary: 830 - 1270 nanometres (nm)
Titanium dioxide (TiO$_2$) layer	Vary: 460 - 670 nanometres (nm)
Bragg grating period (P)	20
Plasmonic Absorber (silver (Ag))	Vary: 400 – 1600 nanometres (nm)
Air Corrugation (d$_W$)	50 nanometres (nm)

Following Planck's law, the metasurfaces achieved thermal emissions with unprecedented capabilities compared to traditional incandescent light bulbs. Exposed metallic resonators with subwavelength dimensions exhibit total absorption A(λ) when light reflection fades, and absorption occurs due to the resonant excitation of surface plasmon polaritons (SPPs). This concept can significantly enhance thermal emission at the resonant frequency with a spectrum much narrower than that of a blackbody at the same temperature (Zhu et al., 2013). Using metasurface, we can control the absorption spectrum A(λ) by shaping through metallic resonators of different sizes within the same subwavelength period. This shaping can achieve the frequency comb in mid-infrared if we carefully choose the metal stack arrays.

The ability of nanoplasmonic structures to tailor thermal emission at the mid-IR is of great opportunity for many applications, for example, thermophotovoltaics (Lin et al., 2003a, Basu et al., 2009, Narayanaswamy and Chen, 2003, Messina and Ben-Abdallah, 2013, Ilic et al., 2012), thermal imaging (De Wilde et al., 2006, Kittel et al., 2005), thermal circuits (Otey et al., 2010, Basu and Francoeur, 2011, Zhu et al., 2012), local heating (Wang and Wu, 2016), and cooling (Guha et al., 2012). A structure that generates narrowband thermal emission has reasonable consideration for thermophotovoltaic and thermal imaging applications.

5.6.2 Spectra Selectivity Coherent Thermal Emission

Based on Figure 5.10, we introduced the design of novel mid-IR multiple coherent emissions for gas sensing. The progress of this proposed design was presented during the World of Photonics Congress. We have engineered the structure up to the diffraction limit to ensure the achievement of tunable multiple coherent thermal emission spectra. Figure 5.12 displays the results for the multi-coherent thermal emission spectra achieved by adjusting the length (*L*) of

the plasmonic absorber and the width of the air slit (d_W), along with the dielectric period of two material stacks (t_T and t_S) and the thickness of the metallic absorber (t_M), including the periodic surface boundary (P) along x and y axes. The figure demonstrates variation in the length of the metallic absorber from 0.4 to 1.4 µm. The obtained results in Figure 5.12 (a) $d_W = 0.04$ µm and (b) $d_W = 0.06$ µm indicate that the intensity of the emission decreases with an increase in d_W, slightly affecting the emission wavelength as illustrated in Figure 5.12 (b).
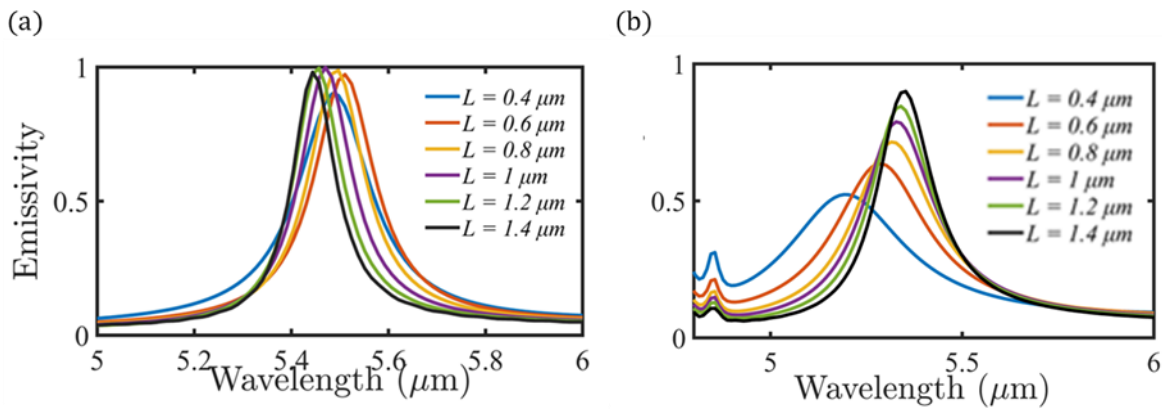
Figure 5.12: Tunable emission spectra based on metallic length and width from 0.4 µm to 1.4 µm. (a) the width of the metallic absorber $d_W = 0.04$ µm (b) the width of the metallic absorber $d_W = 0.06$ µm.

We also investigated the effective plasmon resonance based on the metallic thickness using the function of Bragg grating, as depicted in Figure 5.13. We applied a differential boundary condition along the P_x and P_y axes and observed that changing the thickness of the plasmonic resonator of the PSGs with an air-narrow slit can modify the resonance wavelength. Additionally, the peak intensity is slightly reduced when the thickness of the metallic resonator is below 0.8 µm, as illustrated in Figure 5.13 (b). In contrast, in Figure 5.13 (a), the peak intensity shows a slight increase upon reducing the metallic resonator thickness below 0.8 µm. Furthermore, the emission spectrum's Full Width at Half Maximum (FWHM) can be adjusted and significantly narrowed (to ~0.009 µm) by expanding the photonic limitation region of the boundary condition, as demonstrated in Figure 5.13 (a). By reducing the Bragg grating period from $\Lambda = 2.09$ µm to $\Lambda = 1.65$ µm and varying the thickness from 0.4 to 1.6 µm, we observed a shift in emission wavelength, as depicted in Figure 5.13 (c) and (d). The emission intensity behaviours corresponding to changes in thickness are plotted in Figure 5.13 (c) and (d).
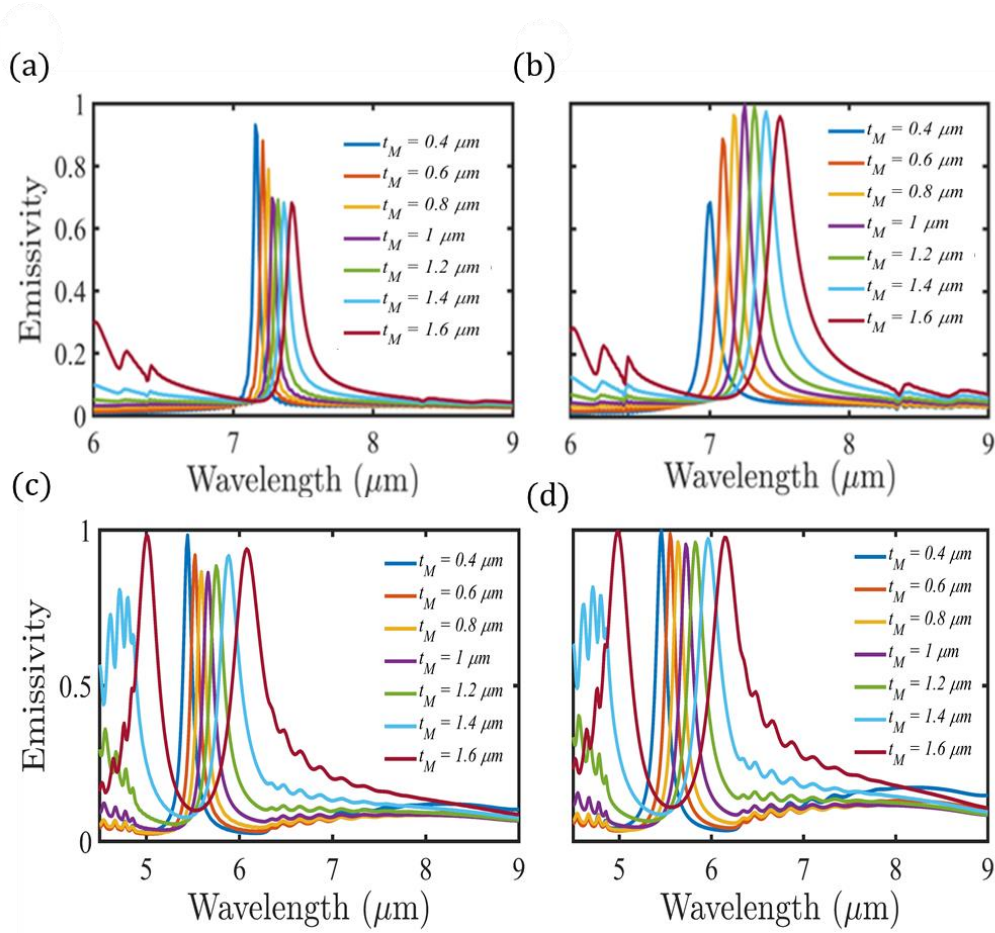
Figure 5.13: Demonstrate the emission spectrum for difference calculations on the metallic thickness from 0.4 to 1.6 µm, and boundary condition, (a) and (c)P_x = 1.3 µm, and P_y = 1.93µm, (b) and (d) P_x = 0.63 µm, and P_y = 1.93µm

Figures 5.14 (a) and (b) show the emission based on the thickness of TiO_2 (t_T) and SiO_2 (t_S) layers in the Bragg grating materials stack arrangement. The spectrum of the single emission wavelength can be shifted by varying the thickness of the Bragg grating period. The emission peak and wavelength exhibit extraordinary behaviour by keeping the emission intensity nearly constant, as shown in the figure. We discovered that the Bragg grating bandgap position varies with the Bragg condition, and the emission wavelength varies with the bandgap position and shifts linearly. The dependence emissivity of Figure 5.14 (a) is obtained by holding the TiO_2 thickness t_T constant while varying the SiO_2 thickness t_S from 0.99 to 1.29 µm. In Figure 5.14 (b), we did the same with TiO_2, varying the thickness t_T from 0.46 to 0.86 µm while keeping the SiO_2 thickness t_T constant.
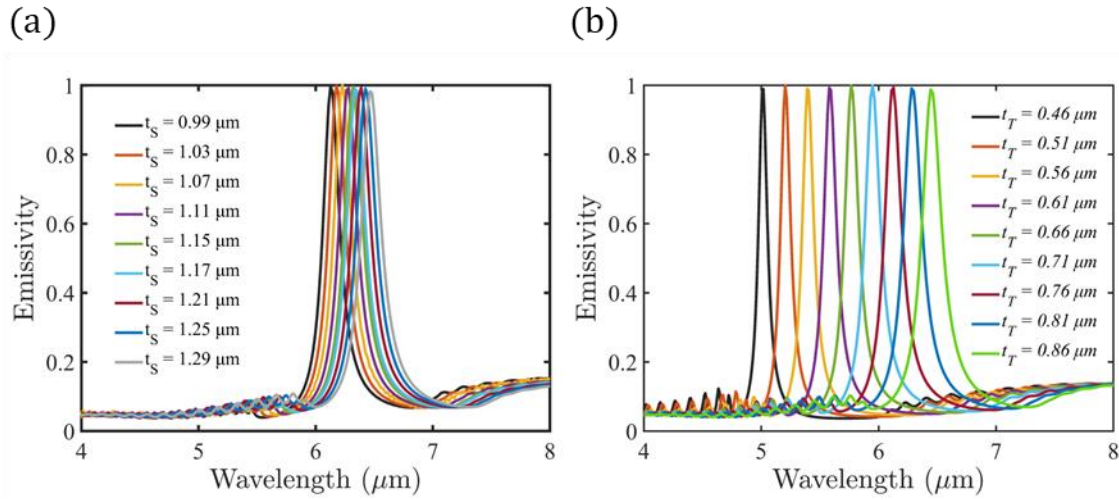
Figure 5.12: Tunable emission spectrum based on the thickness of the dielectric material (a) SiO$_2$ and (b) TiO$_2$.

5.6.3   Angular and tunability thermal coherent emissions

The computed spectrum emission at various incidence angles ranging from 5 to 60 degrees is shown in Figure 5.15. Within the bandwidth of wide incidence angles, the emission light is ultra-narrow. The incidence angle causes the resonant peaks to change significantly, and the angle bandwidth is quite narrow. This type of resonant emission is highly directed and angle-dependent.
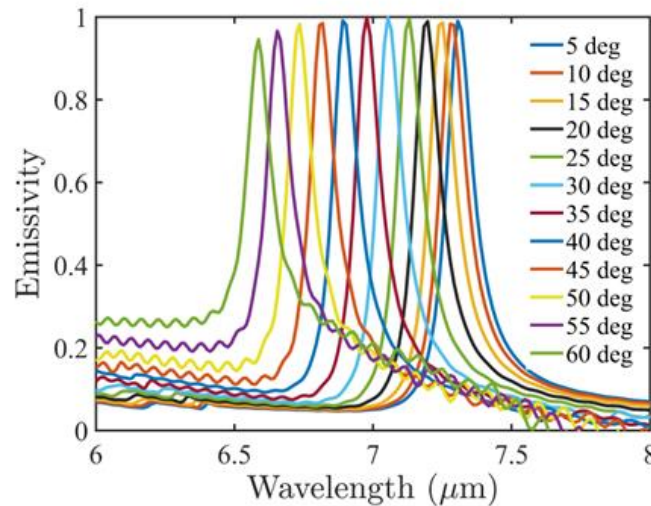
Figure 5.13: Tunable emission spectrum for difference angle of incidence

Figure 5.16 depicts the emissivity based on periodic adjustments to the boundary conditions. It indicates that the periodic boundary P does not affect the emission wavelength but only the peak intensity. The peak intensity drops by increasing P, and the FWHM of the emission

spectrum can be significantly narrowed by increasing P. Figure 5.16 (a) shows that at P = 0.63 µm, the emission is 99%, and the FWHM is significantly wide to ~0.12 µm. Figure 5.16 (b) shows that the intensity of emissions dropped to 93%, and the FWHM has become narrow as ~0.09 µm at P = 0.83 µm. Increasing the P to 0.93 µm compared to P = 0.83 µm, the FWHM is the same, but the intensity of the emission wavelength dropped to 84%. Similarly, P = 1.13 µm, the emission intensity decreased to 77%, and FWHM became narrow ~0.04 µm, as shown in Figure 5.16 (d).
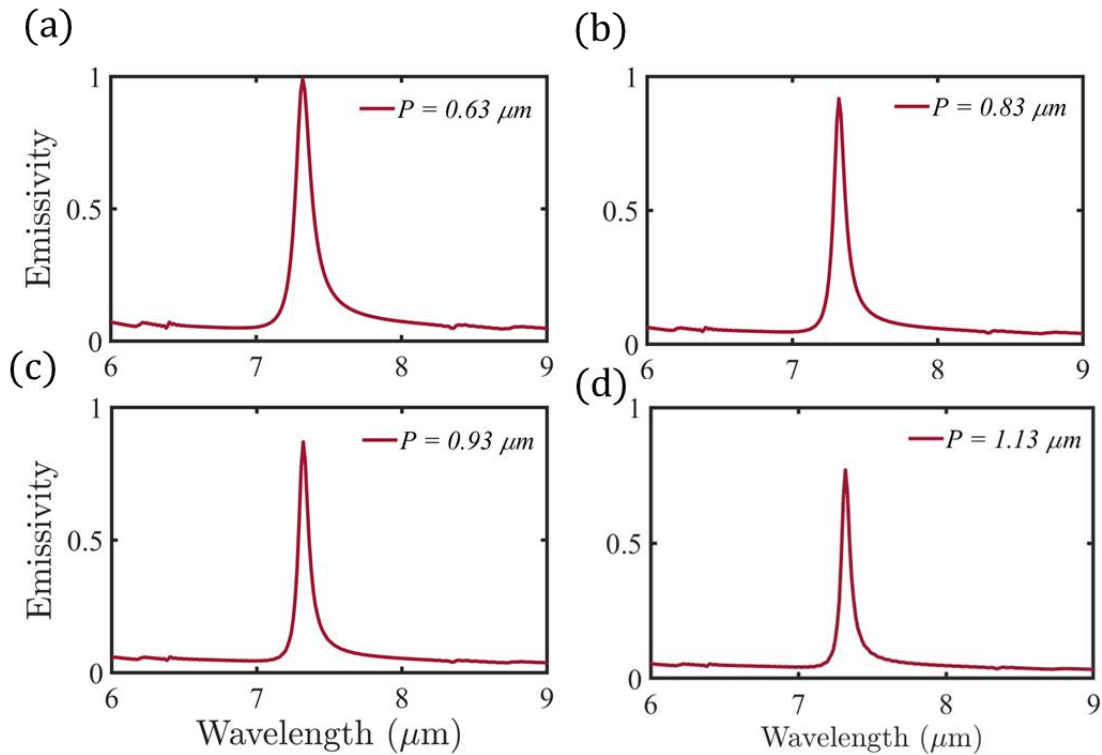
Figure 5.14: Emission spectrum based on different periodic boundaries. (a) the periodic boundaries P = 0.63 µm, (b) the periodic boundaries P = 0.83 µm, (c) the periodic boundaries P = 0.93 µm, (d) the periodic boundaries P = 1.13 µm

The dispersion of the Bragg grating combined with metallic grating can result in extremely high absorption within the photo bandgap area. The Bragg grating band gap appears in the region where reflection and transmission are absent, and absorption appears when z_{PMM_S} satisfy z_0 as shown in equation 4.23. Because of the metallic intervention with the Bragg grating, the resonance of the emissions spectrum can be controlled by varying the Bragg grating period, as shown in Figure 5.17, where Λ is the one-dimensional length covered by TiO_2 and SiO_2 as a Bragg grating period.
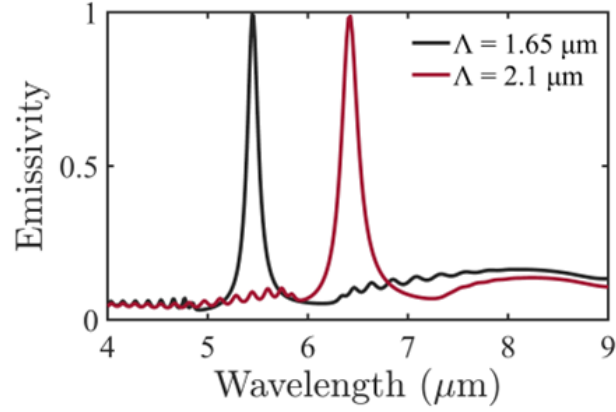
Figure 5.15: Tunable Bragg grating emissions.

The results in Figure 5.18 were obtained by adding a special dielectric layer (SDL) positioned between the interface of the Bragg grating and the conducting metal, enabling the achievement of multiwavelength emission. The SDL possesses a refractive index denoted as (n_s) and a thickness specified as DL. When the SD layer reaches a thickness of 10 µm, the emissivity spectrum, with the contribution of SDL, generates multiwavelength emission characterized by a narrow linewidth of approximately 0.006 µm, as illustrated in Figure 5.18 (a) and (c) for the TE and TM-modes, respectively. By increasing the thickness DL to 20 µm, we can achieve more multiwavelength emission spectrum as shown in Figure 5.18 (b) and (d)
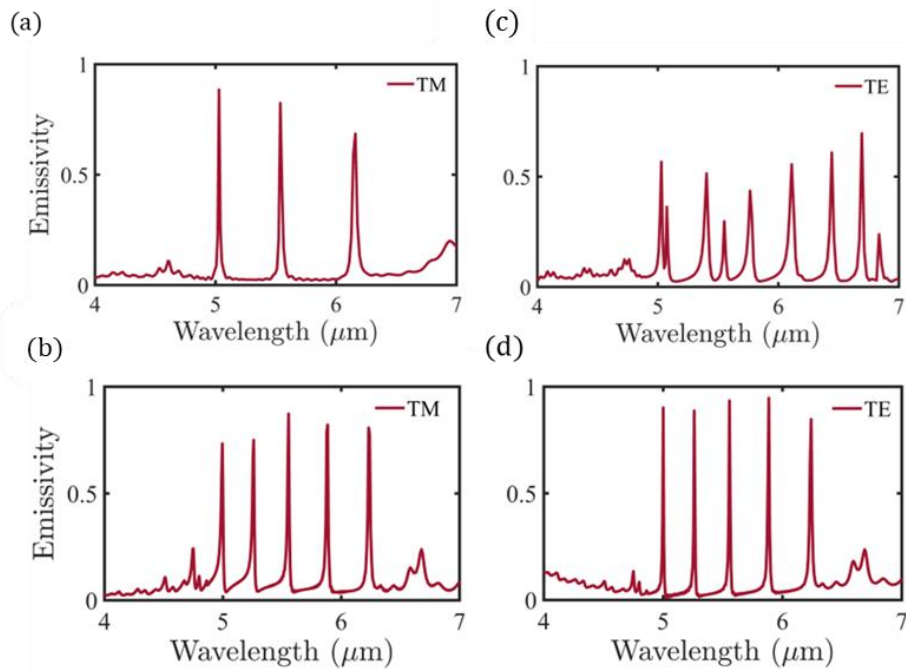
Figure 5.16: Emissivity spectra with a spacing layer SDL stacked in between metal and dielectric material (a) and (b) TM modes (c) and (d) TE modes of the emissivity spectrum.

Figure 5.19 illustrates the behaviour of electric and magnetic fields when a plane wave of transverse-magnetic (TM) polarisation, pointed along the z-direction along the z-direction, interacts with the PSG structure through the plasmonic resonator. The plasmonic resonator, controlled by air corrugations along the x-axis as demonstrated in equations 4.27 and 4.28, alters the electric and magnetic field behaviour within a region where impedance matching is satisfied. In this region, a decaying resonance acts as a homogeneous slab with a higher effective permittivity and a lower effective permeability. This photonic interface region of metallic, SDL, and Bragg grating acts as a mirror, reflecting some light out to free space and absorbing some due to impedance matching and decaying significantly into the spacing dielectric layer, followed by Bragg grating. These interfaces performed multi-emission wavelengths with the SDL at 5.03 μm, 5.54 μm, and 6.16 μm, as shown in Figure 5.19.
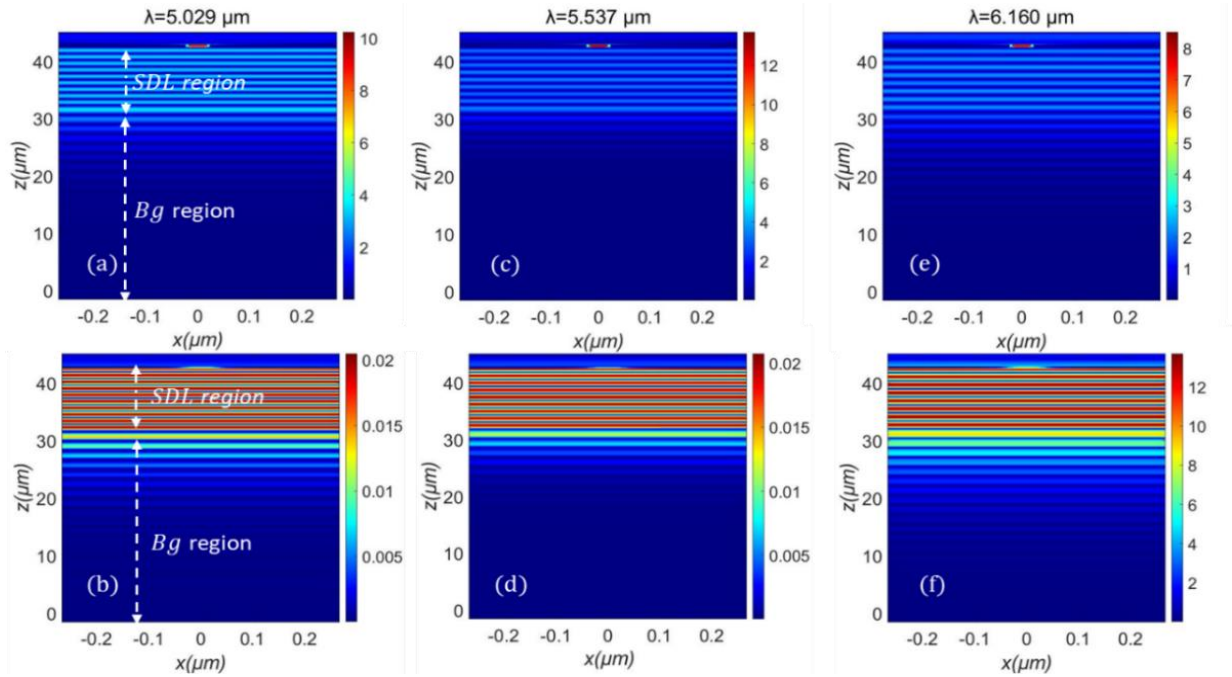
Figure 5.17: The time-averaged field distribution (a, b, c, d, e, f) is the field distribution between the metallic Spacing layer and Bragg grating at different emission wavelengths of the PSG structure.

Figure 5.20 demonstrates the reflected and transmitted surface, characterised by the electric field within the air slit. The effective index at the lowest mode inside the air slit depends on the function of the air slit (d_W) and the dielectric constant (ε_r) of the metal stack, and the mode of surface reflection and transmission is plotted in Figure 5.20 (a) and (b).

(a)   (b)
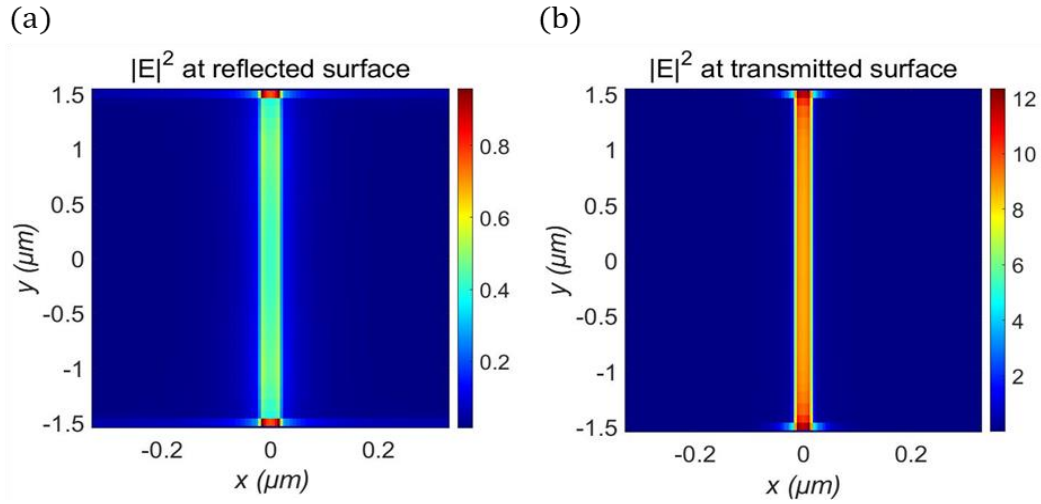
Figure 5.20: The electric field surface distribution of the PSG structure (a) |E|² at surface reflection and (b). |E|² at surface transmission.

5.7   Conclusion

We proposed the PSG structure to achieve both spatially and temporally coherent thermal emission in the mid-infrared range. FDTD and analytical calculations demonstrate that the rectangular metallic patching and metallic corrugation with air can interact with a Bragg grating. This interaction gives rise to emissions with intriguing properties: narrow emission light, tunable emission wavelength by adjusting the Bragg grating period, and significantly narrowed FWHM of the emission spectrum by reducing the Bragg grating band gap. We successfully achieved the intended goal of coherent thermal emission, as demonstrated in the chapter. The tunable emission wavelength was also attained by controlling the design parameters and the polarisation angle of the incident electromagnetic wave. A multi-wavelength coherent thermal emission with a narrow linewidth of about 0.006 μm was achieved within the 4 - 7 μm spectrum. These features open possibilities for a cost-effective and compact infrared source platform, in contrast to traditional semiconductor sources like light-emitting diodes or quantum cascade lasers. Due to their tunable and ultranarrow absorption (reflection) spectrum, PSGs may also serve as promising candidates for other applications such as biosensing, photodetection, and thermal-photovoltaic power generation.

Chapter 6
Plasmonic Infrared Absorber Structure Results and Discussion

Graphene is a 2D material consisting of a monolayer of carbon atoms. It provides unique properties, such as optical transparency, flexibility, high electron mobility and conductivity, which can be tuned by electrochemical potential through optical excitation. The characteristics of graphene in the infrared region and the dispersion of the plasmon mode of the graphene layers are determined using Maxwell's equations. The integrating graphene with plasmonic infrared absorbers aims to harness the unique characteristics of graphene—such as its tunable conductivity, remarkable optical properties, and the ability to manipulate surface plasmon resonances – to enhance the performance of infrared absorbers. The combination of graphene with plasmonic structures allows for actively controlling and tuning the absorption properties of materials in the infrared spectrum. This integration offers the potential for more efficient and versatile devices for applications like sensing, imaging, energy harvesting, and communication systems operating in the infrared range.

6.1   Graphene Infrared Absorber

We introduce a design based on a plasmonic infrared absorber (PIRA) nanostructure, illustrated in Figure 6.1. This design aims to theoretically demonstrate an infrared absorber plasmonic nanostructure with graphene surface resonance enhancements in the wavelength range from 3 to 14 μm. The absorption spectra at these wavelengths can be actively manipulated due to the tunable conductivity of graphene. We investigate the effect of geometric parameters on absorption performance. The objective is to offer a comprehensive design guide for developing tunable resonant graphene conductivity, since graphene properties can enhance the performance of SPR, and the optical conductivity of graphene varies with changes in the number of graphene monolayers stacked. We use suitable boundary conditions within the interfaces and the complex conductivity $\sigma(\omega)$ as a function of frequency ω, temperature T, and chemical potential μ. Ideally, the pure chemical potential of the graphene is equal to zero at any given temperature. However, according to theoretical demonstration, graphene can support SPPs in the infrared ranges and provides a wide range of electromagnetic properties. In Figure 6.1 (a), the emission wavelength from 3 to 6 μm was obtained due to interaction with metallic

absorber without graphene intervention. Figure 6.1 (b) demonstrates the graphene intervention with significant enhancement at wavelengths ranging from 6.5 to 14 μm, and the number of graphene layers is ten.
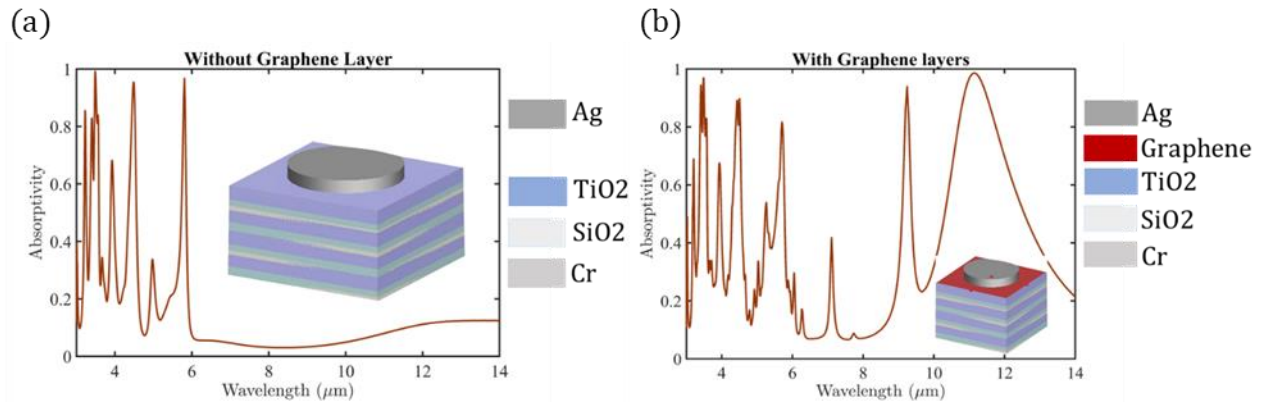
Figure 6.1: We displayed our schematic diagram of the proposed infrared absorber PIRA inside figure (a) Absorption without graphene (b) with graphene.

6.1.1   Graphene

We investigate the properties of graphene monolayers and multilayers within the infrared region of the electromagnetic spectrum. The dispersion of the plasmon mode is calculated using Maxwell's equations, which govern electromagnetic fields. Graphene is represented by a surface conductivity (Slepyan et al., 1999), which must be derived from a microscopic quantum-dynamical model or measurement. Our discussion encompasses plane wave reflection and transmission through graphene, incorporating surface wave excitation associated with high frequencies. The behaviour of surface waves is determined by the relative significance of interband and intraband contributions to conductivity (Mikhailov and Ziegler, 2007), and the propagation of these waves can be modulated by varying the chemical potential. For instance, in isolated graphene characterised by complex surface conductivity ($\sigma = \sigma^{'} + j\sigma^{''}$), a perfect transverse-electric (TE) surface wave exists if $\sigma'' > 0$, corresponding to interband conductivity. Conversely, a transverse-magnetic (TM) surface wave exists for $\sigma'' < 0$, linked to intraband conductivity. Therefore, the imaginary surface conductivity (σ'') can be changed by tuning the chemical potential at infrared frequencies or wavelengths and giving some control over surface wave properties.
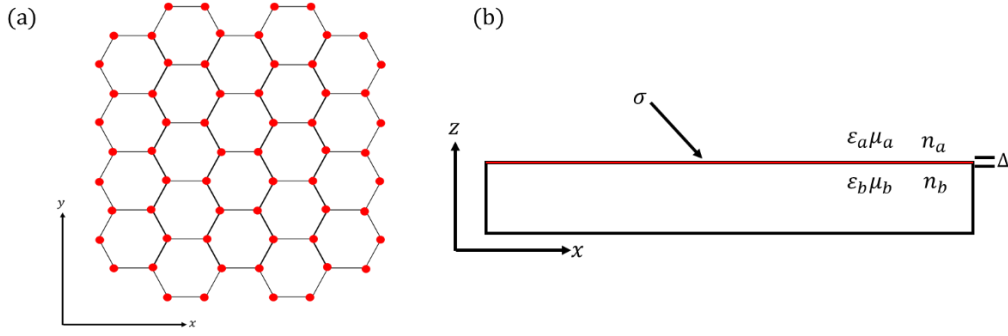
Figure 6.2: (a) is the graphene sheet, where the small circles denote carbon atoms, and (b) graphene is characterised by conductance σ at the interface between two different materials.

As we characterize in Figure 6.2, the graphene sheet lies in the x and y plane at the interface between two different materials where all the material parameters are complex. Then graphene is represented as a 2D material with surface conductivity $\sigma(\omega, \mu_c, \Gamma, T)$, while ω is an angular frequency, μ_c, is chemical potential, Γ is the scattering rate that we assume to be independent of energy, and T is the temperature. We used the Kubo expression to calculate the surface conductivity of the single graphene layer, which is given by:

$$\sigma(\omega, \mu_c, \Gamma, T) = \sigma_{intra}(\omega, \mu_c, \Gamma, T) + \sigma_{inter}(\omega, \mu_c, \Gamma, T) \tag{6.1}$$

$$\sigma_{intraband} = \frac{-je^2}{\pi\hbar^2(\omega+j2\Gamma)} \int_0^\infty \varepsilon \left(\frac{\partial f_E(\mathcal{E})}{\partial \varepsilon} - \frac{\partial f_E(-\mathcal{E})}{\partial \varepsilon} \right) \partial \varepsilon \tag{6.2}$$

$$\sigma_{interband} = \frac{je^2(\omega+j2\Gamma)}{\pi\hbar^2} \int_0^\infty \frac{\partial f_E(-\mathcal{E})-f_E(\mathcal{E})}{(\omega+j2\Gamma)^2-4(\varepsilon/\hbar)^2} \partial \varepsilon \tag{6.3}$$

Where $-e$ is the electron charge, $\hbar$ is the reduced Planck's constant ($\hbar = h/2\pi$), and $f_E(\mathcal{E}) = \exp(\varepsilon - \mu_c/K_BT + 1)^{-1}$, is the fermi Dirac distribution, also, K_B, is Boltzmann's constant. For isolated graphene sheets, the chemical potential is determined by the carrier density d_c, which stated:

$$d_c = \frac{2}{\pi\hbar^2 v_F^2} \int_0^\infty \varepsilon[f_E(\varepsilon) - f_E(\varepsilon + 2\mu_c)]\partial \varepsilon \tag{6.4}$$

Furthermore, while we study graphene using the conductivity function, other optical materials are described using the permittivity function. We turned surface conductivity into a volumetric permittivity by considering equation 6.5.

$$\varepsilon(\omega) = \varepsilon_0 \varepsilon_r + j\frac{\sigma(\omega)}{\omega\Delta} \tag{6.5}$$

Where the ε_0 is the vacuum permittivity, ε_r, are relative dielectric constants of the materials and Δ the graphene sheet thickness.

6.1.2 Plasmonic Infrared Absorber Graphene Integration

Plasmonic infrared absorber graphene integration refers to the combination of graphene material into plasmonic infrared absorbers. Graphene, a single layer of carbon atoms arranged in a two-dimensional honeycomb lattice, possesses exceptional optical and electrical properties. Integrating graphene with plasmonic infrared absorbers has unveiled significant scientific and technological interest in the mid-infrared spectral range (2-20 μm). This range encompasses numerous potential optoelectronic applications, including spectroscopy, materials processing, chemical and biomolecular sensing, remote explosive detection, and covert communication systems (Hoffman and Gmachl, 2012, Soref, 2010). Integrating these applications with electronic devices increases the potential for designing devices capable of actively controlling surface plasmon resonance at metal/dielectric interfaces (Raether, 1988c). The mid-infrared spectral region is also appealing for studying plasmonic devices (Stanley, 2012, Yu et al., 2012). However, due to a relatively weak refractive index change with an electrical bias, mechanical force, or temperature, active plasmonic devices typically exhibit poor optical performance, such as high-power consumption or slow response time.

Graphene, a single layer of carbon atoms, exhibits many unique physical features and has been recently investigated for nanoscale optoelectronic integrated circuits. Graphene-based plasmonic nanostructures support highly confined plasmonic modes that can be tuned via chemical or electrostatic doping and are promising to serve as future platforms for highly integrated plasmonic devices ranging from infrared to higher frequencies (Ju et al., 2011, Li and Yu, 2013).

6.2 Composite Layer Plasmonic Infrared Absorber

The proposed PIRAs have configuration characteristics such as stacked one-dimensional (1D) periodic lattices, in which a finite periodic lattice of $[Cr\text{-}SiO_2\text{-}TiO_2]^4$ is deposited on top of a quartz heating element substrate with a unit cell consisting of triple nanolayers of Cr, SiO_2, and TiO_2. A two-dimensional (2D) plasmonic absorber with a lattice periodic along x and y is placed on top of this lattice, and four (4) represents the number of lattice periods. We select SiO_2 and TiO_2 due to their high refractive index differences and melting points. The electrical

voltage is applied to the quartz thin film element to generate Joule heating, thereby elevating the temperature of the PIRAs. Since the metamaterial structure's design is embedded, we decided that the heating element should be an external component. The thickness of the PIRA structure is enough to handle the transmission, and the thickness of the heating element does not affect the optical properties of the PIRAs in the wavelength range. Table 6.1 displays the simulation parameters for the PIRA design structure.

Table 6.1: Design parameters

Materials	Thickness	Radius
Silicon dioxide (SiO$_2$) layer	380 nanometres (nm)	
Titanium dioxide (TiO$_2$) layer	650 nanometres (nm)	
Chromium (Cr) layer	4 nanometres (nm)	
Plasmonic Absorber (silver (Ag))	600 nanometres (nm)	1400 nanometer (nm)

6.2.1 Optical Characteristics

Transmission and absorption coefficients through the PIRAs have been investigated and displayed in Figure 6.3(a) and (b). The design model of the PIRA structure performed does not rely on the photonic bandgap. The optical spectrum of the structure is investigated by the transfer matrix method (TMM). The graphene-enhanced at the wavelength 6 to 14 μm exhibited an extraordinary emission that can be beneficial for optoelectronics applications, including microbolometers (Richards, 1994, Maier and Brückl, 2009, Maier and Brueckl, 2010, Du et al., 2015); thermal images (Liu et al., 2010b), thermal-photovoltaic solar energy conversion(Tian et al., 2007, Law et al., 2005, Sai and Yugami, 2004, Lin et al., 2003a, Coutts, 1999).

According to the International Commission on Illumination (CIE) (Protection, 2013), three infrared radiation bands must be considered: A-band λ = 0.7 - 1.4 μm, B-band λ = 1.4 - 3 μm, and C-band λ = 3 - 1000 μm. Since the C bands are essential for many real-world applications such as environmental control, health, medical industry, security, and defence sense, it is also home to the spectra peak of the thermal emission of most biological and mechanical objects with temperatures ranging from 215k to 1400k (Jung et al., 2017). For this reason, it is important for security and defence applications related to thermal targeting, night vision, energy harvesting, and conservation. As a result, the PMMs in this thesis with enhanced

emissivity covered wavelengths ranging from 3 -14 μm for both PSG and PIRA design structures.

Figure 6.3 illustrates how the geometric parameters of the metal stack influence the absorption and transmission performance of the PIRA structure. The behaviour of transmission and absorption shows a step-like pattern, resembling homogeneity, which arises from the presence of chromium stacked within the material arrangement. The transmission and absorption coefficients presented in Figure 6.3 were analysed using the TMM method.
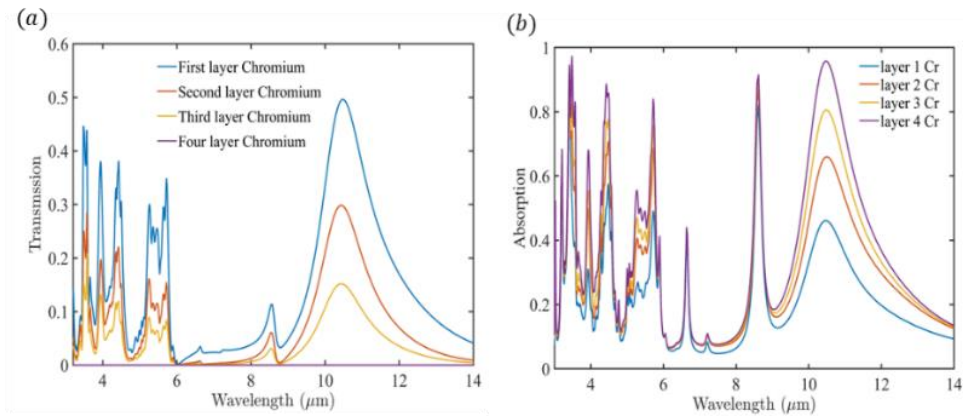
Figure 6.3: (a) Transmission coefficient (b) Absorption coefficient.

Figure 6.4 (a)-(d) depict the mode performance of the metal absorber within the structural material arrangement, as well as the |E|2 field distribution of the PIRAs at various resonant wavelengths. Figure 6.4 (a) and (b) indicate emission at high frequency, and figure (c) and (d) demonstrate the low-frequency emission behaviours. It is observed that from figure 6.4 (b) and (c), the Cr and SiO$_2$ layer act as Bragg-reflector, and the light conferment within these layers are transmitted periodically, passing through the plasmonic material absorber (Ag).
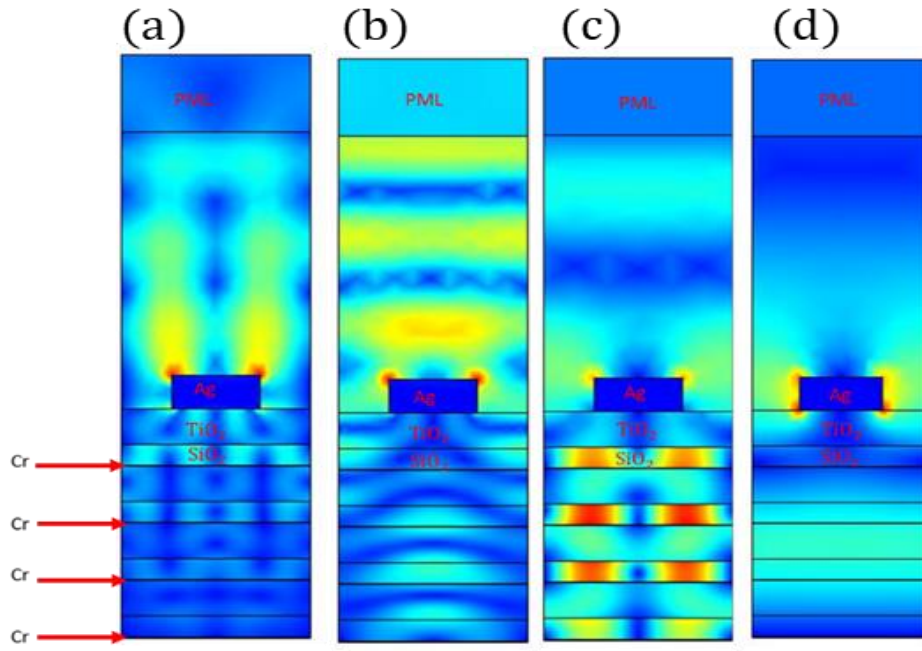
Figure 6.4: Time-averaged field distributions |E| of the PIRAs at specific wavelengths

Furthermore, our investigation based on Figure 6.5, includes a single graphene sheet, examining its reflectivity, transmissivity, and absorptivity. The presence of the graphene sheet remarkably enhances the optical spectrum of the PIRAs. Upon analysing the graphene data simulation profiles in Figures 4.8 (a) and (b), it is evident that graphene exhibits a high imaginary conductivity and low real conductivity. Both the real and imaginary parts have comparable magnitudes. The transmission and reflection spectra of Figure 6.5 (a) and (b) indicate graphene obtained high transmission and low reflection for each layer. Therefore, this behaviour allows the optical conductivity of graphene to vary with a change in the number of graphene monolayers, and this change improves the performance of SPR. Furthermore, SPs bound to the surface of the graphene layer exhibit favourable properties of low losses, high tunability and extreme confinement (Koppens et al., 2011). Figure 6.5 (a) demonstrates the absorption generated from each layer.
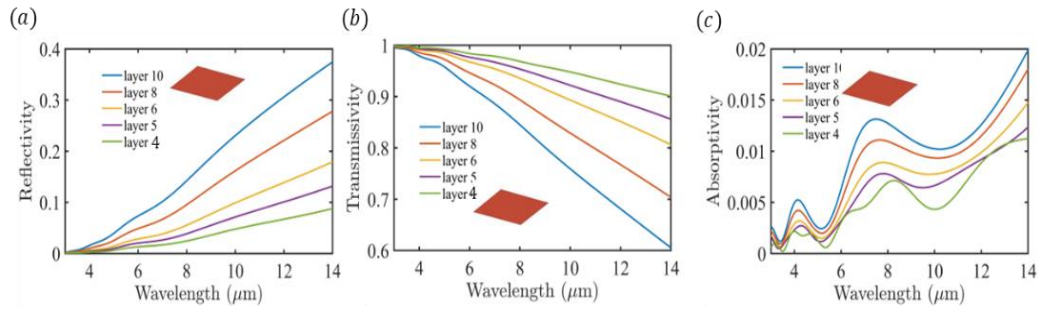
Figure 6.5: Graphene conductivity based on the performance of the layer across the spectrum range of 3-14 μm, (a) reflection spectrum, (b) transmission spectrum, and (c) Absorption spectrum.

Additionally, Figure 6.6 illustrates the performance of surface waves through the plasmonic absorber. In this figure, we intentionally excluded the metallic plasmonic absorber. The results are plotted to showcase the contribution of graphene in Figure 6.6 (a) and its absence in Figure 6.6 (b). Conversely, Figure 6.6 (c) displays the reflection and transmission spectrum without chromium layers. Notably, the presence of chromium layers significantly influences the PIRA spectrum.
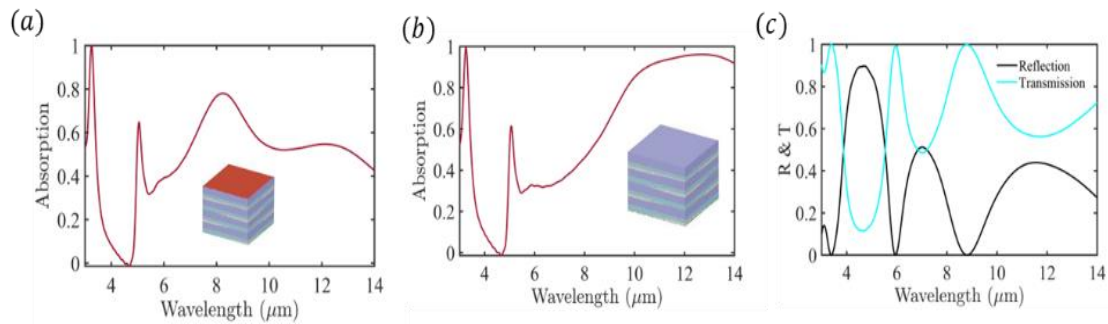
Figure 6.6: Surface resonance enhancement through graphene conductivity (a) and localized enhancement by the chromium layers (b), also (c) demonstrated the reflection and transmission based on SiO_2 and TiO_2.

The results in Figure 6.7 demonstrates PIRA structure with difference metals patch on top of $[Cr\text{-}SiO_2\text{-}TiO_2]^4$ arrangement. Such metal includes gold (Au), silver (Ag), copper (Cu) and aluminium (Al). From this perspective, it is evident that Ag, Au, and Cu exhibit significantly similar characteristics and behaviour compared to Al across the spectral range of 3 to 14 μm.
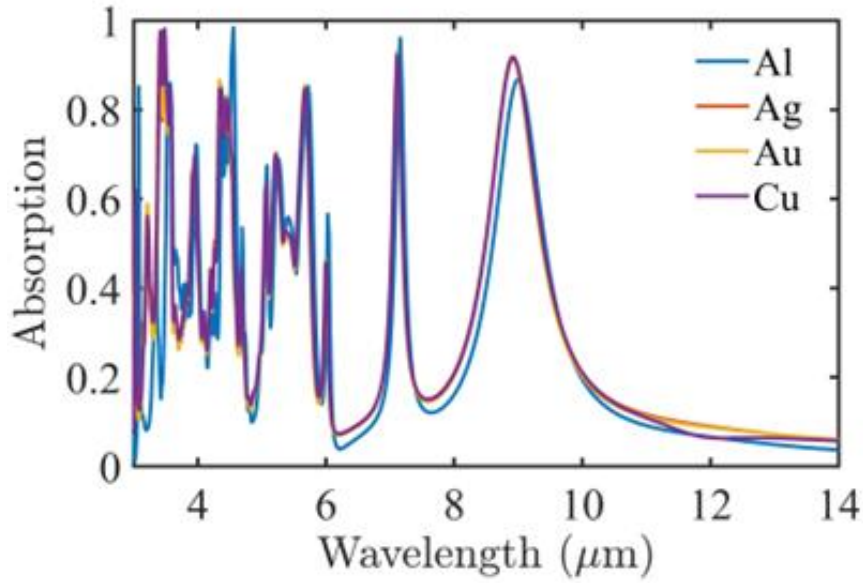
Figure 6.7: Noble metals, where Al aluminium, Ag silver, Au gold and Cu copper.

6.2.3 Angular and Tunable Spectra

We investigated angular and tunable emission properties of the PIRA structure in the mid-infrared band, with a graphene interface that connects the conducting and dielectric components in the structure. The ability of graphene in this work is to modify graphene conductivity using surface wave charge carriers. The interaction of the electromagnetic field with the collective plasma excitation causes electromagnetic wave confinement at the metal and dielectric contact. Graphene conductivity can also be altered by chemical doping, an electric field, a magnetic field, or a gate bias voltage (Wang et al., 2008, Wright and Zhang, 2010). In Figure 6.8 (b), the radius of the plasmonic absorber shifts from 1000 to 1400 nm at the same period, generating a shift in the emission wavelength of the entire spectrum. Figure 6.8 (a) depicts absorption based on a plasmonic absorber without graphene layers at various radius.
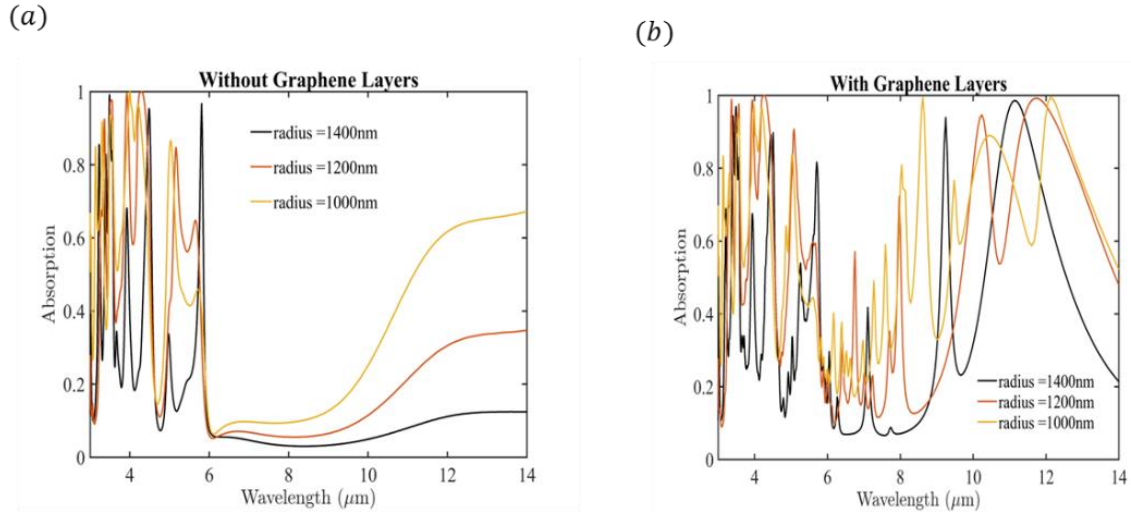
Figure 6.8: Absorption spectra as a function of metal patches from 1000 – 1400nm (a) without graphene layers and (b) with ten graphene layers.

Furthermore, the plasmonic waves in graphene have extremely high field confinement. According to theoretical studies, the electric field of the mid-infrared plasmonic wave is localized in a layer a few tens of nanometres thick (Jablan et al., 2009). A highly localized optical field induces a strong light-matter interaction and can be used to create high-sensitivity sensors or efficient nonlinear optical devices (Mikhailov, 2011). The plasmonic wave also has a low group velocity over a wide range of wavelengths, allowing for further enhancement of light-matter interaction as waves propagate slowly through the media (Jablan et al., 2009). Therefore, our PIR absorber with graphene allows us to measure the dispersion relationship and electro-optic property of the plasmonic waves in graphene. Since the guide mode resonance couples, the electromagnetic wave propagates in the plane interface, creating a great optical transmission resonant change. Then, the wave vector $(k_g(\omega))$ of the graphene interface in between the plasmonic absorber and dielectric material can be described as.

$$k_g(\omega) \approx \frac{\pi \hbar^2 \varepsilon_0 (\varepsilon_a + \varepsilon_b)}{e^2 f_E} \left(1 + \frac{j}{\omega \tau}\right) \omega^2 \qquad 6.6$$

Where the ε_0 is the vacuum permittivity, ε_a and ε_b, are the dielectric constants of the materials above and below the graphene film, τ is the carrier relaxation time ($\tau = \mu f_E / e v_f^2$), and $f_E = \hbar v_F (\pi d_c)^{1/2}$, is the absolute value of the Fermi energy level, and $v_F \approx 10^6 \, m/s$, is the Fermi velocity in graphene. The electrostatic gate can also change the Fermi level in graphene based on a PIR absorber. The result in Figure 6.9 shows the enhancement of the tunable conductivity of graphene from 0.4 eV to 1 eV. The surface conductivity of the graphene can be tuned by

applying the external voltage source, which turns the chemical potential μ_c. These changes in μ_c introduce a turning in the absorption spectrum, as shown in Figure 6.9.
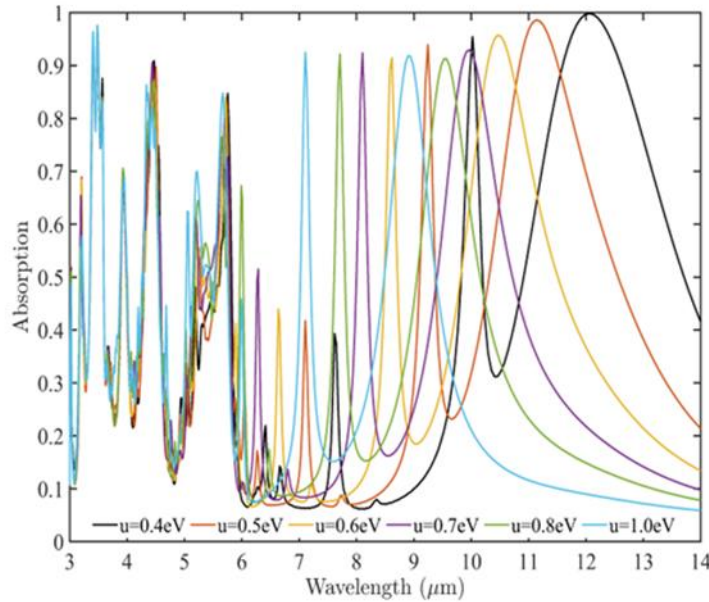
Figure 6.9: The spectra absorption of the PIRAs with the change in the chemical potential.

There has been an increase in interest in manufacturing thermal emissions using nanostructures. Several novel coherent, directional, polarised, and narrowband thermal light sources and wavelength-selective emitters have been proposed and investigated. Figure 6.10 demonstrates light absorption based on incidence polarisation angles from 5 to 30 degrees. The resonant wavelength of the multi-emissions varies significantly with the polarisation angle changes, and the linewidth of these emissions is still narrow, as illustrated in Figure 6.10 (a). However, we observed small transmission, which corresponds to higher emission orders when the angle of incidence varies from 5 to 30 degrees, illustrated in Figure 6.10 (b). Also, we observed the back reflection emission in Figure 6.10 (c) when the polarisation angle reached 25 to 30 degrees. This happens when the direction of the incidence angle is perpendicular or intersects with the Bloch boundary, causing most energy to reflect the PML surface boundary and some to reflect on top of the metallic absorber before going back to the interface of metal and dielectric. Figure 6.10 (d) displayed the transmission spectra conditions from $9 - 14$ μm when the angle of incidence changed from $5 - 30$ degrees.
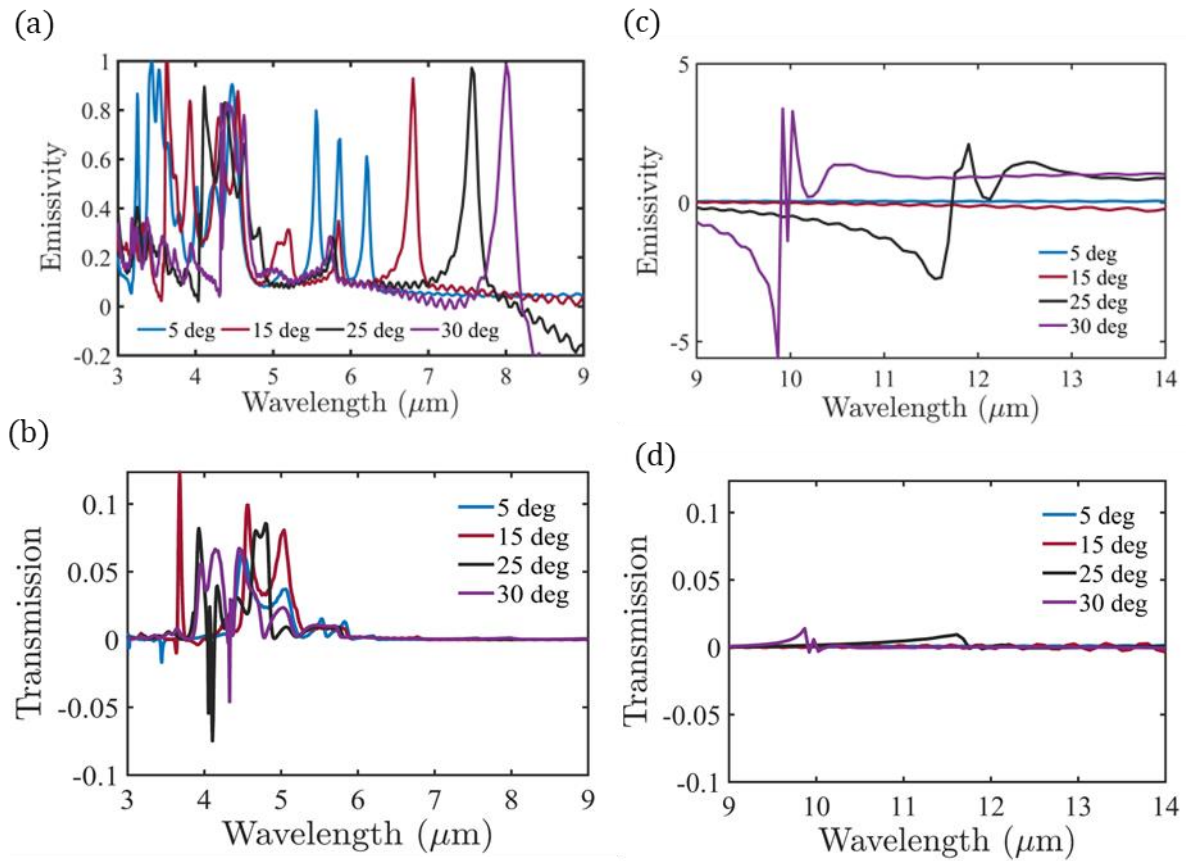
Figure 6.10: The spectra absorption of the PIRAs with the polarisation changes (a) and (b) are the emission transmissions spectra of 3-9 µm, (c) and (d) are the emission transmissions spectra of 9-14 µm,

6.3 Mechanisms Plasmonic Metamaterial

A new revolutionary field in photonics is plasmonic metamaterials, combines the best parts of photonics and electronics by coupling photons to metal conduction electrons as surface plasmons (SP). This concept has been used in various applications, including negative indexes of refraction, magnetism at visible frequencies, and cloaking devices, as we explained in the previous chapter. Plasmonic metamaterials are composites of subwavelength structures designed to respond differently to an incident electromagnetic wave. In the most general approach to designing metamaterials, the properties of a metamaterial are fixed at the time of fabrication by the sizes of each unit cell and the materials used. Integrating dynamic components into a plasmonic metamaterial system allows for the creation of tunable plasmonic resonant responses. In this thesis, the investigation of the active and passive components of the PMMs is to understand the underlying coupling mechanisms that can be used to improve the absorption/emissivity including tunability. We showed how the thermal motion of a phase transition material can be used to create dynamically tunable plasmonic metamaterials.

6.3.1   Thermal Radiation PSGs and PIRAs

We examine the coherent thermal radiation emitted by PSGs and PIRAs at temperature *T* and compare it to the emission of an ideal blackbody at the same temperature. The Wiener-Khinchin theorem states that the degree of temporal coherence of radiation emitted by a thermal source can be calculated by considering the Planck distribution and the Boltzmann constant. Figure 6.11 compares the thermal emission spectrum as a function of wavelength to the blackbody's spectrum at the same temperature. The Figure shows that temperature affects radiant power (W/sr/m²/μm), indicating that the thermal emitter's radiant power increases with temperature. Radiant power refers to the emission, reflection, or transmission of radiant energy. We plotted the radiant power versus wavelength for PSGs and PIRA structures from 450K to 750K. Figure 6.11 (a-c) corresponds to PIRA structure at different temperatures, and (d-e) corresponds to PSG structure at different temperatures.
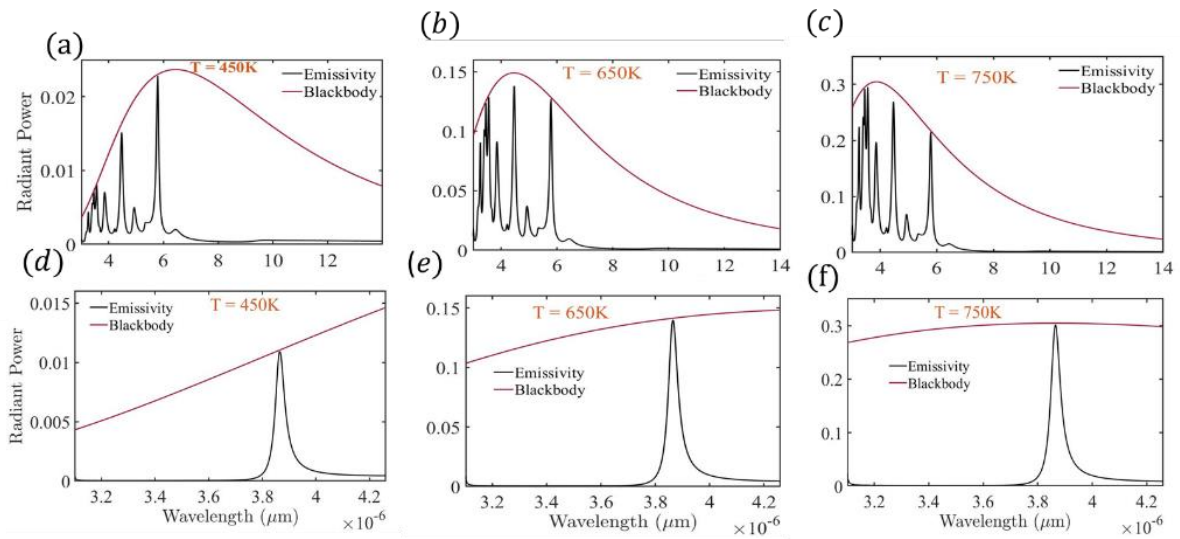
Figure 6.11: illustrates the spectra of thermal radiation compared to blackbody radiation at the same temperature. PIRAs (a, b, and c) and PSGs (d, e, and f).

6.3.2   Thermal Modulations

We artificially tailor an electromagnetic response across various spectral ranges. Thermal sources, such as directionality and monochromaticity, have been achieved. PSGs and PIRAs are optical structures that require an external thermal source to provide coherent thermal light. Furthermore, the properties of these structures are fixed at the time of fabrication by the sizes and shapes of each unit cell, as well as the materials used. As a result, the fast response emission

of the thermal modulation is derived from an external source (a heater)—the external sources of the PSG and PIRA structures as input sources that require fast temperature response. We refer to the Electrically Driven, Ultrahigh-Speed, on-chip Light Emitter Based on Carbon Nanotubes (Miyoshi et al., 2018) as an input source to PSGs and PIRAs. Since the high-speed response of these structures depends on high heat dissipation and power spectra-radiant increases by the temperature. Therefore, the modulation speed of these structures is explained by the speedy temperature response of the external device.

We demonstrate the PSG and PIRA response time at different temperatures in Figure 6.13. This is accomplished by taking the absorption power from the FDTD into the heat transport simulation of the device solver. These results demonstrate a single-unit power absorber with charging temperature versus time within 0.5 fs. We numerically calculated the transient temperature distribution of the PSG and PIRA structures, and we considered thermal only from the physic solver to solve the simultaneous heat conduction equations. The heat transport solver calculates the solution T to the heat equation in a solid medium as:

$$\rho c_p \frac{\partial T}{\partial t} - \nabla(k \nabla T) = q_c \qquad 6.7$$

Where k is the thermal conductivity in (W/m. K), c_p is the heat capacity (J/kg·m^3), ρ is the mass density in (kg/m^3), and q_c is charging energy transfer (W/m^3). The materials data for these simulations are explained in the table below. Table 6.2 displays the thermal simulation parameters for the PIRA and PSG design structures.

Table 6.2: Thermal heat simulation data

Materials	Heat Capacity (C_p)	Thermal conductivity (k)	Density (ρ)
Silver (Ag)	235 J/kg·m^3	425 W/mK	10500 kg/m^3
TiO$_2$	690 J/kg·m^3	7.4W/mK	4950 kg/m^3
SiO$_2$	709 J/kg·m^3	1.38 W/mK	2203 kg/m^3
Cr	448 J/kg·m^3	93.7 W/mK	7150 kg/m^3
Graphene	700 J/kg·m^3	2000 W/mK	2250 kg/m^3

In Figure 6.12, we demonstrate the modulation of the thermal emission based on time and temperature changes. We obtained the results by running an optical and heat transfer simulation. The temperature response of the PIRA structure has a significant decay speed

because of the metallic stack in the structuring arrangements, as shown in Figure 6.12 (a) and (b). Figure 6.12 (c) and (d) illustrate temperature changes based on the PSG structure and the decay response times larger than the PIRA structure.
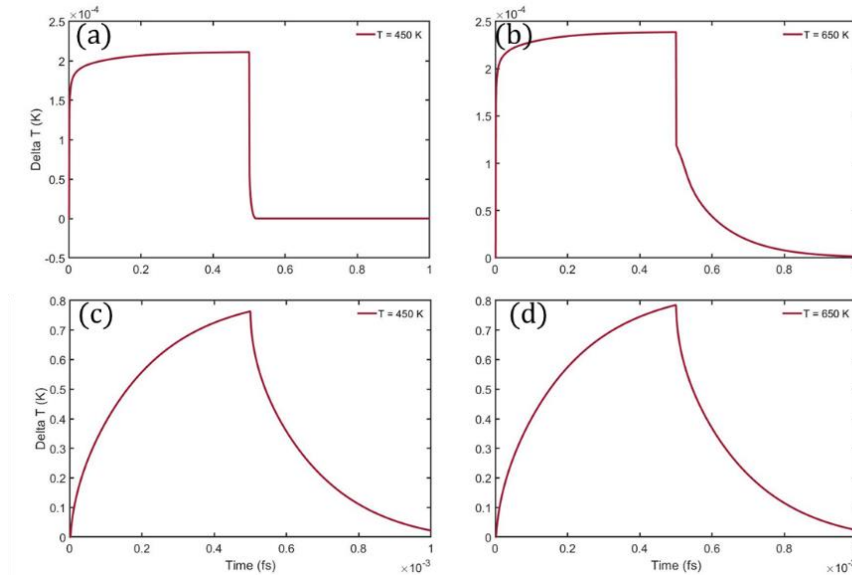
Figure 6.12: Transient temperature of one periodic cell at difference temperature time response, (a and b) for the PIRA and (c and d) for the PSGs

6.4   Media Interface Penetration

According to Snell's law, the incident electromagnetic wave is a travelling wave in the first medium (n_a) before reaching the second medium (n_b). The incident wave will enter and be transmitted at a specific angle (θ_t), known as the angle of transmission, between the interface of two more precise materials. The remaining portion of the incident wave will be reflected in the first medium at an angle known as the angle of reflection (θ_r). Nonetheless, if the direction of the incident wave is perpendicular to the interface, the angle of incidence would be equal to zero ($\theta_i = 0$), and the angle of transmission and reflection would be equal to zero ($\theta_t = \theta_r = 0$). Suppose the incident wave travels to the interface between two media at a specific angle. In that case, θ_i must be greater than zero, and the transmission and reflection angles will no longer equal zero. This characteristic is known as the penetration behaviour of EM surface waves. The proportion of an incident wave that is transmitted is measured by the transmission coefficient (θ_t), which is defined as the ratio of the amplitude of the transmitted electric field to the amplitude of the incident electric field:

$$t = \frac{E(\,transmitted\,)}{E(incident)}$$

6.8

Additionally, the reflection coefficient (r) is the ratio between the amplitude of the reflected electric field and the amplitude of the incident electric field:

$$r = \frac{E(transmitted)}{E(incident)} \qquad 6.9$$

The polarisation of the PSGs and PMMs, defined by the direction of the electric field and the EM wave, does not affect the form of the equations for plane waves travelling normally to the interface of two materials. However, for waves travelling obliquely to the interface, the expressions for transmission and reflection coefficients are affected by how the wave is polarised. As a result, discussions of wave equations for wave penetration are made regarding the polarisation of EM waves. The EM wave can be polarised either parallel or perpendicular to the plane of incidence. Two vectors define the plane of incidence: the propagation vector in the direction of wave propagation and the unit vector normal to the interface.

6.5 Conclusion

We propose an integrated thermophotonic structure based on the plasmonic infrared absorber (PIRA) scheme to create highly efficient and selectively spectral thermal emitters, markedly enhancing absorptivity within the infrared spectrum. Our investigation focused on the impact of geometric parameters on both transmission and absorption performance. The transmission and absorption coefficients were analysed using the transfer matrix method (TMM). Employing plasmonic metamaterial simulation enhanced by graphene, we achieved bio-coherent emission within the infrared spectrum ranging from 3 to 14 μm. This approach allowed for tunable emission/absorption, driven by the surface conductivity of graphene. Within this chapter, we successfully obtained a multi-wavelength absorption spectrum spanning from 3 to 14 μm and demonstrated angular tunability with and without graphene surface conductivity. Moreover, we compared the thermal emission spectrum against the wavelength function to the blackbody's spectrum at the same temperature and conducted heat simulations of one periodic cell at different temperature responses, yielding significant results. Our work suggests that the design of PIRA could offer an enhanced and integrated strategy for infrared sources, potentially finding applications in areas such as infrared heating, thermophotovoltaics, thermal imaging, and beyond.

Chapter 7
Conclusion and Outlook

Photonics technology is commonly regarded as a key enabling technology for the 21st century, and the ability to control light lies at the core of photonics. Plasmonics is a subcategory of photonics that specialises in the interaction between the electromagnetic field and free electrons in a metal, typically at nanoscale dimensions. The field of metamaterials, which consists of man-made artificial materials, dates back only to the year 2000. However, it has grown tremendously over the past decade. These materials comprise sub-wavelength scale structures that can be considered as the atoms in conventional materials. The collective response of a randomly or periodically ordered ensemble of such meta-atoms defines the properties of the metamaterial. These properties can be described in terms of effective material parameters such as permittivity, permeability, refractive index, and impedance. These effective material parameters can be tailored at will to achieve the desired optical response, thus offering improved control over the propagation of electromagnetic waves. This advancement paves the way for many exciting applications, including negative refractive index materials, invisibility cloaking, integrated optical chips, interconnects, and more.

In this thesis, we focused on the optical properties of plasmonic metamaterials in the visible and near-infrared wavelength ranges for thermal applications. The meta-atoms of the investigated samples are plasmonic resonators, which we manufactured as artificial composite materials. The properties of a metamaterial are fixed at the time of fabrication by the dimensions of each unit cell and the materials used.

In Chapter 3, we established a theoretical framework for the proposed research topic by conducting studies on the Maxwell equations. These investigations explored the interaction between electromagnetic waves and free electrons in metals. Additionally, we considered the classification of materials to enhance our understanding of their properties, focusing on permittivity and permeability.

In Chapter 4, we demonstrated the simulation algorithm for nanophotonics design based on the artificial composite arrangement. It covered Lumerical methods and analysis using finite difference time domain (FDTD). This chapter demonstrated methods used to achieve thermal

coherence emission. We explained the structural analysis and theoretical calculations of reflection and transmission based on electric and magnetic fields. The physic modelling of the emissivity/absorptivity was treated based on Kirchhoff's law of thermal radiation.

In Chapter 5, we presented a self-assembled design of a plasmonic stacked grating structure (PSGs) comprising rectangular metallic patches atop a one-dimensional Bragg grating, along with air corrugation designs incorporated into the metallic patches atop the Bragg grating. We performed angle-dependent spectroscopic ellipsometry measurements in which the polarisation state of the incident wave was modulated between TM- and TE-polarisation, such that we could measure the phase difference between both reflected waves by lock-in measurements. The PSG's strategy for mid-IR thermal emission demonstrates the potential for enhanced and coherent thermal radiation. We employed the 3D-FDTD method to analyse the spectral and angular emission responses of the PSGs. An intriguing characteristic of this thermal emitter scheme is the occurrence of emission resonant peaks within the bandgap of the 1D-BG. Consequently, reducing the Bragg grating band gap significantly narrows the full width at half maximum (FWHM) of the emission spectrum. While substituting the Bragg grating with a metallic film can generate a strong resonant emission peak, the resulting FWHM would be much larger compared to our proposed method. Additionally, the operating wavelength of the thermal emitter can be flexibly adjusted by shifting the bandgap of the Bragg grating. These attributes create opportunities for achieving a cost-effective and compact mid-IR source platform. Due to their tunable and narrow spectral and angular response, PSGs hold promise for various applications, including thermal sensing, security, infrared diagnostics, and more.

In Chapter 6, we extended the concepts developed in Chapter 5 by introducing a design based on a plasmonic infrared absorber (PIRA). This design aims to theoretically demonstrate an infrared absorber plasmonic nanostructure with graphene surface resonance enhancements in the wavelength range from 3 to 14 µm. The absorption spectra within these wavelengths can be actively manipulated due to the tunable conductivity inherent in graphene. The objective is to offer a comprehensive design guide for developing tunable resonant graphene conductivity since graphene properties can enhance the performance of SPR, and the optical conductivity of graphene varies with changes in the number of graphene monolayers stacked. We investigated the effect of geometric parameters on absorption performance. The transmission and absorption coefficients were analysed using the transfer matrix method (TMM). The absorption spectrum with graphene and without graphene layers was achieved across the spectrum wavelength of 3

to 14 µm. The graphene-enhanced at the wavelength 6.5 to 14 µm exhibited an extraordinary emission that can be beneficial for optoelectronics applications, including microbolometers, thermal images and thermal-photovoltaic solar energy conversion.

The fast modulation of the tunable plasmonic depends on the fast temperature response to the plasmonic material structure. Since the plasmonic metamaterial is embedded in the design, the modulation components must be external to control the thermal coherent emission spectrum, including the fast response emission, which depends on fast temperature through the plasmonic metamaterial structure. The plasmonic metamaterial structures were considered theoretically and by simulations in this thesis, drawing attention based on coherent thermal emission, including tunable spectral, which exhibit the emission based on structuring adjustment parameter or angular dependant tunable emission. All these features were achieved in this thesis.

Contribution to knowledge

This thesis contributes to the design of the nanostructure of plasmonic metamaterials to improve performance and achieve specific objectives. We have confirmed that plasmonic metamaterials have better performance than micro photonics and electronics in terms of size and speed limitations in the terahertz region.

We have developed a plasmonics metamaterial structure that exhibits a coherent thermal light source with features including:

- o Cost-effective in marked contrast to semiconductor devices such as laser and LED
- o Low consumption energy
- o Fast response emission
- o High-efficient mid-infrared light source.

The PSG design structure contributes tailored thermal radiation in the mid-infrared wavelength range with intriguing capabilities of:

- o High emissivity
- o Narrowband spectrum
- o Sharp angular response.

The PIR absorber design structures contribute based on active plasmon control that can be beneficial to applications such as: infrared microbolometers, infrared photodetectors, or photovoltaic cells without the need for broadband conversion filters.

Research outlook

Surface plasmons in metamaterials are hybrid excitations of electromagnetic waves in a dielectric material coupled to charge oscillations on the surface of a metal. The hybrid mode is often referred to as a surface plasmon polariton (SPP) when it propagates at a flat metal and dielectric interface. The model is known as a localised surface plasmon when bound to a subwavelength metal particle. In either case, the wavelength of the hybrid excitation, and thus the characteristic length scale associated with the mode, can be much smaller than the wavelength of the coupling radiation in free space. As a result, the field of plasmonics has sparked significant interest in applications such as optical interconnects, high-resolution imaging, and enhanced performance sensing, where strongly confined modes can provide significant benefits. The capacity to confine and manipulate light on a subwavelength scale has led to the development of new phenomena, such as enhanced thermal analysis, imaging, security, biosensing, and medical diagnoses. Metals, defined here as conducting materials with negative real permittivity resulting from the optical response of the free carriers in the material, are essential to all plasmonic architectures. Research in plasmonics has utilised noble metals such as gold and silver and has focused on the visible and near-infrared frequency ranges close to these metals' plasma frequencies, where the metals' losses are relatively low. Their permittivities are small, on par with the surrounding dielectric. Nonetheless, there is interest in expanding plasmonic research to the mid-IR wavelength range for molecular sensing, thermal imaging, source development, beam steering, and thermal signature cloaking or mimicking applications.

We have demonstrated the feasibility of several novel plasmonic metamaterial concepts. These ideas can serve as a toolbox for the future, enabling the development of platforms with superior performance to those currently in use. In Figure 1.1, the metamaterials tree of knowledge, the research in metamaterials and plasmonics in the coming years, as it is a commercially available non-destructive measurement method that can probe the phase information of localized and propagating plasmon modes, providing deeper insight into their nature. The magneto-optical Kerr effect is another closely related technique recently gaining influence in the plasmonic

community. The technique is commonly used to characterise the magnetic properties of thin layers. Still, plasmons interact strongly with magnetic fields, implying that magnetic fields could be used as additional independence in the design of magneto-plasmonic applications. The chiral metamaterials are the plasmonic community. The plasmonic structures are designed to convert the polarisation of an incident wave into the desired state, a critical step on the path to fully integrated optical chips.

Publications

Abubakar, Y., Gong, Y., Qiao, D., Fan, Y., Evered, C., Jones, A., Saleh, H.D., Li, K. and Copner, N., 2021. Enhanced narrowband mid-IR thermal radiation enabled by plasmonic stacked gratings. *OSA Continuum*, *4*(9), pp.2481-2487.

Qiao, D., Chen, G., Gong, Y., Li, K., Fan, Y., Zhang, B., Jia, F., Abubakar, Y., Jones, A., Otung, I. and Copner, N., 2020. Design and optical characterisation of an efficient polarised organic light emitting diode based on refractive index modulation in the emitting layer. *Optics Express*, *28*(26), pp.40131-40144.

CLEO/Europe-EQEC Conference 2019 at Munich, Germany during the World of Photonics Congress. Paper title: *Novel Mid-infrared Multiple Coherent Emissions for Gas Sensing.* A poster publication.

Engineering feature of Wales PhD conference, Techniquest, Cardiff November 2022, **Poster Presentation.**

Bibliography

ABDULHALIM, I. 2008. Surface plasmon TE and TM waves at the anisotropic film–metal interface. *Journal of Optics A: Pure and Applied Optics,* 11**,** 015002.

ABUBAKAR, Y., GONG, Y., QIAO, D., FAN, Y., EVERED, C., JONES, A., SALEH, H. D., LI, K. & COPNER, N. 2021. Enhanced narrowband mid-IR thermal radiation enabled by plasmonic stacked gratings. *OSA Continuum,* 4**,** 2481-2487.

AGRANOVICH, V. M. 2012. *Surface polaritons*, Elsevier.

AHN, Y., DUNNING, J. & PARK, J. 2005. Scanning photocurrent imaging and electronic band studies in silicon nanowire field effect transistors. *Nano Letters,* 5**,** 1367-1370.

AIZPURUA, J. & HILLENBRAND, R. 2012. Localized surface plasmons: basics and applications in field-enhanced spectroscopy. *Plasmonics.* Springer.

ALAEE, R., FARHAT, M., ROCKSTUHL, C. & LEDERER, F. 2012. A perfect absorber made of a graphene micro-ribbon metamaterial. *Optics express,* 20**,** 28017-28024.

ALIPOUR-BANAEI, H. & MEHDIZADEH, F. 2012. A proposal for anti-UVB filter based on one-dimensional photonic crystal structure. *Digest Journal of Nanomaterials and Biostructures,* 7**,** 361-371.

ALIPOUR-BANAEI, H. & MEHDIZADEH, F. 2013. Significant role of photonic crystal resonant cavities in WDM and DWDM communication tunable filters. *Optik-International Journal for Light and Electron Optics,* 124**,** 2639-2644.

ALIPOUR-BANAEI, H., MEHDIZADEH, F. & HASSANGHOLIZADEH-KASHTIBAN, M. 2013. Important Effect of Defect Parameters on the Characteristics of Thue-Morse Photonic Crystal Filters. *Advances in OptoElectronics*.

AMBATI, M., GENOV, D. A., OULTON, R. F. & ZHANG, X. 2008. Active plasmonics: surface plasmon interaction with optical emitters. *IEEE Journal of Selected Topics in Quantum Electronics,* 14**,** 1395-1403.

AMENDOLA, V. & MENEGHETTI, M. 2012. Advances in self-healing optical materials. *Journal of Materials Chemistry,* 22**,** 24501-24508.

AMENDOLA, V., PILOT, R., FRASCONI, M., MARAGÒ, O. M. & IATÌ, M. A. 2017. Surface plasmon resonance in gold nanoparticles: a review. *Journal of Physics: Condensed Matter,* 29**,** 203002.

ANDRYIEUSKI, A. & LAVRINENKO, A. V. 2013. Graphene metamaterials based tunable terahertz absorber: effective surface conductivity approach. *Optics express,* 21**,** 9144-9155.

ANTIPOV, S. P., LIU, W., POWER, J. G. & SPENTZOURIS, L. K. Left-handed metamaterials studies and their application to accelerator physics. Proceedings of the 2005 Particle Accelerator Conference, 2005. IEEE, 458-460.

ARNOLD, C., MARQUIER, F., GARIN, M., PARDO, F., COLLIN, S., BARDOU, N., PELOUARD, J.-L. & GREFFET, J.-J. 2012. Coherent thermal infrared emission by two-dimensional silicon carbide gratings. *Physical Review B,* 86**,** 035316.

ARPIN, K. A., LOSEGO, M. D., CLOUD, A. N., NING, H., MALLEK, J., SERGEANT, N. P., ZHU, L., YU, Z., KALANYAN, B. & PARSONS, G. N. 2013. Three-dimensional self-assembled photonic crystals with high temperature stability for thermal emission modification. *Nature communications,* 4**,** 1-8.

ASANO, T., SUEMITSU, M., HASHIMOTO, K., DE ZOYSA, M., SHIBAHARA, T., TSUTSUMI, T. & NODA, S. 2016. Near-infrared–to–visible highly selective thermal emitters based on an intrinsic semiconductor. *Science advances,* 2**,** e1600499.

AUSTIN, L. A., KANG, B. & EL-SAYED, M. A. 2015. Probing molecular cell event dynamics at the single-cell level with targeted plasmonic gold nanoparticles: A review. *Nano Today,* 10**,** 542-558.

BABAR, S. & WEAVER, J. 2015. Optical constants of Cu, Ag, and Au revisited. *Applied Optics,* 54**,** 477-481.

BAKAN, G., AYAS, S., SERHATLIOGLU, M., ELBUKEN, C. & DANA, A. J. A. O. M. 2018. Invisible Thin-Film Patterns with Strong Infrared Emission as an Optical Security Feature. 6**,** 1800613.

BAO, Q. & LOH, K. P. 2012. Graphene photonics, plasmonics, and broadband optoelectronic devices. *ACS nano,* 6**,** 3677-3694.

BARNES, W. L., DEREUX, A. & EBBESEN, T. W. 2003. Surface plasmon subwavelength optics. *Nature,* 424**,** 824.

BARSOTTI JR, R. J., VAHEY, M. D., WARTENA, R., CHIANG, Y. M., VOLDMAN, J. & STELLACCI, F. 2007. Assembly of metal nanoparticles into nanogaps. *small,* 3**,** 488-499.

BARTAL, G., MANELA, O. & SEGEV, M. 2006. Spatial four wave mixing in nonlinear periodic structures. *Physical review letters,* 97**,** 073906.

BASU, S. & FRANCOEUR, M. 2011. Near-field radiative transfer based thermal rectification using doped silicon. *Applied Physics Letters,* 98**,** 113106.

BASU, S., ZHANG, Z. & FU, C. 2009. Review of near-field thermal radiation and its application to energy conversion. *International Journal of Energy Research,* 33**,** 1203-1232.

BAUER, S., BAUER-GOGONEA, S., GRAZ, I., KALTENBRUNNER, M., KEPLINGER, C. & SCHWÖDIAUER, R. 2014. 25th anniversary article: a soft future: from robots and sensor skin to energy harvesters. *Advanced Materials,* 26**,** 149-162.

BAYINDIR, M., TEMELKURAN, B. & OZBAY, E. 2000. Photonic-crystal-based beam splitters. *Applied Physics Letters,* 77**,** 3902-3904.

BAZARGANI, H. P. 2012. Proposal for a 4-channel all optical demultiplexer using 12-fold photonic quasicrystal. *Optics Communications,* 285**,** 1848-1853.

BENNETT, J. M. & ASHLEY, E. J. 1965. Infrared Reflectance and Emittance of Silver and Gold Evaporated in Ultrahigh Vacuum. *Applied Optics,* 4**,** 221-224.

BERENGER, J.-P. 1994. A perfectly matched layer for the absorption of electromagnetic waves. *Journal of computational physics,* 114**,** 185-200.

BERINI, P. 2009. Long-range surface plasmon polaritons. *Advances in optics and photonics,* 1**,** 484-588.

BHATIA, B., LEROY, A., SHEN, Y., ZHAO, L., GIANELLO, M., LI, D., GU, T., HU, J., SOLJAČIĆ, M. & WANG, E. N. 2018. Passive directional sub-ambient daytime radiative cooling. *Nature communications,* 9**,** 1-8.

BLOEMBERGEN, N. & PERSHAN, P. 1962. Light waves at the boundary of nonlinear media. *Physical review,* 128**,** 606.

BOLOTIN, K. I., SIKES, K. J., JIANG, Z., KLIMA, M., FUDENBERG, G., HONE, J., KIM, P. & STORMER, H. L. 2008. Ultrahigh electron mobility in suspended graphene. *Solid state communications,* 146**,** 351-355.

BONOD, N., TAYEB, G., MAYSTRE, D., ENOCH, S. & POPOV, E. J. O. E. 2008. Total absorption of light by lamellar metallic gratings. 16**,** 15431-15438.

BORN, M. & WOLF, E. Principles of optics 4th edition 1970 300. Pergamon Press Ltd., Oxford and London). Google Scholar.

BORYS, N. J. 2011. *Optical structure-property relations in metal and semiconductor nanoparticles*, The University of Utah.

BOSE, J. C. 1898. On the rotation of plane of polarisation of electric wave by a twisted structure. *Proceedings of the Royal Society of London,* 63**,** 146-152.

BOUCHON, P., KOECHLIN, C., PARDO, F., HAÏDAR, R. & PELOUARD, J.-L. 2012. Wideband omnidirectional infrared absorber with a patchwork of plasmonic nanoantennas. *Optics letters,* 37**,** 1038-1040.

BOYD, R. W. 2011. Material slow light and structural slow light: similarities and differences for nonlinear optics. *JOSA B,* 28**,** A38-A44.

BRAR, V. W., SHERROTT, M. C., JANG, M. S., KIM, S., KIM, L., CHOI, M., SWEATLOCK, L. A. & ATWATER, H. A. J. N. C. 2015. Electronic modulation of infrared radiation in graphene plasmonic resonators. 6**,** 1-7.

CAMPIONE, S., MARQUIER, F., HUGONIN, J.-P., ELLIS, A. R., KLEM, J. F., SINCLAIR, M. B. & LUK, T. S. 2016. Directional and monochromatic thermal emitter from epsilon-near-zero conditions in semiconductor hyperbolic metamaterials. *Scientific reports,* 6**,** 1-9.

CAO, T., LIAN, M., LIU, K., LOU, X., GUO, Y. & GUO, D. 2021. Wideband mid-infrared thermal emitter based on stacked nanocavity metasurfaces. *International Journal of Extreme Manufacturing,* 4**,** 015402.

CARMINATI, R. & GREFFET, J.-J. 1999. Near-Field Effects in Spatial Coherence of Thermal Sources. *Physical Review Letters,* 82**,** 1660-1663.

CELANOVIC, I., PERREAULT, D. & KASSAKIAN, J. 2005. Resonant-cavity enhanced thermal emission. *Physical Review B,* 72**,** 075127.

CHARLES, A. D., RIDER, A. N., BROWN, S. A. & WANG, C. H. 2021. Multifunctional magneto-polymer matrix composites for electromagnetic interference suppression, sensors and actuators. *Progress in Materials Science,* 115**,** 100705.

CHENG, J. T. & ELLIS, P. D. 1989. Adsorption of rubidium (1+) to. gamma.-alumina as followed by solid-state rubidium-87 NMR spectroscopy. *The Journal of Physical Chemistry,* 93**,** 2549-2555.

CHO, E. S., KIM, J., TEJERINA, B., HERMANS, T. M., JIANG, H., NAKANISHI, H., YU, M., PATASHINSKI, A. Z., GLOTZER, S. C. & STELLACCI, F. 2012. Ultrasensitive detection of toxic cations through changes in the tunnelling current across films of striped nanoparticles. *Nature Materials,* 11**,** 978-985.

COSTANTINI, D., LEFEBVRE, A., COUTROT, A.-L., MOLDOVAN-DOYEN, I., HUGONIN, J.-P., BOUTAMI, S., MARQUIER, F., BENISTY, H. & GREFFET, J.-J. 2015a. Plasmonic metasurface for directional and frequency-selective thermal emission. *Physical Review Applied,* 4**,** 014023.

COSTANTINI, D., LEFEBVRE, A., COUTROT, A. L., MOLDOVAN-DOYEN, I., HUGONIN, J. P., BOUTAMI, S., MARQUIER, F., BENISTY, H. & GREFFET, J. J. 2015b. Plasmonic Metasurface for Directional and Frequency-Selective Thermal Emission. *Physical Review Applied,* 4**,** 014023.

COUNCIL, N. R. 1998. *Harnessing light: optical science and engineering for the 21st century*, National Academies Press.

COUTTS, T. 1999. A review of progress in thermophotovoltaic generation of electricity. *Renewable and sustainable energy reviews,* 3.

CUESTA-SOTO, F., MARTÍNEZ, A., GARCIA, J., RAMOS, F., SANCHIS, P., BLASCO, J. & MARTÍ, J. 2004. All-optical switching structure based on a photonic crystal directional coupler. *Optics Express,* 12**,** 161-167.

CUI, Y., HE, Y., JIN, Y., DING, F., YANG, L., YE, Y., ZHONG, S., LIN, Y., HE, S. J. L. & REVIEWS, P. 2014. Plasmonic and metamaterial structures as electromagnetic absorbers. 8**,** 495-520.

DANG, S., WANG, Z. & YE, H. 2019. Optimization and preparation of a visible-infrared compatible stealth film based on D/M/D structure. *Materials Research Express,* 6**,** 106422.

DATAS, A. & ALGORA, C. 2010. Detailed balance analysis of solar thermophotovoltaic systems made up of single junction photovoltaic cells and broadband thermal emitters. *Solar energy materials and solar cells,* 94**,** 2137-2147.

DAWSON, P., CAIRNS, G. & O'PREY, S. 2000. Prism coupler with variable coupling gap. *Review of Scientific Instruments,* 71**,** 4208-4212.

DE WILDE, Y., FORMANEK, F., CARMINATI, R., GRALAK, B., LEMOINE, P.-A., JOULAIN, K., MULET, J.-P., CHEN, Y. & GREFFET, J.-J. 2006. Thermal radiation scanning tunnelling microscopy. *Nature,* 444**,** 740-743.

DE ZOYSA, M., ASANO, T., MOCHIZUKI, K., OSKOOI, A., INOUE, T. & NODA, S. J. N. P. 2012. Conversion of broadband to narrowband thermal emission through energy recycling. 6**,** 535-539.

DEBNATH, D. & GHOSH, S. K. 2022. Optical Constants of Noble Metals at the Nanoscale within the Framework of the Drude Free-Electron Conduction Model: Implications for Liquid Crystal Sensing. *ACS Applied Nano Materials,* 5**,** 1621-1634.

DENG, H., WANG, T., GAO, J. & YANG, X. 2014. Metamaterial thermal emitters based on nanowire cavities for high-efficiency thermophotovoltaics. *Journal of Optics,* 16**,** 035102.

DI FABRIZIO, E., SCHLÜCKER, S., WENGER, J., REGMI, R., RIGNEAULT, H., CALAFIORE, G., WEST, M., CABRINI, S., FLEISCHER, M. & VAN HULST, N. F. 2016. Roadmap on biosensing and photonics with advanced nano-optical methods. *Journal of Optics,* 18**,** 063003.

DRACHEV, V., CAI, W., CHETTIAR, U., YUAN, H. K., SARYCHEV, A., KILDISHEV, A., KLIMECK, G. & SHALAEV, V. 2006. Experimental verification of an optical negative-index material. *Laser Physics Letters,* 3**,** 49-55.

DRUDE, P. 1902. Zur elektronentheorie der metalle. *Annalen der Physik,* 312**,** 687-692.

DU, K., LI, Q., ZHANG, W., YANG, Y. & QIU, M. 2015. Wavelength and thermal distribution selectable microbolometers based on metamaterial absorbers. *IEEE Photonics Journal,* 7**,** 1-8.

DYACHENKO, P. N., MOLESKY, S., PETROV, A. Y., STÖRMER, M., KREKELER, T., LANG, S., RITTER, M., JACOB, Z. & EICH, M. 2016. Controlling thermal emission with refractory epsilon-near-zero metamaterials via topological transitions. *Nature communications,* 7**,** 1-8.

EBBESEN, T. W., GENET, C. & BOZHEVOLNYI, S. I. 2008. Surface-plasmon circuitry. *Physics Today,* 61**,** 44.

ECONOMOU, E. 1969. Surface plasmons in thin films. *Physical review,* 182**,** 539.

EINSTEIN, A. 1905. The photoelectric effect. *Ann. Phys,* 17**,** 4.

ENOCH, S. & BONOD, N. 2012. *Plasmonics: from basics to advanced topics*, Springer.

ENOCH, S., SIMON, J.-J., ESCOUBAS, L., ELALMY, Z., LEMARQUIS, F., TORCHIO, P. & ALBRAND, G. J. A. P. L. 2005. Simple layer-by-layer photonic crystal for the control of thermal emission. 86**,** 261101.

FALLAHI, A. & PERRUISSEAU-CARRIER, J. 2012. Design of tunable biperiodic graphene metasurfaces. *Physical Review B,* 86**,** 195408.

FAN, G., SUN, K., HOU, Q., WANG, Z., LIU, Y. & FAN, R. 2021. Epsilon-negative media from the viewpoint of materials science. *EPJ Applied Metamaterials,* 8**,** 11.

FAN, S. 2017. Thermal photonics and energy applications. *Joule,* 1**,** 264-273.

FARHAT, M., GUENNEAU, S., ENOCH, S., MOVCHAN, A. B. & PETURSSON, G. G. 2010. Focussing bending waves via negative refraction in perforated thin plates. *Applied Physics Letters,* 96**,** 081909.

FAZARINC, Z. 2015. Fermi–Dirac, Bose–Einstein, Maxwell–Boltzmann, and computers. *Computer Applications in Engineering Education,* 23**,** 746-759.

FENG, L., TETZ, K. A., SLUTSKY, B., LOMAKIN, V. & FAINMAN, Y. 2007. Fourier plasmonics: Diffractive focusing of in-plane surface plasmon polariton waves. *Applied Physics Letters,* 91**,** 081101.

FLEMING, J., LIN, S., EL-KADY, I., BISWAS, R. & HO, K. J. N. 2002. All-metallic three-dimensional photonic crystals with a large infrared bandgap. 417**,** 52-55.

FLEURY, R. & ALU, A. Cloaking and invisibility: A review. Forum for Electromagnetic Research Methods and Application Technologies (FERMAT), 2014.

FOX, M. 2002. Optical properties of solids. American Association of Physics Teachers.

FRANKLIN, D., MODAK, S., VÁZQUEZ-GUARDADO, A., SAFAEI, A. & CHANDA, D. 2018. Covert infrared image encoding through imprinted plasmonic cavities. *Light: Science & Applications,* 7**,** 1-8.

GANSEL, J. K., THIEL, M., RILL, M. S., DECKER, M., BADE, K., SAILE, V., VON FREYMANN, G., LINDEN, S. & WEGENER, M. 2009. Gold helix photonic metamaterial as broadband circular polarizer. *science,* 325**,** 1513-1515.

GAO, J., SUN, L., DENG, H., MATHAI, C. J., GANGOPADHYAY, S. & YANG, X. 2013. Experimental realization of epsilon-near-zero metamaterial slabs with metal-dielectric multilayers. *Applied Physics Letters,* 103**,** 051111.

GARCIA-VIDAL, F. J., MARTIN-MORENO, L., EBBESEN, T. & KUIPERS, L. 2010. Light passing through subwavelength apertures. *Reviews of Modern Physics,* 82**,** 729.

GEIM, A. K. 2009. Graphene: status and prospects. *science,* 324**,** 1530-1534.

GHANEKAR, A., LIN, L. & ZHENG, Y. 2016. Novel and efficient Mie-metamaterial thermal emitter for thermophotovoltaic systems. *Optics express,* 24, A868-A877.

GHOSHAL, A. & KIK, P. G. 2008. Theory and simulation of surface plasmon excitation using resonant metal nanoparticle arrays. *Journal of Applied Physics,* 103, 113111.

GONG, Y., LIU, X., LI, K., HUANG, J., MARTINEZ, J., REES-WHIPPEY, D., CARVER, S., WANG, L., ZHANG, W. & DUAN, T. 2013a. Coherent emission of light using stacked gratings. *Physical Review B,* 87, 205121.

GONG, Y., LIU, X., LI, K., HUANG, J., MARTINEZ, J. J., REES-WHIPPEY, D., CARVER, S., WANG, L., ZHANG, W., DUAN, T. & COPNER, N. 2013b. Coherent emission of light using stacked gratings. *Physical Review B,* 87, 205121.

GONG, Y., WANG, Z., LI, K., UGGALLA, L., HUANG, J., COPNER, N., ZHOU, Y., QIAO, D. & ZHU, J. J. O. L. 2017. Highly efficient and broadband mid-infrared metamaterial thermal emitter for optical gas sensing. 42, 4537-4540.

GORDON, B. L. 2002. Maxwell–Boltzmann statistics and the metaphysics of modality. *Synthese,* 133, 393-417.

GORDON, R. & BROLO, A. G. 2005. Increased cut-off wavelength for a subwavelength hole in a real metal. *Optics Express,* 13, 1933-1938.

GOU, J., LIU, X., ZHANG, C., SUN, G., SHI, Y., WANG, J., CHEN, H., MA, T. & REN, X. 2018. Ferromagnetic composite with stress-insensitive magnetic permeability: Compensation of stress-induced anisotropies. *Physical Review Materials,* 2, 114406.

GRAMOTNEV, D. K. & BOZHEVOLNYI, S. I. J. N. P. 2010. Plasmonics beyond the diffraction limit. 4, 83.

GRBIC, A. & ELEFTHERIADES, G. V. 2002. Experimental verification of backward-wave radiation from a negative refractive index metamaterial. *Journal of applied physics,* 92, 5930-5935.

GREFFET, J.-J. 2011. Controlled incandescence. *Nature,* 478, 191.

GREFFET, J.-J., CARMINATI, R., JOULAIN, K., MULET, J.-P., MAINGUY, S. & CHEN, Y. 2002a. Coherent emission of light by thermal sources. *Nature,* 416, 61-64.

GREFFET, J.-J., CARMINATI, R., JOULAIN, K., MULET, J.-P., MAINGUY, S. & CHEN, Y. J. N. 2002b. Coherent emission of light by thermal sources. 416, 61.

GRIGORENKO, A., NIKITIN, P. & KABASHIN, A. 1999. Phase jumps and interferometric surface plasmon resonance imaging. *Applied Physics Letters,* 75, 3917-3919.

GRIGORENKO, A. N., POLINI, M. & NOVOSELOV, K. 2012. Graphene plasmonics. *Nature photonics,* 6, 749-758.

GRISCOM, D. L. 1991. Optical properties and structure of defects in silica glass. *Journal of the Ceramic Society of Japan,* 99, 923-942.

GU, Y., KWAK, E.-S., LENSCH, J., ALLEN, J., ODOM, T. W. & LAUHON, L. J. 2005. Near-field scanning photocurrent microscopy of a nanowire photodetector. *Applied Physics Letters,* 87, 043111.

GUHA, B., OTEY, C., POITRAS, C. B., FAN, S. & LIPSON, M. 2012. Near-field radiative cooling of nanostructures. *Nano letters,* 12, 4546-4550.

GUO, Q., CUI, Y., YAO, Y., YE, Y., YANG, Y., LIU, X., ZHANG, S., LIU, X., QIU, J. & HOSONO, H. 2017. A solution-processed ultrafast optical switch based on a nanostructured epsilon-near-zero medium. *Advanced Materials,* 29, 1700754.

HAN, S. E., STEIN, A. & NORRIS, D. J. 2007. Tailoring self-assembled metallic photonic crystals for modified thermal emission. *Physical review letters,* 99, 053906.

HAN, T., BAI, X., THONG, J. T., LI, B. & QIU, C. W. 2014. Full control and manipulation of heat signatures: cloaking, camouflage and thermal metamaterials. *Advanced Materials,* 26, 1731-1734.

HARADA, K., MUNAKATA, K., ITOH, M., YATAGAI, T., HONDA, Y. & UMEGAKI, S. 2000. High-speed light modulation using complex refractive-index changes of electro-optic polymers. *Applied Physics Letters,* 77, 3683-3685.

HARMS, P., MITTRA, R. & KO, W. 1994. Implementation of the periodic boundary condition in the finite-difference time-domain algorithm for FSS structures. *IEEE transactions on antennas propagation,* 42**,** 1317-1324.

HAYDEN, O., AGARWAL, R. & LIEBER, C. M. 2006. Nanoscale avalanche photodiodes for highly sensitive and spatially resolved photon detection. *Nature materials,* 5**,** 352-356.

HEINZEL, A., BOERNER, V., GOMBERT, A., BLÄSI, B., WITTWER, V. & LUTHER, J. 2000. Radiation filters and emitters for the NIR based on periodically structured metal surfaces. *Journal of Modern Optics,* 47**,** 2399-2419.

HENTSCHEL, M., METZGER, B., KNABE, B., BUSE, K. & GIESSEN, H. 2016. Linear and nonlinear optical properties of hybrid metallic–dielectric plasmonic nanoantennas. *Beilstein journal of nanotechnology,* 7**,** 111-120.

HILL, A., MIKHAILOV, S. A. & ZIEGLER, K. 2009. Dielectric function and plasmons in graphene. *EPL (Europhysics Letters),* 87**,** 27005.

HOFFMAN, A. & GMACHL, C. 2012. Extending opportunities. *Nat. Photonics,* 6**,** 407.

HONG, S., SHIN, S. & CHEN, R. 2020. An adaptive and wearable thermal camouflage device. *Advanced Functional Materials,* 30**,** 1909788.

HSU, P.-C., SONG, A. Y., CATRYSSE, P. B., LIU, C., PENG, Y., XIE, J., FAN, S. & CUI, Y. 2016. Radiative human body cooling by nanoporous polyethylene textile. *Science,* 353**,** 1019-1023.

HUANG, J., DU, P., HONG, L., DONG, Y. & HONG, M. 2007. A novel percolative ferromagnetic–ferroelectric composite with significant dielectric and magnetic properties. *Advanced Materials,* 19**,** 437-440.

HUBER, A., DEUTSCH, B., NOVOTNY, L. & HILLENBRAND, R. 2008. Focusing of surface phonon polaritons. *Applied Physics Letters,* 92**,** 203104.

HUTTER, E. & FENDLER, J. H. 2004. Exploitation of localized surface plasmon resonance. *Advanced materials,* 16**,** 1685-1706.

IKEDA, K., MIYAZAKI, H., KASAYA, T., YAMAMOTO, K., INOUE, Y., FUJIMURA, K., KANAKUGI, T., OKADA, M., HATADE, K. & KITAGAWA, S. J. A. P. L. 2008. Controlled thermal emission of polarized infrared waves from arrayed plasmon nanocavities. 92**,** 021117.

ILIC, O., JABLAN, M., JOANNOPOULOS, J. D., CELANOVIC, I. & SOLJAČIĆ, M. 2012. Overcoming the black body limit in plasmonic and graphene near-field thermophotovoltaic systems. *Optics express,* 20**,** A366-A384.

INOUE, T., DE ZOYSA, M., ASANO, T. & NODA, S. 2015. Realization of narrowband thermal emission with optical nanostructures. *Optica,* 2**,** 27-35.

INOUE, T., DE ZOYSA, M., ASANO, T. & NODA, S. J. A. P. L. 2016. On-chip integration and high-speed switching of multi-wavelength narrowband thermal emitters. 108**,** 091101.

IYER, A. K. & ELEFTHERIADES, G. V. Negative refractive index metamaterials supporting 2-D waves. 2002 IEEE MTT-S International Microwave Symposium Digest (Cat. No. 02CH37278), 2002. IEEE, 1067-1070.

JABLAN, M., BULJAN, H. & SOLJAČIĆ, M. 2009. Plasmonics in graphene at infrared frequencies. *Physical review B,* 80**,** 245435.

JI, D., SONG, H., ZENG, X., HU, H., LIU, K., ZHANG, N. & GAN, Q. 2014. Broadband absorption engineering of hyperbolic metafilm patterns. *Scientific reports,* 4**,** 1-7.

JOANNOPOULOS, J. D., JOHNSON, S. G., WINN, J. N. & MEADE, R. D. 2008. Molding the flow of light. *Princeton Univ. Press, Princeton, NJ [ua]*.

JOHNSON, P. B. & CHRISTY, R.-W. 1972. Optical constants of the noble metals. *Physical review B,* 6**,** 4370.

JU, L., GENG, B., HORNG, J., GIRIT, C., MARTIN, M., HAO, Z., BECHTEL, H. A., LIANG, X., ZETTL, A. & SHEN, Y. R. 2011. Graphene plasmonics for tunable terahertz metamaterials. *Nature nanotechnology,* 6**,** 630-634.

JUNG, D., BANK, S., LEE, M. L. & WASSERMAN, D. 2017. Next-generation mid-infrared sources. *Journal of Optics,* 19**,** 123001.

KABASHIN, A. V., PATSKOVSKY, S. & GRIGORENKO, A. N. 2009. Phase and amplitude sensitivities in surface plasmon resonance bio and chemical sensing. *Optics Express,* 17**,** 21191-21204.

KAJIHARA, K. 2007. Improvement of vacuum-ultraviolet transparency of silica glass by modification of point defects. *Journal of the Ceramic Society of Japan,* 115**,** 85-91.

KAN, Y., ZHAO, C., FANG, X. & WANG, B. 2017. Designing ultrabroadband absorbers based on Bloch theorem and optical topological transition. *Optics Letters,* 42**,** 1879-1882.

KITTEL, A., MÜLLER-HIRSCH, W., PARISI, J., BIEHS, S.-A., REDDIG, D. & HOLTHAUS, M. 2005. Near-Field Heat Transfer in a Scanning Thermal Microscope. *Physical Review Letters,* 95**,** 224301.

KLAR, T. A., KILDISHEV, A. V., DRACHEV, V. P. & SHALAEV, V. M. 2006. Negative-index metamaterials: going optical. *IEEE Journal of Selected Topics in Quantum Electronics,* 12**,** 1106-1115.

KOCK, W. E. 1946. Metal-lens antennas. *Proceedings of the IRE,* 34**,** 828-836.

KOECHLIN, C., BOUCHON, P., PARDO, F., PELOUARD, J.-L. & HAÏDAR, R. 2013. Analytical description of subwavelength plasmonic MIM resonators and of their combination. *Optics express,* 21**,** 7025-32.

KOHIYAMA, A., SHIMIZU, M., IGUCHI, F. & YUGAMI, H. 2015. Narrowband thermal radiation from closed-end microcavities. *Journal of Applied Physics,* 118**,** 133102.

KONG, J., SUN, T., CAO, F., LI, Y., BAO, J., GAO, J., WANG, X., ZHOU, G., GUO, C. & REN, Z. 2018. A Metamaterial-Plasmonic Scheme Based on a Random Metallic Network for Controlling Thermal Emission. *physica status solidi (a),* 215**,** 1800206.

KONG, J. A. 2002. Electromagnetic wave interaction with stratified negative isotropic media. *Progress In Electromagnetics Research,* 35**,** 1-52.

KOPPENS, F. H., CHANG, D. E. & GARCÍA DE ABAJO, F. J. 2011. Graphene plasmonics: a platform for strong light–matter interactions. *Nano letters,* 11**,** 3370-3377.

KRASAVIN, A. V. & ZAYATS, A. V. 2015. Active Nanophotonic Circuitry Based on Dielectric-loaded Plasmonic Waveguides. *Advanced Optical Materials,* 3**,** 1662-1690.

KRASAVIN, A. V. & ZHELUDEV, N. 2004. Active plasmonics: Controlling signals in Au/Ga waveguide using nanoscale structural transformations. *Applied Physics Letters,* 84**,** 1416-1418.

KREIBIG, U. & VOLLMER, M. 2013. *Optical properties of metal clusters*, Springer Science & Business Media.

KRETSCHMANN, E. & RAETHER, H. 1968. Radiative decay of non radiative surface plasmons excited by light. *Zeitschrift für Naturforschung A,* 23**,** 2135-2136.

KSHETRIMAYUM, R. S. 2005. A brief intro to metamaterials. *IEEE Potentials,* 23**,** 44-46.

LAL, S., LINK, S. & HALAS, N. J. 2007. Nano-optics from sensing to waveguiding. *Nature photonics,* 1**,** 641-648.

LANDY, N. I., SAJUYIGBE, S., MOCK, J. J., SMITH, D. R. & PADILLA, W. J. 2008a. Perfect metamaterial absorber. *Physical review letters,* 100**,** 207402.

LANDY, N. I., SAJUYIGBE, S., MOCK, J. J., SMITH, D. R. & PADILLA, W. J. J. P. R. L. 2008b. Perfect metamaterial absorber. 100**,** 207402.

LANG, F., WANG, H., ZHANG, S., LIU, J. & YAN, H. 2018. Review on variable emissivity materials and devices based on smart chromism. *International Journal of Thermophysics,* 39**,** 1-20.

LAROCHE, M., CARMINATI, R. & GREFFET, J.-J. 2006. Coherent thermal antenna using a photonic crystal slab. *Physical review letters,* 96**,** 123903.

LAW, M., GREENE, L. E., JOHNSON, J. C., SAYKALLY, R. & YANG, P. 2005. Nanowire dye-sensitized solar cells. *Nature materials,* 4**,** 455-459.

LEE, B., FU, C. & ZHANG, Z. 2005. Coherent thermal emission from one-dimensional photonic crystals. *Applied Physics Letters,* 87**,** 071904.

LEMIEUX, S., GIESE, E., FICKLER, R., CHEKHOVA, M. V. & BOYD, R. W. 2019. A primary radiation standard based on quantum nonlinear optics. *Nature Physics,* 15**,** 529-532.

LEMOULT, F., KAINA, N., FINK, M. & LEROSEY, G. 2013. Wave propagation control at the deep subwavelength scale in metamaterials. *Nature Physics,* 9**,** 55-60.

LENERT, A., BIERMAN, D. M., NAM, Y., CHAN, W. R., CELANOVIĆ, I., SOLJAČIĆ, M. & WANG, E. N. 2014. A nanophotonic solar thermophotovoltaic device. *Nature nanotechnology,* 9**,** 126-130.

LI, P., WANG, Y., GUPTA, U., LIU, J., ZHANG, L., DU, D., FOO, C. C., OUYANG, J. & ZHU, J. 2019. Transparent soft robots for effective camouflage. *Advanced Functional Materials,* 29**,** 1901908.

LI, R., CHENG, C., REN, F.-F., CHEN, J., FAN, Y.-X., DING, J. & WANG, H.-T. 2008. Hybridized surface plasmon polaritons at an interface between a metal and a uniaxial crystal. *Applied Physics Letters,* 92**,** 141115.

LI, W. & FAN, S. J. O. E. 2018. Nanophotonic control of thermal radiation for energy applications. 26**,** 15995-16021.

LI, W., GULER, U., KINSEY, N., NAIK, G. V., BOLTASSEVA, A., GUAN, J., SHALAEV, V. M. & KILDISHEV, A. V. J. A. M. 2014. Refractory plasmonics with titanium nitride: broadband metamaterial absorber. 26**,** 7959-7965.

LI, W. & VALENTINE, J. J. N. L. 2014. Metamaterial perfect absorber based hot electron photodetection. 14**,** 3510-3514.

LI, Y., BAI, X., YANG, T., LUO, H. & QIU, C.-W. 2018. Structured thermal surface for radiative camouflage. *Nature communications,* 9**,** 1-7.

LI, Y. & ZHU, W. 2018. Common Complications of Surgery for Crohn's Disease and Ulcerative Colitis. *Interventional Inflammatory Bowel Disease: Endoscopic Management and Treatment of Complications.* Elsevier.

LI, Z. & YU, N. 2013. Modulation of mid-infrared light using graphene-metal plasmonic antennas. *Applied Physics Letters,* 102**,** 131108.

LIANG, D. & BOWERS, J. E. 2010. Recent progress in lasers on silicon. *Nature photonics,* 4**,** 511-517.

LIN, S.-Y., MORENO, J. & FLEMING, J. 2003a. Three-dimensional photonic-crystal emitter for thermal photovoltaic power generation. *Applied physics letters,* 83**,** 380-382.

LIN, S.-Y., MORENO, J. & FLEMING, J. J. A. P. L. 2003b. Three-dimensional photonic-crystal emitter for thermal photovoltaic power generation. 83**,** 380-382.

LIU, N., MESCH, M., WEISS, T., HENTSCHEL, M. & GIESSEN, H. J. N. L. 2010a. Infrared perfect absorber and its application as plasmonic sensor. 10**,** 2342-2348.

LIU, X., STARR, T., STARR, A. F. & PADILLA, W. J. 2010b. Infrared spatial and frequency selective metamaterial with near-unity absorbance. *Physical review letters,* 104**,** 207403.

LIU, X., TYLER, T., STARR, T., STARR, A. F., JOKERST, N. M. & PADILLA, W. J. 2011a. Taming the Blackbody with Infrared Metamaterials as Selective Thermal Emitters. *Physical Review Letters,* 107**,** 045901.

LIU, X., TYLER, T., STARR, T., STARR, A. F., JOKERST, N. M. & PADILLA, W. J. J. P. R. L. 2011b. Taming the blackbody with infrared metamaterials as selective thermal emitters. 107**,** 045901.

LIU, Z., STEELE, J. M., SRITURAVANICH, W., PIKUS, Y., SUN, C. & ZHANG, X. 2005. Focusing surface plasmons with a plasmonic lens. *Nano letters,* 5**,** 1726-1729.

LOCHBAUM, A., DORODNYY, A., KOCH, U., KOEPFLI, S. M., VOLK, S., FEDORYSHYN, Y., WOOD, V. & LEUTHOLD, J. 2020. Compact Mid-Infrared Gas Sensing Enabled by an All-Metamaterial Design. *Nano Letters,* 20**,** 4169-4176.

LOCHBAUM, A., FEDORYSHYN, Y., DORODNYY, A., KOCH, U., HAFNER, C. & LEUTHOLD, J. 2017a. On-Chip Narrowband Thermal Emitter for Mid-IR Optical Gas Sensing. *ACS Photonics,* 4**,** 1371-1380.

LOCHBAUM, A., FEDORYSHYN, Y., DORODNYY, A., KOCH, U., HAFNER, C. & LEUTHOLD, J. J. A. P. 2017b. On-chip narrowband thermal emitter for mid-IR optical gas sensing. 4**,** 1371-1380.

LÓPEZ-TEJEIRA, F., RODRIGO, S. G., MARTIN-MORENO, L., GARCÍA-VIDAL, F. J., DEVAUX, E., EBBESEN, T. W., KRENN, J. R., RADKO, I., BOZHEVOLNYI, S. I. & GONZÁLEZ, M. U. 2007. Efficient unidirectional nanoslit couplers for surface plasmons. *Nature Physics,* 3**,** 324-328.

LYU, J., LIU, Z., WU, X., LI, G., FANG, D. & ZHANG, X. 2019. Nanofibrous kevlar aerogel films and their phase-change composites for highly efficient infrared stealth. *ACS nano,* 13**,** 2236-2245.

MACDONALD, K. F. & ZHELUDEV, N. I. 2010. Active plasmonics: current status. *Laser & Photonics Reviews,* 4**,** 562-567.

MAIER, S. A. 2007. *Plasmonics: fundamentals and applications*, Springer.

MAIER, T. & BRÜCKL, H. 2009. Wavelength-tunable microbolometers with metamaterial absorbers. *Optics letters,* 34, 3012-3014.

MAIER, T. & BRUECKL, H. 2010. Multispectral microbolometers for the midinfrared. *Optics letters,* 35**,** 3766-3768.

MAKHSIYAN, M., BOUCHON, P., JAECK, J., PELOUARD, J.-L. & HAÏDAR, R. J. A. P. L. 2015. Shaping the spatial and spectral emissivity at the diffraction limit. 107**,** 251103.

MATSUNO, Y. & SAKURAI, A. 2017. Perfect infrared absorber and emitter based on a large-area metasurface. *Optical Materials Express,* 7**,** 618-626.

MEHDIZADEH, F., ALIPOUR-BANAEI, H. & DAIE-KUZEKANANI, Z. 2012. All optical multi reflection structure based on one dimensional photonic crystals for WDM communication systems. *Optoelectronics and Advanced Materials-Rapid Communications,* 6**,** 527-531.

MESSINA, R. & BEN-ABDALLAH, P. 2013. Graphene-based photovoltaic cells for near-field thermal energy conversion. *Scientific reports,* 3**,** 1-5.

MEZZANOTTE, P., ROSELLI, L. & SORRENTINO, R. 1995. A simple way to model curved metal boundaries in FDTD algorithm avoiding staircase approximation. *IEEE microwave guided wave letters,* 5**,** 267-269.

MIKHAILOV, S. A. 2011. Theory of the giant plasmon-enhanced second-harmonic generation in graphene and semiconductor two-dimensional electron systems. *Physical Review B,* 84**,** 045432.

MIKHAILOV, S. A. & ZIEGLER, K. 2007. New electromagnetic mode in graphene. *Physical review letters,* 99**,** 016803.

MIYOSHI, Y., FUKAZAWA, Y., AMASAKA, Y., RECKMANN, R., YOKOI, T., ISHIDA, K., KAWAHARA, K., AGO, H. & MAKI, H. J. N. C. 2018. High-speed and on-chip graphene blackbody emitters for optical communications by remote heat transfer. 9**,** 1-9.

MIZOGUCHI, T., FINDLAY, S. D., MASUNO, A., SAITO, Y., YAMAGUCHI, K., INOUE, H. & IKUHARA, Y. 2013. Atomic-scale identification of individual lanthanide dopants in optical glass fiber. *ACS nano,* 7**,** 5058-5063.

MOORE, G. E. 1998. Cramming more components onto integrated circuits. *Proceedings of the IEEE,* 86**,** 82-85.

MORI, T., YAMAUCHI, Y., HONDA, S. & MAKI, H. 2014. An electrically driven, ultrahigh-speed, on-chip light emitter based on carbon nanotubes. *Nano letters,* 14**,** 3277-3283.

MORIN, S. A., SHEPHERD, R. F., KWOK, S. W., STOKES, A. A., NEMIROSKI, A. & WHITESIDES, G. M. 2012. Camouflage and display for soft machines. *Science,* 337**,** 828-832.

MURPHY, C. J., GOLE, A. M., STONE, J. W., SISCO, P. N., ALKILANY, A. M., GOLDSMITH, E. C. & BAXTER, S. C. 2008. Gold nanoparticles in biology: beyond toxicity to cellular imaging. *Accounts of chemical research,* 41**,** 1721-1730.

NARAYANASWAMY, A. & CHEN, G. 2003. Surface modes for near field thermophotovoltaics. *Applied Physics Letters,* 82**,** 3544-3546.

NARAYANASWAMY, A. & CHEN, G. 2004. Thermal emission control with one-dimensional metallodielectric photonic crystals. *Physical Review B,* 70**,** 125101.

NEFEDOV, I. S. & MELNIKOV, L. A. 2014. Super-Planckian far-zone thermal emission from asymmetric hyperbolic metamaterials. *Applied Physics Letters,* 105**,** 161902.

NEUTENS, P., VAN DORPE, P., DE VLAMINCK, I., LAGAE, L. & BORGHS, G. 2009. Electrical detection of confined gap plasmons in metal–insulator–metal waveguides. *Nature Photonics,* 3**,** 283-286.

NICOLAS, R., LÉVÊQUE, G., MARAE-DJOUDA, J., MONTAY, G., MADI, Y., PLAIN, J., HERRO, Z., KAZAN, M., ADAM, P.-M. & MAURER, T. 2015. Plasmonic mode interferences and Fano resonances in Metal-Insulator-Metal nanostructured interface. *Scientific reports,* 5**,** 1-11.

NOVOSELOV, K. S., COLOMBO, L., GELLERT, P., SCHWAB, M. & KIM, K. 2012. A roadmap for graphene. *nature,* 490**,** 192-200.

OTEY, C. R., LAU, W. T. & FAN, S. 2010. Thermal Rectification through Vacuum. *Physical Review Letters,* 104**,** 154301.

OTTO, A. 1968. Excitation of nonradiative surface plasma waves in silver by the method of frustrated total reflection. *Zeitschrift für Physik A Hadrons and nuclei,* 216**,** 398-410.

OZBAY, E. 2006. Plasmonics: Merging Photonics and Electronics at Nanoscale Dimensions. *Science,* 311**,** 189.

PADILLA, W. J., BASOV, D. N. & SMITH, D. R. 2006. Negative refractive index metamaterials. *Materials today,* 9**,** 28-35.

PALIK, E. D. 1998. *Handbook of optical constants of solids*, Academic press.

PARAZZOLI, C., GREEGOR, R., LI, K., KOLTENBAH, B. & TANIELIAN, M. 2003. Experimental verification and simulation of negative index of refraction using Snell's law. *Physical Review Letters,* 90**,** 107401.

PENDRY, J. B. 2000. Negative refraction makes a perfect lens. *Physical review letters,* 85**,** 3966.

PENDRY, J. B., HOLDEN, A., STEWART, W. & YOUNGS, I. 1996. Extremely low frequency plasmons in metallic mesostructures. *Physical review letters,* 76**,** 4773.

PHAN, L., WALKUP IV, W. G., ORDINARIO, D. D., KARSHALEV, E., JOCSON, J. M., BURKE, A. M. & GORODETSKY, A. A. 2013. Reconfigurable infrared camouflage coatings from a cephalopod protein. *Advanced Materials,* 25**,** 5621-5625.

PLANCK, M. 1901. On the law of distribution of energy in the normal spectrum. *Annalen der physik,* 4**,** 1.

PLANCK, M. 1978. Über das gesetz der energieverteilung im normalspektrum. *Von Kirchhoff bis Planck.* Springer.

POLDERVAART, L. & SLUIJTER, C. 1975. Photonics: the profile of a new discipline. *High Speed Photography.* Springer.

PRALLE, M., MOELDERS, N., MCNEAL, M., PUSCASU, I., GREENWALD, A., DALY, J., JOHNSON, E., GEORGE, T., CHOI, D. & EL-KADY, I. 2002. Photonic crystal enhanced narrow-band infrared emitters. *Applied Physics Letters,* 81**,** 4685-4687.

PROTECTION, I. C. O. N.-I. R. 2013. ICNIRP guidelines on limits of exposure to incoherent visible and infrared radiation. *Health Physics,* 105**,** 74-96.

QU, Y., LI, Q., CAI, L., PAN, M., GHOSH, P., DU, K. & QIU, M. 2018. Thermal camouflage based on the phase-changing material GST. *Light: Science & Applications,* 7**,** 1-10.

QU, Y., LI, Q., GONG, H., DU, K., BAI, S., ZHAO, D., YE, H. & QIU, M. 2016a. Spatially and spectrally resolved narrowband optical absorber based on 2D grating nanostructures on metallic films. *Advanced Optical Materials,* 4**,** 480-486.

QU, Y., LI, Q., GONG, H., DU, K., BAI, S., ZHAO, D., YE, H. & QIU, M. J. A. O. M. 2016b. Spatially and spectrally resolved narrowband optical absorber based on 2D grating nanostructures on metallic films. 4**,** 480-486.

RAETHER, H. 1988a. Surface plasmons on gratings. *Surface plasmons on smooth and rough surfaces and on gratings***,** 91-116.

RAETHER, H. 1988b. Surface plasmons on smooth surfaces. *Surface plasmons on smooth and rough surfaces and on gratings.* Springer.

RAETHER, H. 1988c. Surface plasmons on smooth surfaces. *Surface plasmons on smooth and rough surfaces and on gratings***,** 4-39.

RICHARDS, P. 1994. Bolometers for infrared and millimeter waves. *Journal of Applied Physics,* 76**,** 1-24.

RING, E. & AMMER, K. 2012. Infrared thermal imaging in medicine. *Physiological measurement,* 33**,** R33.

RINNERBAUER, V., LENERT, A., BIERMAN, D. M., YENG, Y. X., CHAN, W. R., GEIL, R. D., SENKEVICH, J. J., JOANNOPOULOS, J. D., WANG, E. N. & SOLJAČIĆ, M. J. A. E. M. 2014. Metallic photonic

crystal absorber-emitter for efficient spectral control in high-temperature solar thermophotovoltaics. 4**,** 1400334.

RITCHIE, R. H. 1957. Plasma losses by fast electrons in thin films. *Physical review,* 106**,** 874.

RIVERA, V., FERRI, F. & MAREGA JR, E. 2012. Localized surface plasmon resonances: noble metal nanoparticle interaction with rare-earth ions. *Plasmonics-Principles and Applications***,** 283-312.

ROBINSON, S. & NAKKEERAN, R. 2012. Investigation on two dimensional photonic crystal resonant cavity based bandpass filter. *Optik,* 123**,** 451-457.

ROSTAMI, A., BANAEI, H. A., NAZARI, F. & BAHRAMI, A. 2011. An ultra compact photonic crystal wavelength division demultiplexer using resonance cavities in a modified Y-branch structure. *Optik,* 122**,** 1481-1485.

RYCENGA, M., COBLEY, C. M., ZENG, J., LI, W., MORAN, C. H., ZHANG, Q., QIN, D. & XIA, Y. 2011. Controlling the synthesis and assembly of silver nanostructures for plasmonic applications. *Chemical reviews,* 111**,** 3669-3712.

SAHA, K., AGASTI, S. S., KIM, C., LI, X. & ROTELLO, V. M. 2012. Gold nanoparticles in chemical and biological sensing. *Chemical reviews,* 112**,** 2739-2779.

SAI, H., KANAMORI, Y. & YUGAMI, H. 2005. Tuning of the thermal radiation spectrum in the near-infrared region by metallic surface microstructures. *Journal of Micromechanics and Microengineering,* 15**,** S243.

SAI, H., KANAMORI, Y. & YUGAMI, H. J. A. P. L. 2003. High-temperature resistive surface grating for spectral control of thermal radiation. 82**,** 1685-1687.

SAI, H. & YUGAMI, H. 2004. *Thermophotovoltaic generation with selective radiators based on tungsten surface gratings*.

SAI, H., YUGAMI, H., AKIYAMA, Y., KANAMORI, Y. & HANE, K. 2001. Spectral control of thermal emission by periodic microstructured surfaces in the near-infrared region. *JOSA A,* 18**,** 1471-1476.

SAKAT, E., WOJSZVZYK, L., HUGONIN, J.-P., BESBES, M., SAUVAN, C. & GREFFET, J.-J. J. O. 2018. Enhancing thermal radiation with nanoantennas to create infrared sources with high modulation rates. 5**,** 175-179.

SCHULLER, J. A., BARNARD, E. S., CAI, W., JUN, Y. C., WHITE, J. S. & BRONGERSMA, M. L. 2010. Plasmonics for extreme light concentration and manipulation. *Nature materials,* 9**,** 193-204.

SHALAEV, V. M. 2008. Metamaterials: A new paradigm of physics and engineering. *Chapter2, https://nanohub. org/resources/4262*.

SHARMA, A. K. & GUPTA, B. 2005. Fiber optic sensor based on surface plasmon resonance with nanoparticle films. *Photonics and Nanostructures-Fundamentals and Applications,* 3**,** 30-37.

SHELBY, R. A., SMITH, D. R. & SCHULTZ, S. 2001. Experimental verification of a negative index of refraction. *science,* 292**,** 77-79.

SHREKENHAMER, D., CHEN, W.-C. & PADILLA, W. J. J. P. R. L. 2013. Liquid crystal tunable metamaterial absorber. 110**,** 177403.

SINCERBOX, G. T. & GORDON, J. C. 1981. Small fast large-aperture light modulator using attenuated total reflection. *Applied optics,* 20**,** 1491-1496.

SLEPYAN, G. Y., MAKSIMENKO, S., LAKHTAKIA, A., YEVTUSHENKO, O. & GUSAKOV, A. 1999. Electrodynamics of carbon nanotubes: Dynamic conductivity, impedance boundary conditions, and surface wave propagation. *Physical Review B,* 60**,** 17136.

SMITH, D. R., PADILLA, W. J., VIER, D., NEMAT-NASSER, S. C. & SCHULTZ, S. 2000. Composite medium with simultaneously negative permeability and permittivity. *Physical review letters,* 84**,** 4184.

SOMMERFELD, A. 1928. Zur Elektronentheorie der Metalle. *Naturwissenschaften,* 16**,** 374-381.

SOREF, R. 2010. Mid-infrared photonics in silicon and germanium. *Nature photonics,* 4**,** 495-497.

SORGER, V. J., OULTON, R. F., MA, R.-M. & ZHANG, X. 2012. Toward integrated plasmonic circuits. *MRS bulletin,* 37**,** 728-738.

SOUKOULIS, C. M., KAFESAKI, M. & ECONOMOU, E. N. 2006. Negative-Index Materials: New Frontiers in Optics. *Advanced materials,* 18**,** 1941-1952.

SOUKOULIS, C. M. & WEGENER, M. 2010. Optical metamaterials—more bulky and less lossy. *Science,* 330**,** 1633-1634.

SPADAVECCHIA, J., APCHAIN, E., ALBÉRIC, M., FONTAN, E. & REICHE, I. 2014. One-Step Synthesis of Collagen Hybrid Gold Nanoparticles and Formation on Egyptian-like Gold-Plated Archaeological Ivory. *Angewandte Chemie,* 126**,** 8503-8506.

STANLEY, R. 2012. Plasmonics in the mid-infrared. *Nature Photonics,* 6**,** 409-411.

SUGINO, C., LEADENHAM, S., RUZZENE, M. & ERTURK, A. 2016. On the mechanism of bandgap formation in locally resonant finite elastic metamaterials. *Journal of Applied Physics,* 120**,** 134501.

SUI, N. 2012. *Synthesis, characterization and optical properties of hybrid nanoparticles working with plasmon-fluorescence coupling.* Ecully, Ecole centrale de Lyon.

SUTHERLAND, R. L. 2003. *Handbook of nonlinear optics*, CRC press.

SVEDBERG, E. 2012. Harnessing Light: Capitalizing on Optical Science Trends and Challenges for Future Research.

TABOR, C. E. 2009. *Some optical and catalytic properties of metallic nanoparticles*, Georgia Institute of Technology.

TAFLOVE, A., HAGNESS, S. C. & PIKET-MAY, M. 2005. Computational electromagnetics: the finite-difference time-domain method. *The Electrical Engineering Handbook.*

TEDAH, I. A. O., MACULEWICZ, F., WOLF, D. E. & SCHMECHEL, R. 2019. Thermoelectrics versus thermophotovoltaics: Two approaches to convert heat fluxes into electricity. *Journal of Physics D: Applied Physics,* 52**,** 275501.

TEPERIK, T., ARCHAMBAULT, A., MARQUIER, F. & GREFFET, J.-J. 2009. Huygens-Fresnel principle for surface plasmons. *Optics express,* 17**,** 17483-17490.

TIAN, B., ZHENG, X., KEMPA, T. J., FANG, Y., YU, N., YU, G., HUANG, J. & LIEBER, C. M. 2007. Coaxial silicon nanowires as solar cells and nanoelectronic power sources. *nature,* 449**,** 885-889.

TITTL, A., MAI, P., TAUBERT, R., DREGELY, D., LIU, N. & GIESSEN, H. J. N. L. 2011. Palladium-based plasmonic perfect absorber in the visible wavelength range and its application to hydrogen sensing. 11**,** 4366-4369.

TITTL, A., MICHEL, A. K. U., SCHÄFERLING, M., YIN, X., GHOLIPOUR, B., CUI, L., WUTTIG, M., TAUBNER, T., NEUBRECH, F. & GIESSEN, H. J. A. M. 2015. A switchable mid-infrared plasmonic perfect absorber with multispectral thermal imaging capability. 27**,** 4597-4603.

TRÜGLER, A. 2011. *Optical properties of metallic nanoparticles*, Springer.

VASA, P., WANG, W., POMRAENKE, R., MAIURI, M., MANZONI, C., CERULLO, G. & LIENAU, C. Active plasmonics: merging metals with semiconductors. Ultrafast Phenomena and Nanophotonics XVIII, 2014. International Society for Optics and Photonics, 898409.

VESELAGO, V. G. 1968. The electrodynamics of substances with simultaneously negative values of img align= absmiddle Alt= ε Eps/Img and μ. *Physics-Uspekhi,* 10**,** 509-514.

WANG, F., ZHANG, Y., TIAN, C., GIRIT, C., ZETTL, A., CROMMIE, M. & SHEN, Y. R. 2008. Gate-variable optical transitions in graphene. *science,* 320**,** 206-209.

WANG, G., CHEN, X., LIU, S., WONG, C. & CHU, S. 2016. Mechanical chameleon through dynamic real-time plasmonic tuning. *Acs Nano,* 10**,** 1788-1794.

WANG, Y. & WU, J. 2016. Radiative heat transfer between nanoparticles enhanced by intermediate particle. *AIP Advances,* 6**,** 025104.

WILLETS, K. A. & VAN DUYNE, R. P. 2007. Localized surface plasmon resonance spectroscopy and sensing. *Annual review of physical chemistry,* 58**,** 267-297.

WOOLF, D. N., KADLEC, E. A., BETHKE, D., GRINE, A. D., NOGAN, J. J., CEDERBERG, J. G., BURCKEL, D. B., LUK, T. S., SHANER, E. A. & HENSLEY, J. M. J. O. 2018. High-efficiency thermophotovoltaic energy conversion enabled by a metamaterial selective emitter. 5**,** 213-218.

WRIGHT, A. & ZHANG, C. 2010. Dynamic conductivity of graphene with electron-LO-phonon interaction. *Physical Review B,* 81**,** 165413.

XIAO, S., CHETTIAR, U. K., KILDISHEV, A. V., DRACHEV, V. P. & SHALAEV, V. M. 2009. Yellow-light negative-index metamaterials. *Optics Letters,* 34**,** 3478-3480.

XU, H., BJERNELD, E. J., KÄLL, M. & BÖRJESSON, L. 1999. Spectroscopy of single hemoglobin molecules by surface enhanced Raman scattering. *Physical review letters,* 83**,** 4357.

XU, T., WU, Y.-K., LUO, X. & GUO, L. J. J. N. C. 2010. Plasmonic nanoresonators for high-resolution colour filtering and spectral imaging. 1**,** 59.

YAN, H., LI, X., CHANDRA, B., TULEVSKI, G., WU, Y., FREITAG, M., ZHU, W., AVOURIS, P. & XIA, F. 2012. Tunable infrared plasmonic devices using graphene/insulator stacks. *Nature nanotechnology,* 7**,** 330-334.

YAO, Y., SHANKAR, R., KATS, M. A., SONG, Y., KONG, J., LONCAR, M. & CAPASSO, F. J. N. L. 2014. Electrically tunable metasurface perfect absorbers for ultrathin mid-infrared optical modulators. 14**,** 6526-6532.

YEE, K. 1966. Numerical solution of initial boundary value problems involving Maxwell's equations in isotropic media. *IEEE Transactions on antennas and propagation,* 14**,** 302-307.

YIN, L., VLASKO-VLASOV, V. K., PEARSON, J., HILLER, J. M., HUA, J., WELP, U., BROWN, D. E. & KIMBALL, C. W. 2005. Subwavelength focusing and guiding of surface plasmons. *Nano letters,* 5**,** 1399-1402.

YU, C., LI, Y., ZHANG, X., HUANG, X., MALYARCHUK, V., WANG, S., SHI, Y., GAO, L., SU, Y. & ZHANG, Y. 2014. Adaptive optoelectronic camouflage systems with designs inspired by cephalopod skins. *Proceedings of the National Academy of Sciences,* 111**,** 12998-13003.

YU, N., WANG, Q. & CAPASSO, F. 2012. Beam engineering of quantum cascade lasers. *Laser & Photonics Reviews,* 6**,** 24-46.

ZAYATS, A. V., SMOLYANINOV, I. I. & MARADUDIN, A. A. 2005. Nano-optics of surface plasmon polaritons. *Physics reports,* 408**,** 131-314.

ZHAI, Y., MA, Y., DAVID, S. N., ZHAO, D., LOU, R., TAN, G., YANG, R. & YIN, X. 2017. Scalable-manufactured randomized glass-polymer hybrid metamaterial for daytime radiative cooling. *Science,* 355**,** 1062-1066.

ZHOU, L., SONG, H., LIANG, J., SINGER, M., ZHOU, M., STEGENBURGS, E., ZHANG, N., XU, C., NG, T. & YU, Z. 2019. A polydimethylsiloxane-coated metal structure for all-day radiative cooling. *Nature Sustainability,* 2**,** 718-724.

ZHU, L., OTEY, C. R. & FAN, S. 2012. Negative differential thermal conductance through vacuum. *Applied Physics Letters,* 100**,** 044104.

ZHU, L., SANDHU, S., OTEY, C., FAN, S., SINCLAIR, M. B. & SHAN LUK, T. 2013. Temporal coupled mode theory for thermal emission from a single thermal emitter supporting either a single mode or an orthogonal set of modes. *Applied Physics Letters,* 102**,** 103104.

ZHU, Z., EVANS, P. G., HAGLUND JR, R. F. & VALENTINE, J. G. J. N. L. 2017. Dynamically reconfigurable metadevice employing nanostructured phase-change materials. 17**,** 4881-4885.

ZIA, R. & BRONGERSMA, M. L. 2007. Surface plasmon polariton analogue to Young's double-slit experiment. *Nature nanotechnology,* 2**,** 426-429.

Appendix

A1   Script for PSG and PIRA Analysis Calculation

Consideration of A $(\lambda, \theta)= \epsilon(\lambda,\theta)=1-R(\lambda,\theta)-T(\lambda,\theta)$ of the equation 4.62 enables the following code to calculate reflection, transmission, and absorption, as well as emission dependent on angular position. This operation requires the effective refractive index and surface mode, which can be calculated by the FDTD solver. Reflection, transmission, and absorption are calculated by script A1.1. A1.2 computes the electric and magnetic resonance throughout the structure, whereas A1.3 computes the effective design parameters. A1.4, calculate the emission's dependence on angle.

A1.1   Reflection, Transmission and Absorption Script

```
#############################################################################
##### Reflection/transmission/absorption plot
f = getdata('R','f');
T = -transmission('T');
R = transmission('R');
?A = 1-R-T;
plot(c*1e6/f,R,T, A,'wavelength (um)','R/T/A');
legend('R','T','A');
##### plot only the reflection
plot(c/f*1e6,R,"wavelength (microns)","Reflection");
##### plot only the transmission
plot(c/f*1e6,R,"wavelength (microns)"," Transmission ");
##### plot only the absorption
plot(c/f*1e6,A,"wavelength (microns)","Absorption");
```

A1.2   Electric and Magnetic Resonance script

```
#############################################################################
For Electric Resonance
##### |E| at resonance
E = getresult('zx_profile','E');
E2 = pinch(E.E2);
x = E.x;
z = E.z;
lambda = E.lambda;
?fi = find(A,max(A)); # find the frequency point where the absorption becomes maximum
?lambda = lambda(fi);
E2 = pinch(E2,3,fi);
image(x*1e6,z*1e6,E2,"x (um)","z (um)","|E|^2 at "+num2str(round(lambda*1e9))+"
(nm)");
##### field profiles for recorded reflected surface
E2_r = getelectric("R_profile");
```

```
E2_t = getelectric("T_profile");
E2_xz = getelectric("profile_zx_plane");
x = getdata("R_profile","x");
y = getdata("R_profile","y");
z = getdata("profile_zx_plane","z");
image(x*1e6,y*1e6,E2_r,"x (microns)","y (microns)","|E|^2 at reflected surface");
image(x*1e6,y*1e6,E2_t,"x (microns)","y (microns)","|E|^2 at transmitted surface");
image(x*1e6,z*1e6,E2_zx,"x (microns)","z (microns)","|E|^2 at y=0");
# get electric field dataset from the simulation
mname="zx_profile";     # monitor name
E=getresult(mname,"H");    # H fields at monitor
 save dataset to mat file
filename="ElectricField";
matlabsave(filename, H);
```

A1.3   Parameter Analysis Script

```
###############################################################################
nf = getnamed('R','frequency points');
nt1 = 475; # number of points for raius sweep
t1 = linspace(50,1000,nt1)*1e-9;
A = matrix(length(t1),nf);
for (i = 1:length(t1)){
switchtolayout;
setnamed('::model','t1',t1(i));
run;
T = -transmission('T');
R = transmission('R');
A(i,1:nf) = 1-R-T;
?"i = "+num2str(i);
}
f = getdata('T','f');
image(t1(1:nt1)*1e9,c/f*1e6,A,'Px,Py (nm)','wavelength (um)');
###get electric field dataset from the simulation
mname="R";       # monitor name
E=getresult(mname,"E");    # H fields at monitor
save dataset to mat file
filename="Thickness tm";
matlabsave(filename,A,t1);
```

A1.4   Angular Analysis Script

```
###############################################################################
theta = linspace(0,30,4);
A = matrix(length(theta),500);
for (i = 1:length(theta)){
switchtolayout;
```

```
setnamed('source','plane wave type','BFAST'); # enable BFAST
setnamed('source','angle theta',theta(i));
run;
T = -transmission('T');
R = transmission('R');
A(i,1:500) = 1-R-T;
?i;
}
f = getdata('R','f');
image(c*1e6/f,theta,transpose(A),'wavelength (um)','theta','A');
f = getdata('R','f');
image(theta,c*1e6/f,(A),'wavelength (um)','theta','A');
```